High-order series expansions and the determination of crystalline structures for Rydberg atom arrays

Master's Thesis in Physics

Presented by

Antonia Duft

17.05.2023

Institute for Theoretical Physics I
Friedrich-Alexander-Universität Erlangen-Nürnberg

Supervisor: Prof. Dr. Kai Phillip Schmidt

Abstract

A system of hardcore bosons on the links of a Kagome lattice subject to a long-range algebraically decaying van-der-Waals interaction is investigated. It is described by the Fendley-Sengupta-Sachdev (FSS) model, which is known to be the relevant microscopic description of Rydberg atom arrays excited by a detuned laser field. Particular interest lies on this system as an engineerable quantum platform, already realized in experiments, which has been predicted to host a phase with intrinsic topological order. Further, this model contains the transverse-field Ising model (TFIM) for a specific line in parameter space. The limit of weak interaction strengths for both models is analyzed using perturbative continuous unitary transformations and linked cluster expansions, allowing for the extraction of critical properties of possible continuous phase transitions. The long-range interaction is approximated by a truncation after the third-nearest neighbor. Further, multiple limiting cases of the TFIM are investigated, where also the opposite limit of low fields is examined. In particular, in the regime where the system is adiabatically connected to the J_1-J_2 TFIM, a continuous phase transition between the two limits within the 3d XY universality class is found. If the system is adiabatically connected to the J_1-J_3 TFIM, a continuous phase transition within the 3d Ising universality class is found. The determination of crystalline ground-state structures in the classical limit of the FSS model with full long-range van-der-Waals interaction is approached by a systematic search for the energetically most beneficial periodic ordering structure. With this, a phase diagram of the classical limit is determined. The findings are combined into a draft for the quantum phase diagram of the FSS model, which is discussed in particular in the light of the limiting cases of the TFIM with modified interactions.

Zusammenfassung

Ein System von Hardcore-Bosonen auf den Kanten eines Kagome Gitters, welche einer langreichweitigen, algebraisch abfallenden van-der-Waals Wechselwirkung unterliegen, wird untersucht. Dieses wird durch das Fendley-Sengupta-Sachdev (FSS) Modell beschrieben, welches bekanntermaßen die relevante mikroskopische Beschreibung von Rydberg-Atom-Arrays ist, die durch ein verstimmtes Laserfeld angeregt werden. Von besonderem Interesse ist dieses System als eine bereits in Experimenten realisierte Plattform für die Modellierung von Quantensystemen, für die eine Phase mit intrinsischer topologischer Ordnung vorhergesagt wurde. Außerdem enthält dieses Modell das Ising Modell mit transversalem Feld (TFIM) für eine spezifische Linie im Parameterraum. Der Limes niedriger Wechselwirkungsstärken wird für beide Modelle unter der Verwendung der Methode der „perturbative continuous unitary transformations“ und Entwicklungen auf zusammenhängenden Clustern analysiert, wodurch die kritischen Eigenschaften möglicher kontinuierlicher Phasenübergänge extrahiert werden können. Die langreichweitige Wechselwirkung wird durch eine Trunkierung nach dem dritt-nächsten Nachbarn approximiert. Des Weiteren werden verschiedene Grenzfälle des TFIM untersucht, in welchen auch der entgegengesetzte Limes niedriger Felder untersucht wird. Insbesondere wird in dem Regime, in welchem das System adiabatisch mit dem J_1-J_2 TFIM verbunden ist, ein kontinuierlicher Phasenübergang in der 3d XY Universalitätsklasse zwischen den Limites gefunden. Falls das System adiabatisch mit dem J_1-J_3 TFIM verbunden ist, wird ein kontinuierlicher Phasenübergang in der 3d Ising Universalitätsklasse gefunden. An die Bestimmung kristalliner Grundzustandsstrukturen im klassischen Limes des FSS Modells mit voller langreichweitiger Wechselwirkung wird mit einer systematischen Suche nach der energetisch günstigsten periodischen Ordnungsstruktur herangegangen. Hiermit wird ein Phasendiagramm für den klassischen Limes bestimmt. Die Ergebnisse werden in einem Entwurf für das Quantenphasendiagramm des FSS Modells zusammengefasst, welches insbesondere im Bezug auf die Grenzfälle des TFIM mit modifizierten Wechselwirkungen diskutiert wird.

Contents

1. Introduction

The hydrogen atom is encountered early on in the physics education of a student: having only one electron in its orbit and hence the simplest imaginable atomic structure allows carrying out analytical calculations which are not possible for more complicated atoms with, e.g., multiple valence electrons. This simple atomic structure is also a reason for the essential role the hydrogen atom has played historically in the development of the quantum mechanical description of atoms. Many atoms which in principle have a more complicated structure, i.e. multiple electrons and an extended nucleus, show similarities to the hydrogen atom. In particular, this concerns atoms which have a single valence electron, including for example alkali metals like rubidium (Rb) or caesium (Cs). If the valence electron is in a highly excited state, meaning in a state with a high principal quantum number $n \gg 1$, the atom is referred to as Rydberg atom, and respectively, the highly excited state is referred to as Rydberg state [1]. Due to their large electron orbit, the general quantum mechanical description and effective properties of Rydberg atoms are close to the one of hydrogen [1].

An intriguing characteristic of Rydberg atoms is the universal scaling of most of their properties with the quantum number n [2]. The most commonly known of these is probably the scaling of the energy: $E_n \propto 1/n^2$. Other such universal scaling properties are the orbit size (and hence also the electric dipole moment) $\langle r \rangle \propto n^2$, the radiative lifetime $\tau_0 \propto n^3$ and the polarizability $\alpha \propto n^7$ [3]. The large size of Rydberg atoms due to the weakly bound electron orbit can result in large electric dipole moments $\boldsymbol{p} = -e\boldsymbol{d}$ where e is the elementary electric charge and $\boldsymbol{d}$ is the distance vector between atomic core and valence electron [3]. The large dipole moment of Rydberg atoms gives rise to strong dipole-dipole interactions between atoms excited to a Rydberg state. One implication of this strong interaction is the mechanism of the *Rydberg blockade*, which is illustrated in Figure 1.1 [1].

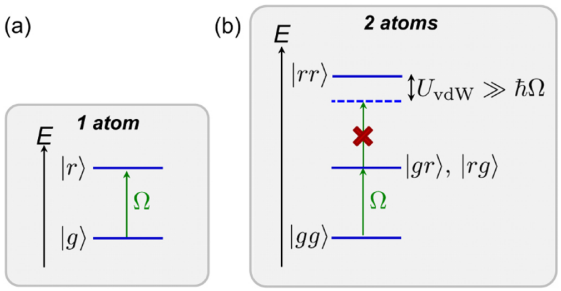

Figure 1.1.: Schematic illustration of the Rydberg-blockade mechanism. (a) The ground state $|g\rangle$ and the Rydberg-excited state $|r\rangle$ of the atom are coupled resonantly by a laser with Rabi-frequency Ω. (b) The doubly Rydberg-excited state $|rr\rangle$ is shifted out of resonance by U_{vdW} due to the van-der-Waals interaction, blockading the excitation to that state. Note that in the main text we set $\hbar = 1$. Figure taken from [1].

The ground state $|g\rangle$ of an atom is coupled resonantly to the Rydberg state $|r\rangle$ by a laser with Rabi-frequency Ω. Now take two atoms next to each other whose composite ground state is

given by $|gg\rangle$. The singly Rydberg-excited states $|gr\rangle$ and $|rg\rangle$ are still resonantly coupled to the ground state. The energy of the doubly Rydberg-excited state $|rr\rangle$ however is shifted out of resonance by U_{vdW} due to the strong interaction. The scaling of the interaction strength for atoms excited to the same Rydberg state $|r\rangle$ can be derived to be of a van-der-Waals type,

$$V \propto R^{-6}\,,$$

where R is the distance between Rydberg atoms [1]. For small enough distances R where $U_{\mathrm{vdW}} \gg \Omega$, this energetic shift is large enough to prevent the simultaneous excitation of atoms to the Rydberg-excited state. Hence, if one atom is excited to a Rydberg state, the excitation of the second atom is said to be 'blockaded' [1]. The corresponding radius within which the interaction is strong enough to result in a blockade is called blockade radius R_b. Rydberg blockade between two atoms was demonstrated experimentally in 2009 by Urban et al. [4] and Gaëtan et al. [5].

The tunable properties of Rydberg atoms result in an important role in multiple research fields from astrophysics [6] over quantum optics [7] to quantum technologies [8]. In particular, Rydberg atoms are a promising building block in quantum computation and quantum simulation.
The idea of using Rydberg atoms for the physical implementation of qubits was proposed by Jaksch et al. in 2000 [9]. In principle, an arbitrary quantum circuit can be built from a set of universal quantum gates consisting of single-qubit rotational gates (X-,Y- and Z-gates, whose action on qubits is given by the corresponding Pauli matrices) and the controlled NOT gate (CNOT gate), a two-qubit gate [10]. Single-qubit operations can be performed by individually subjecting single atoms to laser pulses [9]. The in general more challenging implementation of a two-qubit gate relies on the Rydberg-blockade mechanism, which provides the possibility of a conditional excitation by a driving laser field [11]. In 2010, the first experimental realization of a two-qubit CNOT gate between two Rydberg atoms using the Rydberg-blockade mechanism has been demonstrated in Ref. [12]. They used ^{87}Rb atoms which are excited to Rydberg levels with $n = 90$, which prevents further excitation within a blockade radius $R_b = 10\,\mu\mathrm{m}$ [12]. The extension of the protocol to a two-dimensional qubit array of Cs atoms in optical traps is demonstrated in Ref. [13]. In Ref. [14], two-dimensional qubit arrays with 121 atoms and high two-qubit gate fidelities of $\mathcal{F} = 0.89$ are achieved. Especially considering the scalability of the number of qubits, the weak interactions between ground state atoms make Rydberg atoms an interesting platform for quantum error correction [3].

Besides being a promising candidate for quantum computation, Rydberg atoms already serve as a successful quantum simulation platform for quantum many-body systems. Quantum many-body systems with N spin-1/2 degrees of freedom have Hilbert space dimension 2^N. Especially for strongly correlated and entangled systems, difficulties are encountered in the classical simulation of such systems with approaches like density functional theory (DFT) or tensor network methods [15]. Tensor network methods often fail for strong entanglement, especially in higher dimensions, while DFT becomes inefficient in finding the respective functionals [15]. In general, one relies on approximations when solving such problems. Quantum simulation offers a solution for the efficient simulation of quantum many-body systems where classical approaches fail. The idea is to build a synthetic quantum system which implements the investigated model. One can then study the properties of the synthetic system in order to gain insights into the investigated many-body problem [16]. Further, quantum simulation allows for the tuning of model parameters which could not be tuned for example in real materials, which might allow for further insights [16]. Of course, building a quantum system requires the ability to control individual quantum objects, as well the interactions between them. There are multiple prominent platforms for quantum simulators in which this is possible, including cold neutral atoms in optical lattices [17, 18], trapped ions

[19, 20] and superconducting circuits [21, 22]. Quantum simulators can be used to study a wide range of phenomena, from quantum magnetism [23] to topological phases of matter [24].Rydberg atoms can be controlled individually with optical techniques [16]. Interactions between particles are implemented using Rydberg states, which exhibit long-range interactions that can be controlled and tuned to a high degree (for example by the choice of the Rydberg state n), allowing the engineering of different types of interactions [3]. Further, the precise individual detection of atoms is possible using for example quantum gas microscopes [25, 26], making Rydberg atoms a promising platform for the quantum simulation of a wide range of quantum many-body systems.

In the field of analog quantum simulation, two regimes of interactions between Rydberg atoms imply a natural mapping onto quantum spin models. In particular, atoms in the same Rydberg-excited state interact via a long-range van-der-Waals interaction, $V(r) \propto 1/r^6$ [1]. To build a connection to a spin model, one can map the atoms to a pseudo-spin $1/2$, by identifying ground and Rydberg-excited state with spin down and up state. A system of Rydberg atoms interacting via a van-der-Waals potential and driven by a coherent laser can then be mapped to the Ising model with a transverse and longitudinal magnetic field [3]. This paradigmatic model is studied on atoms in a wide range of lattice geometries.
For example, the antiferromagnetic transverse-field Ising model is studied in one [23, 27, 28] and two dimensions [29–31]. A Rydberg atom simulator with up to 196 atoms on 2D square and triangular lattices is studied in Ref. [32]. Models with additional longitudinal fields are studied for example on the square lattice [33] and the link-Kagome lattice [34].
Further, in the regime of resonant dipole-dipole interaction between Rydberg-excited atoms in different states, where $V(r) \propto 1/r^3$, the spin $1/2$ XY model is realized [16]. This model is studied much less experimentally, with one notable example being the study of the coherent excitation dynamics in a spin chain which are studied in Ref. [35].
Another scheme to the engineering of interactions is offered by Rydberg dressing. A small fraction of the Rydberg-state can be admixed to the ground state by off-resonant coupling, $|\psi\rangle \propto |g\rangle + \epsilon\,|r\rangle$ [3]. This allows to tailor long-range interactions between ground states on spin chains [36] and two-dimensional spin lattices [37].

A particularly interesting model is the already mentioned Ising model with transversal and longitudinal magnetic field on link-Kagome lattice geometries, which is investigated in Ref. [34]. They use a quantum simulator with 219 Rydberg atoms (^{87}Rb) on the links of a Kagome lattice to probe quantum spin liquid states. Quantum spin liquids are highly entangled phases of matter lacking order even at zero temperature [38]. They exhibit for example unique topological properties and non-local excitations. The experimental realization and characterization of such quantum spin liquid states is challenging, as the probing of nonlocal features is required [38]. In the regarded experiment, the atoms are individually trapped in optical tweezer arrays and addressed by a laser which resonantly couples the ground state and Rydberg-excited state by a two-photon optical transition with Rabi-frequency Ω. The different phases of the system are explored using quasi-adiabatic evolution with a slow sweeping of the Rydberg coupling Ω and the detuning δ of the laser over $\sim 2\,\mu$s. Multiple probes, for example the measurement of topological spin operators, allow the detection of a quantum spin liquid phase in an intermediate parameter regime. The existence of such an intermediate spin liquid phase in this particular system is also predicted theoretically in Ref. [39]. The experimental demonstration of a spin liquid phase in the system allows for insights into topological quantum matter. Many open questions remain regarding the investigated system. For example, it is found that long-range couplings destabilize the spin liquid [34]. Further, signatures of a spin liquid phase are found in regimes where it is not expected to be stable as the ground state. Potential for improvement in the quasi adiabatic

state preparation protocol is mentioned in Ref. [34], into whose optimization further insights are provided in Ref. [40]. Altogether, an extension of the theoretical description and experimental studies is required in various aspects.

In this thesis we will focus on the theoretical examination of exactly this system and investigate an arrangement of Rydberg atoms on the links of a Kagome lattice subject to a laser field. Such a system is described by the Fendley-Sengupta-Sachdev (FSS) model [41], which we introduce in chapter 2, where we will again come across the characteristic spatial decay of the van-der-Waals interaction. Further, we will see how the FSS model is related to the paradigmatic transverse-field Ising model (TFIM), as already touched upon. This chapter also includes a brief review of the theoretical predictions concerning the phase diagram of this model. We will then mainly focus on analyzing the quantum phase diagram from the limit of weak interaction strengths, which we achieve by performing series expansions using the method of perturbative continuous unitary transformations which is introduced in chapter 3. As will be shown, the thereby derived effective Hamiltonian can be evaluated in the thermodynamic limit on linked clusters. A method for analyzing a classical limit that can be found within the FSS model is described in chapter 4. We will then turn to discussing our results, starting with the special case of the TFIM in chapter 5. We then discuss our findings for the full FSS model, including its classical limit, in chapter 6. We close with a conclusion and an outlook over possible further research in chapter 7.

2. Rydberg atom arrays on the link-Kagome lattice

In this chapter we introduce the model of Rydberg atoms arranged on the link-Kagome lattice which we investigate in this thesis. In section 2.1 we define the so called Fendley-Sengupta-Sachdev model [41] which describes arrangements of Rydberg atoms subject to a laser field. In section 2.2 we identify a specific parameter ratio within this model which corresponds exactly to the paradigmatic transverse-field Ising model. The investigation of this model has been subject to recent theoretical and experimental research. Particular interest arises at it is a promising model to realize $\mathbb{Z}_2$ quantum spin liquid states, as predicted in Ref. [39]. Experimental signatures of such states could also be found in Ref. [34]. Section 2.3 gives a short overview over the phase diagram constructed from recent theoretical findings.

2.1. The Fendley-Sengupta-Sachdev model

A system of Rydberg atoms arranged on a lattice and driven by a laser field is described by the Fendley-Sengupta-Sachdev (FSS) model [41]. In this model, the description of a Rydberg atom is reduced to an effective two-level system with ground state $|g\rangle$ and Rydberg-excited state $|e\rangle$. Those two levels are coupled resonantly by the laser with Rabi-frequency Ω and detuning δ. Rydberg-excited atoms can be described as electric dipoles. Hence, the energy shift due to the interaction between two simultaneously Rydberg-excited atoms with cores at positions $\boldsymbol{r}_i$ and $\boldsymbol{r}_j$ can be obtained by considering the dipole-dipole interaction (in natural units) [1],

$$V_{dd} = \frac{\boldsymbol{d}_i \cdot \boldsymbol{d}_j - 3\,(\boldsymbol{d}_i \cdot \boldsymbol{e}_R)\,(\boldsymbol{d}_j \cdot \boldsymbol{e}_R)}{|\boldsymbol{r}_i - \boldsymbol{r}_j|^3}\,.$$

Here, $\boldsymbol{d}_i$ is the displacement vector of the valence electron with respect to the atomic core and $\boldsymbol{e}_R$ is the unit vector in $\boldsymbol{R} = \boldsymbol{r}_i - \boldsymbol{r}_j$ direction. Second-order perturbation theory in the interaction strength yields an energy shift due to the van-der-Waals interaction[1] scaling as $|\boldsymbol{r}_i - \boldsymbol{r}_j|^{-6}$.

Combining the driving of the system with a laser field and the van-der-Waals interaction gives us the total FSS Hamiltonian

$$H^{\mathrm{FSS}} = \frac{\Omega}{2}\sum_i \left(b_i + b_i^\dagger\right) - \delta\sum_i n_i + \sum_{i<j} V_{ij}\, n_i n_j\,, \tag{2.1}$$

with hardcore bosonic annihilation operator $b_i = |g\rangle\langle e|$, creation operator $b_i^\dagger = |e\rangle\langle g|$ and particle number operator $n_i = b_i^\dagger b_i$. For the sake of compact notation we write the long-range

[1] As argued in Ref. [1], one can identify different regimes describing the interaction between atoms excited to the same Rydberg state $|e\rangle$. The interaction is of a van-der-Waals type if the excited pair state $|ee\rangle$ is off resonance with another doubly excited state. If the state $|ee\rangle$ is (quasi-)degenerate with another doubly excited state the interaction scales as $V(r) \propto 1/r^3$ and is referred to as Förster resonance. Further, resonant dipole-dipole interactions can occur between resonantly coupled states $|\alpha\beta\rangle$ and $|\beta\alpha\rangle$ with $n \approx n'$.

van-der-Waals interaction between Rydberg excited atoms at sites i and j as $V_{ij} := V/|\boldsymbol{r}_i - \boldsymbol{r}_j|^6$ and call the coefficient $V > 0$ the interaction strength[2]. The summation indices i and j label the sites of the lattice and run over all sites i or all pairs (i, j) respectively, where the condition $i < j$ implies that each pair of sites is only taken into account once.

As already hinted at by the particle number representation of the Hamiltonian, we take a slight detour from the picture of an atom which is in its ground state $|g\rangle$ or in its Rydberg-excited state $|e\rangle$. In particular, we equivalently refer to the ground state of the atom at site i as an occupation of zero particles $|0\rangle$ at site i and to the Rydberg-excited state as occupation of one particle $|1\rangle$. The creation and annihilation operators $b_i^\dagger$ and b_i for these particles fulfill hardcore bosonic statistics: particles at different lattice sites i and j behave like bosons, i.e.

$$[b_i, b_j^\dagger] = \delta_{ij}, \quad [b_i^\dagger, b_j^\dagger] = [b_i, b_j] = 0 \quad \text{for} \quad i \neq j\,,$$

while particles at the same lattice site i have the additional hardcore constraint

$$b_i^\dagger b_i^\dagger = b_i b_i = 0\,,$$

which prohibits the occupation of a site by more than one (hardcore) boson.

It is often useful to describe such systems in another - magnetic - language in terms of spin-1/2 degrees of freedom. We use the Matsubara-Matsuda transformation [42] which maps between hardcore bosons and pseudo-spin 1/2. The transformation identifies an unoccupied site with a spin up and an occupied site with a spin down:

$$|0\rangle_i \mathrel{\widehat{=}} |\uparrow\rangle_i\,,$$
$$|1\rangle_i \mathrel{\widehat{=}} |\downarrow\rangle_i\,.$$

Here a pictorial representation of the two possible spin orientations 'up' and 'down' (referring to the σ^z quantization axis) is used. So, creating a particle by $b_i^\dagger$ corresponds to flipping the spin at site i from up to down, and vice versa for the annihilation by b_i. Counting the occupation of site i corresponds to evaluating the σ_i^z eigenvalue. This allows us to relate the hardcore bosonic operators to the Pauli matrices acting on a spin state represented by $(|\uparrow\rangle, |\downarrow\rangle)$:

$$\sigma_i^x = b_i + b_i^\dagger\,,$$
$$\sigma_i^z = 1 - 2n_i\,.$$

In this pseudo-spin language, the Hamiltonian in Equation (2.1) becomes

$$H^{\text{spin}} = \frac{\Omega}{2}\sum_i \sigma_i^x - \frac{\delta}{2}\sum_i (1 - \sigma_i^z) + \frac{1}{8}\sum_{i\neq j} V_{ij}(1 - 2\sigma_i^z + \sigma_i^z\sigma_j^z)\,. \tag{2.2}$$

We will omit the explicit notion of *pseudo*-spin in the following. The additional factor 1/2 compared to Equation (2.1) takes into account the double counting of each pair of sites by the summation running over $i \neq j$ here instead of $i < j$.

[2] In the literature, the coefficient V is also often referred to as C_6 (hinting at the scaling of the van-der-Waals interaction with the distance r as $1/r^6$) and scales with the principal quantum number n of the Rydberg-excited state as n^{11} [1].

2.1.1. The link-Kagome lattice structure

Having introduced the general Hamiltonian describing Rydberg atom arrays we now investigate a specific arrangement, namely the one of placing the Rydberg atoms on the links of a Kagome lattice, which is illustrated in Figure 2.1.

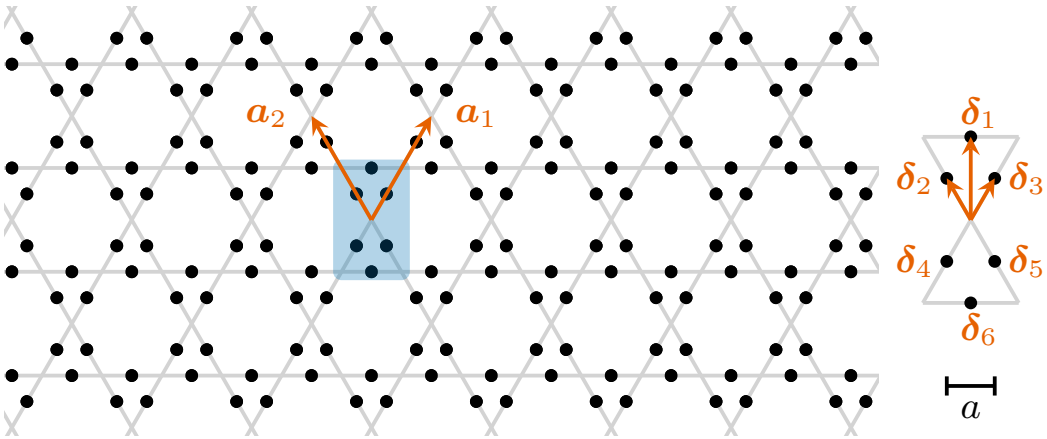

Figure 2.1.: Visualization of the link-Kagome lattice geometry. The underlying Kagome lattice structure is shown in light gray. The Rydberg atoms are placed on the links of this lattice, shown as black circles. The unit cell of the link-Kagome lattice consisting of six sites is highlighted by the blue shaded region. The positions of the unit cells are given by the translational lattice vectors $\boldsymbol{a}_1$, $\boldsymbol{a}_2$. The sites within the unit cell are positioned at $\boldsymbol{\delta}_\alpha$ relative to its center and labeled with an index $\alpha = 1, \ldots, 6$ according to the convention defined in the figure (right inset).

This lattice consists of hourglass-shaped unit cells with six sites which are arranged on an underlying triangular lattice. The unit cells are centered at positions

$$\{\boldsymbol{R}_{nm}\}_{n,m\in\mathbb{Z}} \quad \text{with} \quad \boldsymbol{R}_{nm} = n\boldsymbol{a}_1 + m\boldsymbol{a}_2\,,$$

spanning the translational lattice. The translational vectors of the lattice are given by

$$\boldsymbol{a}_1 = a\begin{pmatrix} 1 \\ \sqrt{3} \end{pmatrix}\,, \tag{2.3a}$$

$$\boldsymbol{a}_2 = a\begin{pmatrix} 1 \\ -\sqrt{3} \end{pmatrix}\,, \tag{2.3b}$$

where a is the lattice constant defining the minimal distance between sites as illustrated in Figure 2.1. We will set $a = 1$. The sites within the unit cell relative to its center are given by $\boldsymbol{\delta}_{1,\ldots,6}$ with

$$\boldsymbol{\delta}_1 = \frac{a}{4}\begin{pmatrix} 0 \\ 2\sqrt{3} \end{pmatrix} = -\boldsymbol{\delta}_6\,, \tag{2.4a}$$

$$\boldsymbol{\delta}_2 = \frac{a}{4}\begin{pmatrix} 1 \\ -\sqrt{3} \end{pmatrix} = -\boldsymbol{\delta}_5\,, \tag{2.4b}$$

$$\boldsymbol{\delta}_3 = \frac{a}{4}\begin{pmatrix} 1 \\ \sqrt{3} \end{pmatrix} = -\boldsymbol{\delta}_4\,. \tag{2.4c}$$

The full lattice is then given by adding the position vectors of the sites within a unit cell to the translational lattice:

$$\{\boldsymbol{r}_{nm\alpha}\}_{n,m\in\mathbb{Z},\alpha=1,..6} \quad \text{with} \quad \boldsymbol{r}_{nm\alpha} = n\boldsymbol{a}_1 + m\boldsymbol{a}_2 + \boldsymbol{\delta}_\alpha \,.$$

Due to the long-range van-der-Waals interaction between Rydberg-excited atoms, each excited atom interacts with each other excited atom and each site is coupled to every other site in the lattice. However, the interaction strength decays rapidly with the distance r between two atoms, namely with r^{-6}. To illustrate this rapid decay, we calculate the interaction strengths for the four smallest distances between sites on the link-Kagome lattice (setting the minimal distance between sites on the lattice $a = 1$):

$$V_1 = V\,, \quad V_2 = \frac{1}{27}\,V\,, \quad V_3 = \frac{1}{64}\,V\,, \quad V_4 = \frac{1}{343}\,V\,.$$

For a numerical approach to the weak-interaction-strength limit of this model, we choose to truncate the long-range interaction at some point, in particular after the third-nearest neighbor. We thus take three different interaction strengths into account, which will be referred to as $V_{1,2,3}$ respectively. The geometry of those considered couplings on the lattice is illustrated in Figure 2.2.

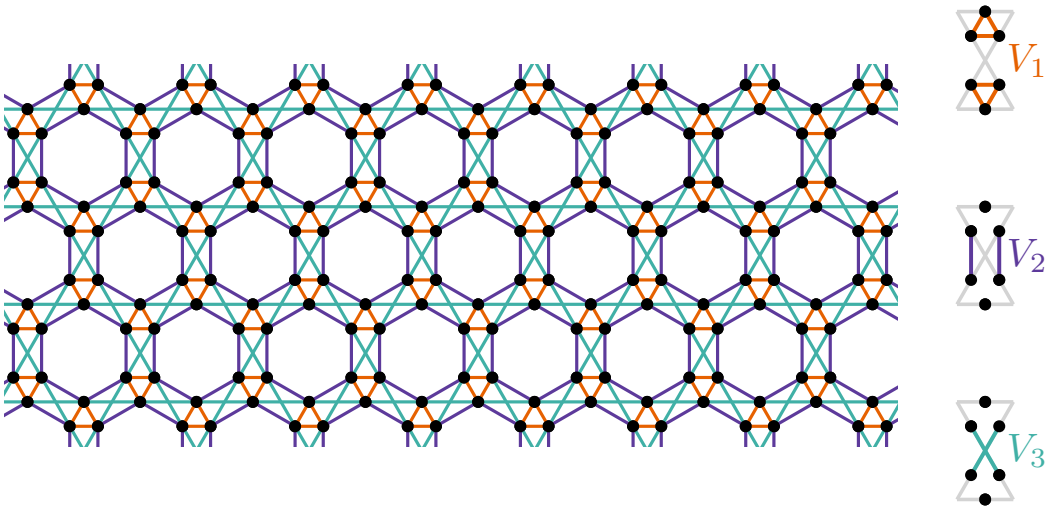

Figure 2.2.: Visualization of the sites coupled on the link-Kagome lattice by the truncated interaction. The Rydberg atoms placed on the black circles are either in their ground state $|g\rangle$ or in a Rydberg-excited state $|e\rangle$. Rydberg-excited atoms are coupled via a long-range van-der-Waals interaction. We truncate this interaction after the third-nearest neighbor. The geometry of the three nearest-neighbor interactions V_i with $i \in \{1, 2, 3\}$ is illustrated on the right-hand side. Considering these leads to the coupling geometry shown on the left, with the different coupling strengths of V_i indicated by corresponding colors.

2.1.2. Weak-interaction-strength limit of the Fendley-Sengupta-Sachdev model

We will now define the limit of weak interaction strengths V in the FSS model. For $V = 0$, the Hamiltonian is purely local:

$$H_0^{\text{spin}} = \frac{\Omega}{2} \sum_i \sigma_i^x - \frac{\delta}{2} \sum_i (1 - \sigma_i^z) \ . \tag{2.5}$$

For small V, we interpret the interaction as a perturbation:

$$H_1^{\text{spin}} = \frac{1}{8} \sum_{i \neq j} V_{ij} (1 - 2\sigma_i^z + \sigma_i^z \sigma_j^z) \, . \tag{2.6}$$

The unperturbed, local Hamiltonian H_0^{spin} can be solved exactly by applying a unitary transformation U which rotates the quantization axis of the spins clockwise by ϕ with $\tan(\phi) = \Omega/\delta$. In its thereby obtained eigenbasis the unperturbed Hamiltonian reads

$$\tilde{H}_0^{\text{spin}} = U^\dagger H_0^{\text{spin}} U = \sum_i \left(-\frac{\delta}{2} + \frac{1}{2} \sqrt{\delta^2 + \Omega^2} \, \tilde{\sigma}_i^z \right) = \sum_i \left(\tilde{\epsilon}_0 + \tilde{\Delta} \, \tilde{\sigma}_i^z \right) \ , \tag{2.7}$$

where objects denoted with a '$\sim$' are defined with respect to the rotated quantization axis. Each site contributes the energy $\tilde{\epsilon}_0 \pm \tilde{\Delta}$, depending on the orientation of the respective spin. The ground state of the system is the eigenstate which minimizes the total energy. In the unperturbed system this corresponds to all spins having the eigenvalue $\tilde{\sigma}^z = -1$, thus pointing down:

$$|\text{GS}\rangle = \bigotimes_i |\tilde{\downarrow}\rangle_i \ .$$

This ground state has the energy

$$E_0 = N \cdot (\tilde{\epsilon}_0 - \tilde{\Delta}) \, ,$$

where N denotes the total number of sites in the system. We can see that $\tilde{H}_0^{\text{spin}}$ acts on the non-interacting spins like a uniform magnetic field would by aligning each of them against the quantization axis $\tilde{\sigma}^z$ whose direction is given by the ratio of the Rabi-frequency Ω and the detuning δ of the laser field which is applied to the system.

When applying the unitary transformation to H, we also have to rotate the interaction H_1^{spin} accordingly which results in the following expression:

$$\begin{aligned} \tilde{H}_1^{\text{spin}} = \frac{1}{8} \sum_{i \neq j} V_{ij} \big(1 - 2\cos\phi \, \tilde{\sigma}_i^z + 2\sin\phi \, \tilde{\sigma}_i^x + \cos^2\phi \, \tilde{\sigma}_i^z \tilde{\sigma}_j^z + \\ + \sin^2\phi \, \tilde{\sigma}_i^x \tilde{\sigma}_j^x - 2\cos\phi \sin\phi \, \tilde{\sigma}_i^z \tilde{\sigma}_j^x \big) \ . \end{aligned} \tag{2.8}$$

Of course, we can equivalently express the Hamiltonian in the eigenbasis of H_0 using hardcore bosonic operators. Here, the unperturbed part is given by

$$\tilde{H}_0^{\text{FSS}} = \sum_i \left[\left(\tilde{\epsilon}_0 - \tilde{\Delta} \right) + 2\tilde{\Delta} \, \tilde{n}_i \right] \ . \tag{2.9}$$

The perturbation in the hardcore bosonic eigenbasis equates to

$$\tilde{H}_1^{\mathrm{FSS}} = \frac{1}{8}\sum_{i\neq j} V_{ij}\Big[(1+\cos\phi)^2 - 4\cos\phi\,(1+\cos\phi)\,\tilde{n}_i + 2\sin\phi\left(\tilde{b}_i^\dagger + \mathrm{h.c.}\right) + \\ + 4\cos^2\phi\,\tilde{n}_i\tilde{n}_j + \sin^2\phi\left(\tilde{b}_i^\dagger\tilde{b}_j + \tilde{b}_i^\dagger\tilde{b}_j^\dagger + \mathrm{h.c.}\right) - 2\cos\phi\sin\phi\left(2\tilde{b}_i^\dagger\tilde{n}_j - \tilde{b}_i^\dagger + \mathrm{h.c.}\right)\Big]\,. \tag{2.10}$$

The transformed operators $\tilde{b}_i$, $\tilde{b}_i^\dagger$ and $\tilde{n}_i$ still fulfill the same hardcore bosonic statistics as the unrotated ones. However, for general δ and Ω they do not correspond to the annihilation, creation or counting of a tangible physical particle any more. Still, as will become clear in the next paragraph, it is meaningful to say that $\tilde{b}_i^\dagger$ creates a *quasi*-particle (correspondingly for $\tilde{b}_i$ and $\tilde{n}_i$).

Thinking in this quasi-particle number basis gives an intuitive way of understanding the unperturbed energy spectrum. We can simply read off the ground-state energy of the unperturbed system E_0 by setting the number of quasi-particles on each site $\tilde{n}_i$ to zero:

$$|\mathrm{GS}\rangle = \bigotimes_i |\tilde{0}\rangle_i\,.$$

Each added quasi-particle then increases the energy of the state by $2\tilde{\Delta}$. This resembles the well-known ladder spectrum of a harmonic oscillator with constant energy shift $\left(\tilde{\epsilon}_0 - \tilde{\Delta}\right)$ and ladder spacing $2\tilde{\Delta}$. Accordingly, we also call a quasi-particle an 'elementary excitation' of the (unperturbed) ground state. In the spin picture, the addition of a quasi-particle at site i corresponds to flipping the spin at site i from $|\tilde{\downarrow}\rangle_i$ to $|\tilde{\uparrow}\rangle_i$, and the removal of a quasi-particle to the inverse spin flipping. We can thus think equivalently of quasi-particles added to the vacuum ground state with zero quasi-particles and spin flips within the ground state of spins aligned against the $\tilde{\sigma}^z$ quantization axis. The equivalence of the two pictures is illustrated in Figure 2.3.

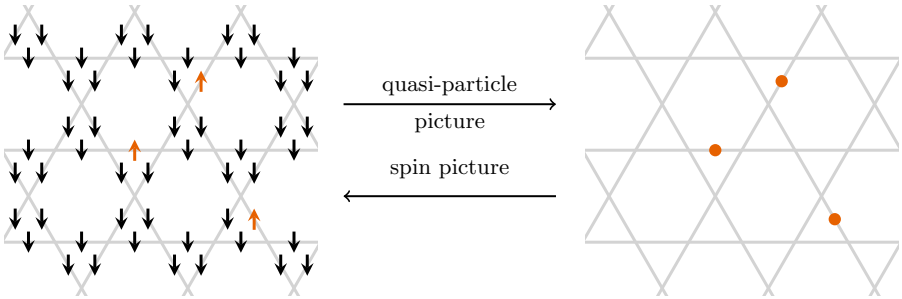

Figure 2.3.: Illustration of the mapping between spin picture (left) and quasi-particle picture (right). In the spin picture, each spin 1/2 can point either up or down. The figure shows one possible configuration of spins on a cutout of the lattice. The ground state of the unperturbed model is given by all spins pointing down (black). Flipping the spin at a site up (orange) increases the energy of the state and can be interpreted as an elementary excitation or quasi-particle. In a quasi-particle picture this corresponds to an empty lattice (vacuum) where quasi-particles are placed at the sites with spin pointing up (orange dots). Note that in the model, those quasi-particles and spins are defined in the transformed basis. However, to lighten the illustration, the '∼' indicating the definition in the rotated basis is omitted.

For normalization reasons, we rescale the Hamiltonian by $2\tilde{\Delta}$, such that the unperturbed energy of one quasi-particle is equal to one (compare Equation (2.9)). For better readability, we will keep using the expression $\tilde{H}^{\mathrm{FSS}}$ when we are actually referring to $\tilde{H}^{\mathrm{FSS}}/2\tilde{\Delta}$ in an abuse of notation. Accordingly, the perturbation parameter is defined as $\lambda = V/2\tilde{\Delta}$.

2.2. The transverse-field Ising model

One of the paradigmatic models in the field of quantum many-body systems is the transverse-field Ising model (TFIM). In this section we define the TFIM and establish its connection to the FSS model. The Ising model has first been described verbally by Ernst Ising in 1924 [43] in order to describe the spontaneous magnetization process of many-body systems. It takes a system of spin 1/2 degrees of freedom placed on a lattice which interact via an antiferromagnetic (ferromagnetic) Ising coupling with strength $J > 0$ ($J < 0$). The addition of a uniform transverse magnetic field with strength h then results in the TFIM,

$$H^{\mathrm{TFIM}} = h \sum_i \sigma_i^x + \sum_{i<j} J_{ij} \sigma_i^z \sigma_j^z \,. \tag{2.11}$$

As in the previous section, we denote the interaction between spins at sites i and j by J_{ij}. If the Ising interaction strength is long-range and decays for example algebraically as $J_{ij} = J/|\boldsymbol{r}_i - \boldsymbol{r}_j|^\alpha$ with $\alpha > 0$, the model is more specifically called long-range transverse-field Ising model. The combination of long-range interactions and antiferromagnetic Ising coupling on a geometrically frustrated lattice - like for example the link-Kagome lattice - requires a detailed analysis, as known for example from the triangular lattice [44–48].

We will now establish the relation between the FSS model and the TFIM. Let us again start with the FSS Hamiltonian expressed in terms of spin 1/2 degrees of freedom in Equation (2.2). For the sake of universality, the long-range interaction is here defined by a variable decay exponent α, where the van-der-Waals interaction is recovered by setting $\alpha = 6$. We want to rearrange the summands in such a way that the Hamiltonian resembles the one of the TFIM for which we start by rewriting the expression for the interaction. Specifically, instead of summing over all pairs of spins on the lattice, $i < j$, we sum over all sites i on the lattice and all vectors $\boldsymbol{d} \neq \boldsymbol{0}$ from i to any other site $j \neq i$ on the lattice. We can then write the Hamiltonian as follows:

$$\begin{aligned} H^{\mathrm{spin}} &= \frac{\Omega}{2} \sum_i \sigma_i^x - \frac{\delta}{2} \sum_i (1 - \sigma_i^z) + \frac{1}{8} \sum_{i \neq j} V_{ij} \sigma_i^z \sigma_j^z + \frac{1}{8} \sum_i \underbrace{\left(\sum_{\boldsymbol{d} \neq \boldsymbol{0}} \frac{V}{|\boldsymbol{d}|^\alpha} \right)}_{=: V \bar{\mu}^\alpha} (1 - 2\sigma_i^z) \\ &= \frac{\Omega}{2} \sum_i \sigma_i^x + \left(\frac{\delta}{2} - \frac{V \bar{\mu}^\alpha}{4} \right) \sum_i \sigma_i^z + \frac{1}{8} \sum_{i \neq j} V_{ij} \sigma_i^z \sigma_j^z + \text{const.}\,. \end{aligned}$$

In this arrangement the Hamiltonian looks very similar to H^{TFIM} in Equation (2.11). In fact, we see that the FSS Hamiltonian describing a Rydberg atom system is equal to the TFIM Hamiltonian with an additional longitudinal field σ^z where the amplitude depends on δ and V. Hence, we can recover the TFIM by choosing those two parameters such that the amplitude of the longitudinal field becomes zero:

$$\left(\frac{\delta}{2} - \frac{V \bar{\mu}^\alpha}{4} \right) = 0 \quad \Leftrightarrow \quad \frac{\delta}{V} = \frac{\bar{\mu}^\alpha}{2} \,.$$

Note that this result is valid for general long-range interactions with algebraic decay with decay exponent α. In the following, we will go back to fixing $\alpha = 6$ as given by the van-der-Waals interaction between Rydberg-excited atoms. For the specific geometry of the link-Kagome lattice with a truncation of the interaction after the third-nearest neighbor as discussed before, we obtain $\bar{\mu}^6 = \sum_{\boldsymbol{d}} 1/|\boldsymbol{d}|^6 \approx 2.105$. Furthermore, equality of H^{spin} and H^{TFIM} requires setting $h = \Omega/2$ and $J = V/4 > 0$.

We will investigate the antiferromagnetic TFIM as a specific parameter ratio in the FSS model. So, naturally, we want to analyze the same limiting case of weak interaction strengths $J \ll h$. Note that this limit is commonly referred to as high-field limit. Analogously, we identify the unperturbed Hamiltonian in Equation (2.11) as

$$H_0^{\text{TFIM}} = h \sum_i \sigma_i^x \,, \tag{2.12}$$

and the Ising coupling as perturbation

$$H_1^{\text{TFIM}} = \sum_{i<j} J_{ij} \sigma_i^z \sigma_j^z \,. \tag{2.13}$$

The unperturbed ground state is given by aligning all spins against the magnetic field h:

$$|\text{GS}\rangle = \bigotimes_i |{\leftarrow}\rangle_i \,.$$

Pictorially we denote the alignment along (against) the σ_i^x axis by an arrow pointing to the right (left). The energy of this ground state is given by

$$E_0 = -hN \,,$$

where again N denotes the number of sites on the lattice. The perturbation H_1 flips the spin of two sites i and j coupled by J_{ij}.

It is again illustrative to switch between this spin picture and a quasi-particle picture with a Matsubara-Matsuda transformation [42] as introduced in section 2.1. Identifying the ground state with the quasi-particle vacuum, we obtain the following correspondences between spin and quasi-particle language:

$$\begin{aligned} |{\leftarrow}\rangle_i &\mathrel{\widehat{=}} |0\rangle_i \,, \\ |{\rightarrow}\rangle_i &\mathrel{\widehat{=}} |1\rangle_i \,, \\ \sigma_i^x &= 2n_i - 1 \,, \\ \sigma_i^z &= b_i^\dagger + b_i \,. \end{aligned}$$

Again, the operators $b_i, b_i^\dagger$ fulfill hardcore bosonic statistics. We can now express the TFIM Hamiltonian in this quasi-particle basis:

$$H^{\text{TFIM}} = 2h \sum_i n_i - hN + \sum_{i<j} J_{ij} \left(b_i b_j + b_i^\dagger b_j + \text{h.c.} \right) \,. \tag{2.14}$$

Here, we see that the perturbation corresponds to the creation (annihilation) of two quasi-particles at sites i and j or the hopping of one quasi-particle from site i to j (or vice versa). Similarly to the FSS model, we rescale the Hamiltonian by $2h$ such that the energy of one quasi-particle is normalized to one, but keep referring to the rescaled Hamiltonian as H^{TFIM}. The perturbation parameter is then defined as $\lambda = J/2h$.

2.3. Recent theoretical investigations of the phase diagram

In this section, we give a short overview about some recent theoretical research done on the model investigated in this thesis. While Rydberg atom arrangements are already a heavily studied subject, especially in the field of quantum simulators (see e.g. [32, 33]), the particular lattice geometry of the link-Kagome lattice has gained interest as it is predicted to physically realize a spin liquid state [39]. A quantum spin liquid is defined as a phase exhibiting a high degree of entanglement with lack of order even at zero temperature [38]. This includes phases with topological order, for which the Kitaev toric code is the canonical example [49]. The relevance of the prediction of a spin liquid state in this model is underlined by the experimental demonstration of respective signatures in a quantum simulator with 219 Rydberg atoms (^{87}Rb) by Semeghini et al. in Ref. [34].

In Ref. [39], Verresen et al. investigate the FSS model on the link-Kagome lattice. They focus on a blockade model, where the algebraically decaying repulsive interaction $V(r) = V/r^6$ is approximated by

$$V(r) = \begin{cases} +\infty & \text{if } r \leq 2a\,, \\ 0 & \text{if } r > 2a\,. \end{cases}$$

Note that the radius $2a$ includes distances up to the third-nearest neighbor, such that each site is coupled to six other sites. This approximation is related to the Rydberg-blockade mechanism: strong van-der-Waals interactions shift the Rydberg-excited states of atoms close to a Rydberg-excited atom out of resonance with the Rabi-frequency Ω, such that simultaneous excitation is suppressed within a blockade radius $R_b = 2a$ [1].
Their approach to predicting a $\mathbb{Z}_2$ spin liquid is rooted in the connection of this blockade model to dimer models on the Kagome lattice [50, 51]. In a dimer picture, an occupied site on a link of the Kagome lattice corresponds to a dimer connecting the two adjacent vertices of the lattice. Maximal filling in the blockade model corresponds to a perfect dimer covering, where each vertex on the lattice is touched by exactly one dimer, and the density of dimers is $\langle n \rangle = 1/4$. This is realized for $\delta \to \infty$. They relate this case to a pure odd $\mathbb{Z}_2$ gauge theory, where the deconfined phase has toric code like topological order [52].
The Rydberg-blockade FSS model also allows fillings $\langle n \rangle < 1/4$, in which case some vertices are touched by no dimer (referred to as monomer). Looking at the FSS Hamiltonian in Equation (2.1), the density of monomers is affected only by the Rabi-oscillations (with Ω), which create or destroy pairs of monomers. For large δ/Ω, the system is then perturbatively described by monomer fluctuations about maximally filled dimer states. This allows for resonances between dimer states. Further, extending the dimer model to include monomers results in the existence of a trivial, translation-symmetric phase, in which the monomers condense. It is argued, that the regime of a small admixture of monomers to the perfect dimer covering is promising to stabilize a spin liquid phase, due to the induced resonances between different dimer states [39].
Using the density matrix renormalization group (DMRG) [53, 54], Verresen et al. obtain the phase diagram shown in Figure 2.4 [39]. Here, they argue the following limiting cases. For small δ/Ω, the system is connected adiabatically to the trivial empty state. For large δ/Ω the system is approximated by a dimer model with low monomer density. This approximation is confirmed by a calculation of the filling fraction $\langle n \rangle \approx 1/4$ for $\delta/\Omega \to \infty$. The ground state is found to be a valence bond solid (VBS) which breaks crystalline symmetries. In between those two phases, for intermediate δ/Ω, they find an intermediate phase which is argued to be a $\mathbb{Z}_2$ spin liquid. They locate the phase transitions by a divergence of the correlation length ξ and the entanglement entropy S (see Figure 2.4). They find that the filling fraction within this intermediate phase

is smaller, but close to the $\langle n \rangle \approx 1/4$ in the VBS phase. This indicates that the intermediate phase is still approximated by a dimer model, as expected for the predicted $\mathbb{Z}_2$ spin liquid. They find a sharp drop in the filling fraction upon entering the trivial phase, which they connect to a condensation of monomers.

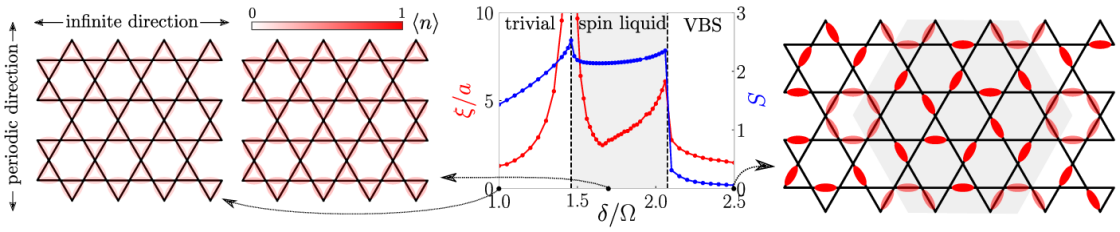

Figure 2.4.: Phase diagram of the blockade model on the link-Kagome lattice as determined in Ref. [39]. Alongside a depiction of the phase diagram, an exemplary density plot for each of the three observed phases is shown. The phases are separated by the diverging correlation length ξ and the entanglement entropy S. For small δ/Ω the system is connected adiabatically to the empty, trivial phase. For large δ/Ω, the system is in a valence bond solid (VBS) phase, breaking the crystalline symmetry as illustrated. An intermediate, featureless spin liquid phase is found for intermediate δ/Ω and characterized for example by a large entanglement plateau. The figure is taken from Ref. [39].

Verresen et al. give multiple evidences that the intermediate phase is actually a $\mathbb{Z}_2$ spin liquid in Ref. [39]. One of those is the calculation of the topological entanglement entropy γ. For gapped phases, γ is related to the entanglement entropy via $S(L) = \alpha L - \gamma$, where L is the length of the boundary between two regions A and B. For $\mathbb{Z}_2$ spin liquids one has $\gamma = \ln 2$, which is roughly the obtained value.
Another evidence is found in the evaluation of the two string operators of a $\mathbb{Z}_2$ gauge theory. The diagonal string P measures the parity of dimers encountered along the string. It anticommutes with the off-diagonal string Q upon intersection. Open Q strings create a monomer at each end, which is also referred to as an electric excitation e in the context of a $\mathbb{Z}_2$ gauge theory. Open P strings create a magnetic excitation m at each end. The anticommutation of P and Q gives rise to nontrivial mutual statistics of e and m. Condensates of e or m give rise to long-range order in Q and P, respectively. Thus, the string operators are used to diagnose the trivial and the VBS phase. In the trivial phase they obtain $\langle Q \rangle \neq 0$, which shows that it corresponds to a condensate of monomers (e). In the confined VBS phase they obtain $\langle P \rangle \neq 0$, indicating an m condensate. In the intermediate phase, they find that both $\langle P \rangle$ and $\langle Q \rangle$ decay to zero, which is consistent with it being the deconfined phase of the gauge theory and neither an e nor an m condensate.
Further, they investigate the topological ground-state degeneracy on infinitely long cylinders. One expects four distinct topological ground states (corresponding to 1, e, m and $f = e \times m$) which can be detected with P and Q loops around the circumference. With this, they confirm the expectation.

In Ref. [39], Verresen at al. also extend their investigation to the Rydberg potential $V(r) \propto 1/r^6$. Here, they discuss not only the link-Kagome lattice but a family of ruby lattices which contains the aspect ratio ρ of the rectangles (compare Figure 2.2) as free tuning parameter. Within this family, the link-Kagome lattice is realized for the particular case $\rho = \sqrt{3}$. In that case, they find a spin liquid around $\delta/\Omega = 3.5$ for $\Omega = V/2.4^6$ with a truncation of the interaction after the

fourth-nearest neighbor. However, they also find indications that the inclusion of further apart neighbors (i.e., the inclusion of the full long-range interaction) seems to destabilize the spin liquid phase. Specifics of this also depend on the chosen ρ. Understanding the origin and stabilization of a quantum spin liquid state on the link-Kagome lattice remains an open question and active field of research [52, 55, 56]. Note however that the predictions of a spin liquid state rely on the mechanism of Rydberg blockade, which again relies on strong interactions between proximate Rydberg atoms. Within the perturbative expansion around the weak-interaction-strength limit we will investigate, this regime is not reached and we do not come close to the parameter region where topological order is predicted. In particular, the above $\Omega = V/2.4^6$ and $\delta/\Omega = 3.5$ translate to a perturbation parameter $\lambda = V/2\tilde{\Delta} \approx 52 \gg 1$.

3. Perturbative series expansions in the limit of weak interaction strengths

In this chapter we introduce the methods used to investigate the limit of weak interaction strengths, $V \ll \tilde{\Delta}$, of the FSS model on the link-Kagome lattice which was defined in the previous chapter. For the TFIM contained in the FSS model, as discussed in section 2.2, this limit corresponds to $J \ll h$, more commonly referred to as the high-field limit. In both models, the limit of zero interaction strength corresponds to spins aligning in an effective magnetic field. We define this magnetic field as the unperturbed part. Accordingly, we treat the interaction as perturbation with perturbation parameter $\lambda = V/2\tilde{\Delta}$ ($\lambda = J/2h$). Physical quantities like for example the ground-state energy will then be calculated as a perturbative series in λ by applying the method of perturbative continuous unitary transformations (pCUT) which is introduced in section 3.1. The pCUT method aims at transforming the Hamiltonian into an effective model H_{eff} which is quasi-particle conserving and thus allows the investigation of individual quasi-particle channels.

Note that the pCUT method has several advantages. Firstly, it is model-independent and can be applied to a wide range of problems which fulfill commonly given prerequisites discussed in section 3.1. Secondly, physical quantities can be calculated in the thermodynamic limit due to the cluster additivity of the effective Hamiltonian as described in section 3.2. We will exploit the cluster additivity in the efficient computation of quantities in the thermodynamic limit on finite linked clusters and discuss the concept of a full graph decomposition in section 3.2.

Section 3.3 outlines how single quasi-particle properties, in particular the one quasi-particle dispersion and excitation gap, can be extracted from H_{eff}. Lastly, we will discuss extrapolation techniques to improve the description of the excitation gap in section 3.4. This wraps up the procedure we apply to find a possible continuous phase transition out of the weak-interaction-strength limit.

3.1. Perturbative continuous unitary transformations

This section introduces the method of perturbative continuous unitary transformations (pCUT). The goal is to transform the initial Hamiltonian, which can not be solved exactly, into an effective model, H_{eff}, given as a perturbative series expansion. The transformation is constructed in such a way that H_{eff} is block diagonal in the quasi-particle number Q and acts on subspaces of the full Hilbert space where Q is fixed.

We start by briefly describing the method of continuous unitary transformations (CUT) which the applied perturbative approach is based on. It was introduced independently by Wegner [57] and Wilson and Glazek [58] and aims at simplifying the Hamiltonian describing a quantum many-body system by a unitary transformation into a more 'suitable' basis. While this endeavor seems trivial for single- or few-particle systems, it is an involved task for many-body systems with

large Hilbert space dimensions. The idea of CUT is to not perform the unitary transformation at once but in a continuous fashion. Formally, one applies infinitely many infinitesimal unitary transformations via a flow parameter $l \in \mathbb{R}_{\geq 0}$ such that the Hamiltonian at a point l during the transformation is given by

$$H(l) = U^\dagger(l) H U(l)\,. \tag{3.1}$$

By letting l flow from zero to infinity, the initial untransformed Hamiltonian $H = H(0)$ flows to the final fully transformed effective Hamiltonian $H_{\text{eff}} = \lim_{l\to\infty} H(l)$. This idea so far still does not answer the question of how to choose the unitary transformation U. By expressing the unitary transformation in terms of its infinitesimal generator $\eta(l)$ with

$$\eta(l) = -U^\dagger(l)\partial_l U(l)\,, \tag{3.2}$$

this boils down to the task of choosing a suitable infinitesimal generator. The rate of change of the Hamiltonian during the course of the transformation is given by the flow equation

$$\partial_l H(l) = [\eta(l), H(l)]\,, \tag{3.3}$$

which is obtained by taking the derivative of Equation (3.1) with respect to l.

Before discussing the generator used for pCUT, let us introduce the requirements of a system in order to apply the pCUT method [59]:

1. The Hamiltonian H can be decomposed in the following way: $H = H_0 + \lambda H_1$.
2. The unperturbed Hamiltonian is bounded from below and has an equidistant spectrum. Formally, this allows writing H_0 as

   $$H_0 = \sum_i (\epsilon_0 + \Delta n_i) = E_0 + \Delta Q\,.$$

   As already described in section 2.1 we can interpret such a Hamiltonian in a quasi-particle language. The ground state is given by the vacuum and elementary excitations above the vacuum correspond to the addition of quasi-particles where due to the equidistant spectrum each quasi-particle adds the same energy Δ to the system. The total number of quasi-particles in the system is given by the quasi-particle number operator Q.
3. The perturbation H_1 can be written in terms of the quasi-particles of the unperturbed system H_0 as

   $$H_1 = \sum_{n=-N}^{N} T_n\,,$$

   where $[Q, T_n] = nT_n$, i.e. T_n changes the number of quasi-particles in the system by n. The perturbation thus connects subspaces with different quasi-particle numbers, where the difference in quasi-particle number is bounded from above by $N \in \mathbb{N}_0$.

As can easily be confirmed, the FSS model meets these requirements (see Equations (2.9) and (2.10)). We now restrict ourselves to formulating the ansatz for pCUT and then jump directly to the resulting effective Hamiltonian. More details on the derivation and the method itself can be found in [59].

With the goal of transforming H into an effective model which conserves the quasi-particle number, the quasi-particle conserving generator is used [59],

$$\eta(l) = \sum_{k=1}^{\infty} \lambda^k \sum_{|\underline{m}|=k} \operatorname{sgn}\left(M(\underline{m})\right) F\left(l;\underline{m}\right) T\left(\underline{m}\right) , \tag{3.4}$$

with the following notation:

$$\begin{aligned} \underline{m} &= (m_1, m_2, \ldots, m_k) \quad \text{with} \quad m_i \in \{0, \pm 1, \ldots, \pm N\} , \\ T\left(\underline{m}\right) &= T_{m_1} T_{m_2} \ldots T_{m_k} , \\ M\left(\underline{m}\right) &= \sum_{i=1}^{k} m_i . \end{aligned}$$

For writing down the Hamiltonian at a stage during the transformation defined by l the following ansatz is made [59]:

$$H(l) = H_0 + \sum_{k=1}^{\infty} \lambda^k \sum_{|\underline{m}|=k} F\left(l;\underline{m}\right) T\left(\underline{m}\right) . \tag{3.5}$$

This resembles a series expansion of H_1 in the perturbation parameter λ. For a given perturbation order k all possibilities for virtual excitation processes in that order are encoded in the vector $\underline{m}$ of length k. The product $T\left(\underline{m}\right)$ of the according T_n operators creates these processes. Each possible process is weighted by a real-valued coefficient function $F(l;\underline{m})$.
Inserting Equations (3.4) and (3.5) into the flow equation in Equation (3.3) yields an infinite set of coupled differential equations for the $F(l;\underline{m})$. The limit of interest for the effective Hamiltonian is $l \to \infty$. When solving the set of differential equations, all $F(l;\underline{m})$ with $M(\underline{m}) \neq 0$ are zero in this limit (for details see [59]). This is ensured by the signum function $\operatorname{sgn}\left(M(\underline{m})\right)$ in the generator (Equation (3.4)): when $M(\underline{m}) = 0$, the generator vanishes and the final step of the transformation, H_{eff}, is reached. Physically, this means that only processes which conserve the total number of quasi-particles in the system survive. The set of differential equations can be solved order by order, with the maximal order limited by computational resources.

With the weights $F(l \to \infty;\underline{m})$ determined, we can write down an effective Hamiltonian

$$H_{\text{eff}} = H_0 + \sum_{k} \lambda^k \sum_{\substack{|\underline{m}|=k \\ M(\underline{m})=0}} C(\underline{m}) T(\underline{m}) , \tag{3.6}$$

with model-independent coefficients $C(\underline{m}) := F(\infty;\underline{m})$. By construction, the effective model only contains processes with $M(\underline{m}) = 0$, i.e., processes which conserve the quasi-particle number Q, and is thus block diagonal with respect to Q. Since the coefficients $C(\underline{m})$ are model-independent, they only have to be calculated once. Note that in this calculation of the $C(\underline{m})$, the energy spacing Δ of the unperturbed system is set to one. Thus, the investigated Hamiltonian has to be rescaled such that the unperturbed energy of one quasi-particle is normalized to one, which is exactly what we already did in subsection 2.1.2 and section 2.2.

The model-specific task is now to identify the respective T_n operators. As we already brought the FSS Hamiltonian into the required form in Equation (2.10), we can simply read them off as

follows:

$$T_0 = \frac{1}{8}\sum_{i\neq j} r_{ij}^{-6}\left((1+\cos\phi)^2 - 4\cos\phi\,(1+\cos\phi)\,\tilde{n}_i + 4\cos^2\phi\,\tilde{n}_i\tilde{n}_j + \sin^2\phi\left(\tilde{b}_i^\dagger\tilde{b}_j + \text{h.c.}\right)\right),$$
$$T_{+1} = \frac{1}{8}\sum_{i\neq j} r_{ij}^{-6}\left(2\sin\phi\,\tilde{b}_i^\dagger - 2\cos\phi\sin\phi\left(2\tilde{b}_i^\dagger\tilde{n}_j - \tilde{b}_i^\dagger\right)\right) = T_{-1}^\dagger\,,$$
$$T_{+2} = \frac{1}{8}\sum_{i\neq j} r_{ij}^{-6}\sin^2\phi\,\tilde{b}_i^\dagger\tilde{b}_j^\dagger = T_{-2}^\dagger\,.$$

The perturbation parameter is given by the rescaled interaction strength, $\lambda = V/2\tilde{\Delta}$, and we define $r_{ij} = |\boldsymbol{r}_i - \boldsymbol{r}_j|$. In the case of the TFIM, we can read off the T_n operators from Equation (2.14):

$$T_0 = \sum_{i<j} r_{ij}^{-6}\left(b_i b_j^\dagger + b_i^\dagger b_j\right),$$
$$T_2 = \sum_{i<j} r_{ij}^{-6} b_i^\dagger b_j^\dagger = T_{-2}^\dagger\,.$$

Here the perturbation parameter is given by $\lambda = J/2h$. Note that for the TFIM the complexity of the T_n operators is reduced drastically compared to the full FSS model. This reduces the computational resources in the remaining task of evaluating the T_n operator sequences in H_{eff}.

3.2. Linked cluster theorem and graph decompositions

After applying the pCUT method to the initial Hamiltonian, we have obtained an effective model H_{eff} which is block diagonal with respect to the quasi-particle number Q. Still, this model is given in terms of T_n operator sequences and the task of actually evaluating physical quantities in the thermodynamic limit remains. For such evaluations, we need to calculate matrix elements between various n quasi-particle states. In this section we will outline why - for effective pCUT Hamiltonians - it is sufficient to consider states on finite linked clusters to still obtain series expansions of the matrix elements which are valid in the thermodynamic limit.

We start by taking a closer look at the structure of the effective Hamiltonian in Equation (3.6) on the lattice which it is defined on. The lattice consists of *sites* which the atoms are placed on, and *bonds* linking these sites where the perturbation acts on. In our specific model, we consider interactions between the three nearest neighbors (considering the truncation of the long-range interaction motivated in section 2.1) and hence all sites which are third-nearest neighbors or closer are linked by a bond. As we are dealing with different interaction strengths (depending on the distance between sites), there are three different types of bonds (also referred to as 'colors'). In principle, this viewpoint is already present in Figure 2.2, where exactly this setup of sites and bonds with three different colors is illustrated.

The interaction is expressed in terms of T_n operators, which by definition create (or annihilate if $n < 0$) n quasi-particles. As discussed in Ref. [60], each operator T_n can be further decomposed by specifying *where* these quasi-particles are created (annihilated),

$$T_n = \sum_l \tau_{n,l}\,,$$

where l labels the bond between two distinct sites. In the definition of the model-specific T_n operators, these bonds were specified by labeling the sites it connects by i and j. The full product sequence of T_n operators appearing in $T(\underline{m})$ in order k can thus be expressed by

$$T(\underline{m}) = \sum_{l_1,l_2,\ldots,l_k} \tau_{m_1,l_1}\tau_{m_2,l_2}\ldots\tau_{m_n,l_k} ,$$

where $|\underline{m}| = k$. We observe that each sequence $T(\underline{m})$ acts on a finite set of links l_i, which defines a finite cluster $C_k = l_1 \cup l_2 \cup \cdots \cup l_k$ whose size is defined by the perturbation order k. With this in mind, we can rewrite the effective Hamiltonian up to order $k_{\max}$ in the perturbation as a sum over finite clusters C_k containing links $l_1, l_2, \ldots, l_k$:

$$H_{\text{eff}} = H_0 + \sum_{k=1}^{k_{\max}} \lambda^k \sum_{\substack{|\underline{m}|=k \\ M(\underline{m})=0}} C(\underline{m}) \sum_{C_k:=\cup_i l_i} \tau_{m_1,l_1}\tau_{m_2,l_2}\ldots\tau_{m_k,l_k} . \tag{3.7}$$

Note that the maximal perturbation order $k_{\max}$ is limited by computational resources. The crucial point, which will allow the restriction of the sum in Equation (3.7) to finite *linked* clusters C_k, is a certain property of H_{eff}, namely its cluster additivity.
Formally, we define a finite cluster C of the whole lattice as a finite subset of sites and all their linking bonds. Two clusters A and B can be either disconnected, if they do not share a site and are not connected by a link ($A \cup B = 0$), or linked otherwise. Consider now an operator $\mathcal{O}^C$ acting on the cluster $C = A \cup B$ given by two disconnected clusters A and B. $\mathcal{O}^C$ is called cluster additive if it holds that

$$\mathcal{O}^C = \mathcal{O}^A \otimes \mathrm{id}^B + \mathrm{id}^A \otimes \mathcal{O}^B , \tag{3.8}$$

where $\mathcal{O}^A$ denotes the operator $\mathcal{O}^C$ which only acts on the subset $A \subset C$ of the full cluster[1]. One can show (see Ref. [61]) that the effective pCUT Hamiltonian H_{eff} is cluster additive (the flow equations (3.3) conserve the cluster additivity of operators [62]).

The cluster additivity of H_{eff} implies that contributions of disconnected clusters C_k in Equation (3.7) cancel out and it is sufficient to calculate only on linked clusters (linked cluster theorem) [63].
A nice implication of the cluster additivity of H_{eff} is that physical quantities up to perturbation order $k_{\max}$ can be calculated in the thermodynamic limit on such finite linked clusters. As the perturbation is local - in a sense that the T_n operators it is comprised of act of pairs of sites (i, j) connected by a bond with finite distance - in perturbation order k only processes involving k bonds contribute. This limits the length scale of corresponding linked processes to $\propto k$, and it is thus sufficient to calculate on finite linked clusters.

The natural route is to choose one cluster, which is sufficiently large such that all virtual fluctuations in the considered perturbation order $k_{\max}$ fit on it without being influenced by its boundaries, and evaluate all matrix elements of H_{eff} on this cluster (which contains all clusters C_k in Equation (3.7)). However, both computational time and memory grow exponentially with the cluster size which restricts the order $k_{\max}$ that can be reached. Furthermore, unlinked processes are still included in such a calculation. For optimizing computational efforts one should therefore always choose the smallest possible cluster. We do this for the FSS model introduced

[1] Note that the decomposition in Equation (3.8) is not possible for every operator $\mathcal{O}^C$ acting on the Hilbert space of the full cluster C, hence the explicit notion of cluster additivity.

in section 2.1. For the transverse-field Ising model introduced in section 2.2 we choose to further perform a full decomposition of this cluster into graphs in order to push the achievable perturbation order of our results. Similarly to a cluster, a graph is defined by vertices (sites) which are connected by edges (bonds). The perturbation acts on these edges. Keeping the linked cluster theorem in mind, it is obvious that only connected graphs contribute. In a given perturbation order $k_{\max}$, graphs with up to $k_{\max}$ edges can contribute.

The idea of a graph decomposition is to identify topologically identical structures (graphs) within the cluster, on which the effective Hamiltonian is equivalent. We can then optimize our calculations by only evaluating the contribution of such identical structures once. Consequently, the first task is to generate all topologically different graphs relevant in perturbation order $k_{\max}$. This is done by an algorithm provided by Matthias Mühlhauser (AG Schmidt, [64]). We will not dive further into the procedure of efficiently generating all relevant graphs. For details on this see for example Ref. [65].

With the decomposition of the effective Hamiltonian in Equation (3.7), it is reduced to a sum over all graph contributions. Minimizing computational resources by only evaluating equivalent structures once requires some further work for this summation. As a graph can be realized multiple times on the lattice, it does not suffice to simply sum over all considered graphs. Instead, we have to determine how often each graph is found on the lattice in relation to the number of sites, which defines an embedding factor. The sum over contributions from all linked clusters is then recovered by adding up the obtained graph contributions weighted by the corresponding embedding factors. In other words, we add the contributions of all embeddings of a graph into the lattice. For example, the ground-state energy per site is given by

$$E_0/N = \sum_{g \subseteq G} c(g)\epsilon_0(g)\,,$$

where the sum runs over all relevant graphs g in the cluster G, $c(g)$ is the embedding of the corresponding graph and $\epsilon_0(g)$ is the reduced ground-state energy of the graph. Note that in order to avoid multiple counting of fluctuations, it is necessary to consider the reduced contribution of the graph, which is given by subtracting the contributions of all subgraphs g':

$$\epsilon_0(g) = E_0(g) - \sum_{g' \subset g} \epsilon_0(g')\,.$$

With this, only fluctuations which act on the entire graph, i.e. touch all bonds, are considered.

As mentioned in the beginning of the section, we are dealing with a truncated long-range interaction and thus three different 'colors' of bonds with three different interaction strengths $V_{1,2,3}$. In the perturbative setup, those are all represented by the same perturbation parameter $\lambda = V/2\tilde{\Delta}$ with the algebraic decay of the interaction strength contained in the T_n operators. We implement this by assigning operators $T_n^{(i)}$ with $i \in \{1,2,3\}$ and perturbation parameters $\lambda^{(i)}$ to each bond color. We leave these $\lambda^{(i)}$ variable, so that our results are not limited to the algebraic decay with $\alpha = 6$ and we are able to choose arbitrary ratios between V_1, V_2 and V_3. For multiple bond colors, the number of graphs generated by the standard scheme grows exponentially. One can solve this problem by applying a white graph expansion [60]. Here, the color of the bonds is neglected in the generation of the relevant graphs. Instead, a distinct perturbation parameter is used for each bond, resulting in the matrix elements being obtained as a power series in multiple perturbation operators λ. The actual lattice geometry is then reintroduced by the embedding

of those graphs into the lattice and the according resubstitution of the perturbation parameters $\lambda^{(i)}$. Note that for a white graph expansion it is required that the actual operators acting on the bonds are independent of the bond color and only the coefficients vary. Although additional bookkeeping is required, the overall computational effort is reduced by this scheme.

3.3. Extraction of individual quasi-particle channels

In section 3.1 an effective Hamiltonian H_{eff} which is block diagonal in the quasi-particle number was derived using the pCUT method. In the following section, we discuss the structure of H_{eff} in more detail and describe how to extract individual n quasi-particle channels (in particular the single quasi-particle channel), following Ref. [61].

We can write the effective Hamiltonian as a sum over the independent n quasi-particle operators,

$$H_{\text{eff}} = \sum_n H_n \,, \tag{3.9}$$

where H_n is an irreducible operator acting on n quasi-particles. More specifically, H_n describes a hopping or interaction process involving n quasi-particles. In the most general form we can write this by summing over all possible combinations of lattice sites involved in the process, and taking the product of corresponding annihilation and creation operators weighted with the according coefficient t. In normal ordered form, the operator H_n then reads

$$H_n = \sum_{\substack{i_1,\ldots,i_n \\ j_1,\ldots,j_n}} t_{i_1,\ldots,i_n \to j_1,\ldots,j_n} b^\dagger_{j_1} \ldots b^\dagger_{j_n} b_{i_1} \ldots b_{i_n} \,. \tag{3.10}$$

The ground-state properties of the system are defined by H_0. The dynamics of a single quasi-particle are contained in H_1. Interactions between two or more quasi-particles are described by H_2 and so on. For the location of possible second-order phase transitions, we investigate the ground-state energy and single quasi-particle channels.

When looking at Equation (3.9) it becomes clear that in order to extract the true n quasi-particle contribution it does not suffice to simply apply H_{eff} to a n quasi-particle state, as this would contain contributions from lower particle channels. Instead, we have to look at the restriction of H_n to the n quasi-particle subspace:

$$H_n|_n = H_{\text{eff}}|_n - \sum_{i=1}^{n-1} H_i|_n \,. \tag{3.11}$$

Here we define the restricted operator $H|_n$ acting on the subspace $\mathcal{H}_n \subset \mathcal{H}$ which is spanned by n quasi-particle states. This implies the relation $H_n|_m = 0$ for $m < n$, which is used in writing down Equation (3.11). Note that in contrast to H_{eff} and H_n, $H_{\text{eff}}|_n$ itself is not cluster additive [61]. We can now iteratively extract individual n quasi-particle channels from the effective Hamiltonian.

Let us apply the discussed insights to our task of evaluating the contributions of the ground state and the single quasi-particle channel. We start by calculating the energy of the ground state, or the zero quasi-particle channel. Using Equation (3.11), the ground-state energy per site is

obtained by applying H_0 to the vacuum state $|0\rangle$:

$$\epsilon_0 = \frac{\langle 0|H_0^A|0\rangle}{N^A} = \frac{\langle 0|H_{\text{eff}}^A|0\rangle}{N^A} = \frac{E_0^A}{N^A} \,. \tag{3.12}$$

Note that here H_0 does not denote the unperturbed Hamiltonian but the zero quasi-particle restricted Hamiltonian from Equation (3.9). N^A denotes the total number of sites in the cluster A on which the Hamiltonian is evaluated, as indicated by the superscript.
We further want to calculate the energy of one quasi-particle (more specifically, the energy difference to the vacuum) or the one quasi-particle dispersion. For this we have to investigate the restricted H_1, which according to Equation (3.11) is given by

$$H_1|_1 = H_{\text{eff}}|_1 - H_0|_1 \,. \tag{3.13}$$

The physical meaning of this quantity becomes clear when it is written in normal ordering as introduced in Equation (3.10). We obtain the expression

$$H_1 = \sum_{i,j} t_{i\to j}\, b_j^\dagger b_i \,, \tag{3.14}$$

which describes all single quasi-particle hopping processes from site i to site j. Indeed, here we can see that H_1 describes the *pure* single quasi-particle channel. We are interested in the coefficients of these hopping processes, also termed hopping amplitudes. Using Equation (3.13) we obtain

$$t_{i\to j} = \langle 1;j|H_1|1;i\rangle = \langle 1;j|H_{\text{eff}}^A|1;i\rangle - \underbrace{\langle 0|H_0^A|0\rangle}_{E_0^A}\delta_{ij} \,, \tag{3.15}$$

where $|1;i\rangle$ denotes a state with one quasi-particle at site i. Note that the subtraction of E_0^A is essential in order to preserve the cluster additivity [66]. It is crucial that all quantities are calculated on the same cluster A. Only then the resulting hopping amplitudes are valid in the thermodynamic limit and independent of the cluster (i.e. have no cluster indicated).

Due to the translational invariance of the lattice we can reduce the degrees of freedom in Equation (3.10) using a Fourier transformation into momentum space. We describe the lattice in terms of its unit cell which is repeatedly placed at integer multiples of its translational lattice vectors. For a definition of the lattice vectors, see Equation (2.3) and Equation (2.4) in subsection 2.1.1. Remember that the elementary unit cell of the link-Kagome lattice has six sites. Previously, we introduced a one quasi-particle state by denoting the site i the quasi-particle is placed at without considering this decomposition of a lattice into its unit cells. Taking this into account, we can write such a state in the spatial domain more explicitly as

$$|i\rangle \mathrel{\widehat{=}} |\boldsymbol{R}_i, \alpha\rangle \,, \tag{3.16}$$

where we omit the '1' specifying a *one* quasi-particle state. Here $\boldsymbol{R}_i$ is the position of the unit cell in which site i is contained and $\alpha = 1,\ldots,6$ specifies the site within the unit cell according to the convention introduced in Figure 2.1. The position of the site is thus given by $\boldsymbol{R}_i + \boldsymbol{\delta}_\alpha$.
The one quasi-particle states in momentum space are obtained by Fourier transformation,

$$|\boldsymbol{k}, \alpha\rangle = \frac{1}{\sqrt{N_{\text{uc}}}} \sum_{\boldsymbol{R}} \mathrm{e}^{-i\boldsymbol{k}\boldsymbol{R}} |\boldsymbol{R}, \alpha\rangle \,, \tag{3.17}$$

with momentum $\boldsymbol{k}$ and number of unit cells $N_{\mathrm{uc}} = N/6$.

Due to the translational invariance, only the relative positions of two sites i and j are relevant for the hopping amplitude. Using the notation for the spatial domain introduced in Equation (3.16) we can write the hopping amplitude between sites (i, α) and (j, β) with relative position of unit cells $\boldsymbol{d}$ as

$$t_{(i,\alpha)\to(j,\beta)} := t_{\boldsymbol{d}}^{\beta\alpha} = \langle \boldsymbol{R}_j, \beta | H_1 | \boldsymbol{R}_i, \alpha \rangle \quad \text{with} \quad \boldsymbol{d} = \boldsymbol{R}_j - \boldsymbol{R}_i \,.$$

Note that the range of the hopping, $\boldsymbol{d} + \boldsymbol{\delta}_\beta - \boldsymbol{\delta}_\alpha$, is limited by the finite perturbation order $k_{\max}$ of the effective Hamiltonian.
We can now write down the action of H_1 on a one quasi-particle state in momentum basis. Using Equation (3.14) we obtain:

$$\begin{aligned}
H_1|\boldsymbol{k}, \alpha\rangle &= \sum_{(i,\gamma),(j,\delta)} t_{(i,\gamma)\to(j,\delta)}\, b^\dagger_{(\boldsymbol{R}_j,\delta)} b_{(\boldsymbol{R}_i,\gamma)} |\boldsymbol{k}, \alpha\rangle \\
&= \frac{1}{\sqrt{N_{\mathrm{uc}}}} \sum_{(i,\gamma)} \sum_{\boldsymbol{d},\delta} \sum_{\boldsymbol{R}} t_{\boldsymbol{d}}^{\delta\gamma} \mathrm{e}^{-i\boldsymbol{k}\boldsymbol{R}}\, b^\dagger_{(\boldsymbol{R}_i+\boldsymbol{d},\delta)} \underbrace{b_{(\boldsymbol{R}_i,\gamma)} |\boldsymbol{R}, \alpha\rangle}_{\delta_{\boldsymbol{R}_i \boldsymbol{R}} \delta_{\gamma\alpha} |0\rangle} \\
&= \frac{1}{\sqrt{N_{\mathrm{uc}}}} \sum_{\boldsymbol{d},\delta} \sum_{\boldsymbol{R}} t_{\boldsymbol{d}}^{\delta\alpha} \mathrm{e}^{-i\boldsymbol{k}\boldsymbol{R}}\, |\boldsymbol{R} + \boldsymbol{d}, \delta\rangle \\
&= \frac{1}{\sqrt{N_{\mathrm{uc}}}} \sum_{\boldsymbol{d},\delta} \sum_{\boldsymbol{R}} t_{\boldsymbol{d}}^{\delta\alpha} \mathrm{e}^{-i\boldsymbol{k}(\boldsymbol{R}-\boldsymbol{d})}\, |\boldsymbol{R}, \delta\rangle \\
&= \sum_{\boldsymbol{d},\delta} t_{\boldsymbol{d}}^{\delta\alpha} \mathrm{e}^{i\boldsymbol{k}\boldsymbol{d}}\, |\boldsymbol{k}, \delta\rangle \\
&=: \sum_{\delta} (H_k)_{\delta\alpha} |\boldsymbol{k}, \delta\rangle \,.
\end{aligned}$$

The total momentum is conserved due to the translational invariance. In matrix representation, we see this as H_1 is block diagonal in momentum space and decomposes into blocks with specific total momentum. The elements of the 6×6 matrix H_k are given by

$$(H_k)_{\beta\alpha} = \langle \boldsymbol{k}, \beta | H_1 | \boldsymbol{k}, \alpha \rangle = \sum_{\boldsymbol{d}} t_{\boldsymbol{d}}^{\beta\alpha} \mathrm{e}^{i\boldsymbol{k}\boldsymbol{d}} \quad \text{with} \quad \alpha, \beta = 1, \ldots, 6 \,.$$

Hence, we have reduced the dimensionality of our problem exploiting the translational invariance of the lattice. We can now diagonalize this matrix in order to obtain the energy eigenvalues of one quasi-particle (in the thermodynamic limit). In order to investigate whether a continuous phase transition occurs, we will look at the lowest energy eigenvalue and also refer to this as the one quasi-particle excitation gap Δ. In the next section, we describe the extrapolation methods used to investigate the excitation gap which is given as a series expansion.

3.4. (Dlog)Padé extrapolations

We obtain our results for the one quasi-particle dispersion as series in the perturbation parameter λ. By nature of perturbation theory these results are only valid for small values of λ. We are interested in describing quantum phase transitions of the system happening at a critical value λ_c. It is obvious that this is only possible if λ_c lies within the convergence radius of our series

expansion in the obtained order. A quantum phase transition is characterized by a non-analyticity in the ground-state energy with respect to λ. Close to the critical point λ_c of a continuous phase transition, which is the type of phase transition we investigate, the elementary excitation gap Δ vanishes with a power-law behavior like [67]

$$\Delta \propto |\lambda - \lambda_c|^{z\nu} , \tag{3.18}$$

with dynamical critical exponent z and correlation length critical exponent ν. Such a behavior can not be modeled by a simple polynomial series. In order to overcome this problem and extract critical points and exponents of a potential continuous phase transition we apply extrapolation techniques. In the following, we introduce the Padé and DlogPadé extrapolation techniques. A more detailed discussion and derivation can be found for example in Refs. [68] and [69].

As stated before, our results are given as a power series in the perturbation parameter λ,

$$F(\lambda) = \sum_{i=0}^{m} a_i \lambda^i = a_0 + a_1\lambda + a_2\lambda^2 + ... + a_m\lambda^m , \tag{3.19}$$

with coefficients $a_i \in \mathbb{R}$. The order m of the polynomial is determined by the maximally obtained perturbation order. We now interpret this as the Taylor expansion of a rational function. The $[L, M]$ Padé approximant of $F(\lambda)$ is defined as

$$P[L, M]_F(\lambda) := \frac{P_L(\lambda)}{Q_M(\lambda)} = \frac{p_0 + p_1\lambda + ... + p_L\lambda^L}{q_0 + q_1\lambda + ... + q_M\lambda^M} . \tag{3.20}$$

The coefficients $p_i, q_i \in \mathbb{R}$ with $q_0 = 1$ are uniquely defined by a set of linear equations given by the requirement that the Taylor expansion of $P[L, M]_F(\lambda)$ up to order m is equal to $F(\lambda)$,

$$F(\lambda) = \mathcal{T}^m_{P[L,M]_F}(\lambda) .$$

For a series up to order m one can calculate all Padé approximants with $L + M \leq m$. For each extrapolant, we determine the critical value λ_c as the zero of $P[L, M]_F(\lambda)$.

In general, Padé extrapolants with $L + M$ close to m approximate the actual behavior better as they include higher orders of the perturbative series expansion. We assume that the extrapolation approximates the underlying function well if many different extrapolants show quantitative similar behavior for the desired quantity. Note that a Padé extrapolant exhibits poles if its denominator $Q_M(\lambda)$ becomes zero. Such a pole can be of physical origin and indicate a quantum phase transition. For a continuous phase transition as in Equation (3.18) however, we expect no poles in the interval $[0, \lambda_c]$. Also, unphysical poles can occur which do not correspond to any physical behavior of the system. If a pole appears isolated and before the critical value, it is likely not of physical origin and the corresponding Padé extrapolant is called defective and is sorted out.

Padé approximants can only describe singularities with integer critical exponent. Thus, we cannot extract the critical exponent $z\nu$ from Padé extrapolations. To accomplish this, we additionally perform DlogPadé extrapolations of the series in Equation (3.19), which are better suited for modeling the behavior close to a continuous phase transition as they allow for arbitrary critical exponents. The DlogPadé extrapolation scheme uses the logarithmic derivative of $F(x)$,

$$D(x) := \frac{\mathrm{d}}{\mathrm{d}x} \ln F = \frac{F'(x)}{F(x)} , \tag{3.21}$$

and determines its $[L, M]$ Padé approximant which is defined as

$$P[L,M]_D(\lambda) := \frac{P_L(\lambda)}{Q_M(\lambda)} = \frac{p_0 + p_1\lambda + ... + p_L\lambda^L}{q_0 + q_1\lambda + ... + q_M\lambda^M}\,, \tag{3.22}$$

with $p_i, q_i \in \mathbb{R}$. Here one order is 'lost' due to the derivative and we have $L+M \leq m-1$. In order to obtain the extrapolant of the original power series $F(\lambda)$ we define the DlogPadé extrapolant as

$$\mathrm{d}P[L,M]_F(\lambda) = \exp\left(\int_0^\lambda \mathrm{d}\lambda' P[L/M]_D(\lambda')\right)\,.$$

Now assume the true physical function $f(\lambda)$ which we approximate with our series $F(\lambda)$ is given by a power law behavior close to the critical point λ_c as:

$$f(\lambda) \propto \left(1 - \frac{\lambda}{\lambda_c}\right)^{-\theta}\,.$$

The logarithmic derivative is given by

$$\frac{\mathrm{d}}{\mathrm{d}\lambda}\ln f(\lambda) = \frac{\theta}{\lambda_c - \lambda}\,,$$

which has a single pole at $\lambda = \lambda_c$. The Padé extrapolant of the logarithmic derivative defined in Equation (3.22) should thus exhibit a pole at $\lambda = \lambda_c$ and we can determine λ_c from the zeros of $Q_M(\lambda)$. Further, we can extract the critical exponent θ as

$$\theta = \left.\frac{P_L(\lambda)}{\frac{\mathrm{d}}{\mathrm{d}\lambda}Q_M(\lambda)}\right|_{\lambda=\lambda_c}\,. \tag{3.23}$$

Note that the obtained value for θ depends heavily on the value λ_c extracted from the extrapolation.
Often it is useful to structure the Padé and DlogPadé extrapolants into families. A family is a set of extrapolants $P[L, M]$ or $dP[L, M]$ which have the same difference $d = L - M$ between the degree of numerator and denominator polynomial. One can then study the convergence behavior of e.g. λ_c with the perturbation order m within a family.

3.5. Summary and implementation of the approach

To end this chapter, we summarize the approach we follow in the investigation of the weak-interaction-strength limit of the FSS model and of the contained TFIM. The Hamiltonian of interest is decomposed into an exactly solvable unperturbed part H_0 and a perturbation H_1 with perturbation parameter λ, as presented in chapter 2. The investigated Hamiltonians fulfill all requirements needed to apply the pCUT method which transforms H into an effective Hamiltonian H_{eff}, which is given in form of a series expansion in λ up to a maximal order $k_{\max}$. H_{eff} is block diagonal in the quasi-particle number and cluster additive. This allows us to perform a linked cluster expansion and optimize the numerical evaluation by means of a full graph decomposition of the cluster. We extract the zero and one quasi-particle channels from H_{eff}. By performing a Fourier transformation, we reduce the dimensionality of the one quasi-particle contribution to

a 6×6 matrix which we diagonalize to find the lowest energy eigenvalue, i.e. the elementary excitation gap. We perform Padé and DlogPadé extrapolations of the gap to extract critical point and exponent of a potential continuous phase transition.

The calculation of individual needed matrix elements of H_{eff} is achieved using an implementation of the AG Schmidt. It requires the definition of H_0 and T_n operators of the considered model, along with a definition of the sites and geometry of bonds within the lattice. Similarly, the graph decomposition is performed using an implementation by the AG Schmidt, which generates all relevant graphs up to a given order for a given cluster. Then, the matrix element between a bra- and ket-state is calculated up to a given perturbation order $k_{\max}$ as series in the perturbation parameters $\lambda^{(i)}$. The appropriate combination of individual hopping elements in order to calculate the one quasi-particle dispersion is achieved by a python code written by myself.

4. Ground-state energy minimization approach in the classical limit

In the previous chapter (3) we outlined the method used to investigate the weak-interaction-strength limit, $V \ll \tilde{\Delta}$, of the FSS model on the link-Kagome lattice, which composes the bulk part of the work done for this thesis. As an addition to this, we also investigate the classical limit of the FSS model where $\Omega = 0$. The terminology 'classical' arises from thereby excluding quantum fluctuations from the model. The resulting ground states are given by crystalline structures. The algorithm used for the determination of these ground states was developed by Jan Koziol and will be outlined in this chapter. A more detailed description of the algorithm can be found in the corresponding publication [46]. It is based on the idea to evaluate the energy of the crystalline structures in the thermodynamic limit on the unit cell of the respective ordering pattern. By searching for the energetically best order among all unit cells of the lattice up to a certain extent, the ground state is found. The algorithm can be applied to general bosonic lattice models with long-range density-density interactions which decay algebraically with decay exponent α. In such a general model each site can be occupied by multiple bosons with an onsite repulsion strength U. The hardcore restraint of our model translates to setting $U = \infty$. The application to bosonic models with finite U on different lattice geometries and thereby obtained findings is also discussed in Ref. [46].

The classical limit of the FSS model is given by setting $\Omega = 0$ in Equation (2.1),

$$H_{\text{class}}^{\text{FSS}} = -\delta \sum_i n_i + \frac{1}{2} \sum_{i \neq j} V_{ij} n_i n_j \,. \tag{4.1}$$

Expressed in the hardcore bosonic basis with creation operators $b_i^\dagger$ and annihilation operators b_i, the Hamiltonian is diagonal in the particle number $n_i = b_i^\dagger b_i$. An eigenstate of the system is given by a distribution of an arbitrary number of hardcore bosons (limited by the number of lattice sites) over the lattice and its energy can be evaluated directly for a finite lattice. The ground state is given by the configuration of bosons which minimizes the total energy. Our goal will be to determine the ground-state phase diagram of this system, taking into account the full long-range interaction (instead of truncating the interaction as in the rest of the thesis).

We can easily gain an intuitive understanding of the physics of the FSS model in the classical limit. The first summand in Equation (4.1) acts as a chemical potential, which energetically favors the occupation of a site with strength $-\delta$. The second summand is a repulsive interaction between two occupied sites i and j with strength $V_{ij} = V/|\boldsymbol{r}_i - \boldsymbol{r}_j|^\alpha$, yielding an energy penalty decreasing with the distance between the two sites. Here, this is the van-der-Waals interaction with $\alpha = 6$. Energetically, this results in a competition between maximizing the energy gain from the overall occupation while minimizing the energy loss from sites occupied close to each other. Finding the ground state of this model boils down to answering the question of how many sites have to be occupied in which configuration (i.e. distance to each other) in order to minimize the energy.

Intuitively, it is clear that the ground-state configuration will depend on the ratio δ/V and that the fraction of occupied sites - the filling fraction f - will increase with increasing δ/V. For $\delta/V \leq 0$, the number of hardcore bosons in the system will be zero as no energy is gained from adding particles to the system and energy is lost from the repulsive interaction. As discussed in section 2.2, the FSS model maps to the Ising model for $\delta/V = \bar{\mu}^\alpha/2$. For $\delta/V \neq \bar{\mu}^\alpha/2$ we have an Ising model with additional longitudinal field. Note that in the calculation of the value $\bar{\mu}^\alpha$, we take the full long-range interaction into account. Using a Matsubara-Matsuda transformation [42] we can relate hardcore bosons to spins such that the empty state corresponds to $\sigma_i^z = +1$ and the full state to $\sigma_i^z = -1$ at each site i. Further, a spin state in a positive longitudinal field can be associated with the corresponding state in a negative field by flipping each spin. Thus, the hardcore bosonic model is particle-hole symmetric[1] around $\delta/V = \bar{\mu}^\alpha/2$ and accordingly, the system is completely filled, meaning each site occupied, for $\delta/V \geq \bar{\mu}^\alpha$ and half filled for $\delta/V = \bar{\mu}^\alpha/2$. However, finding the filling fraction and the realized ordering pattern for an arbitrary given ratio δ/V is not trivial due to the long-range nature of the interaction: each occupied site is coupled to any other occupied site. We thus have to use a more elaborate scheme in order to find the energetically favored ordering pattern. This is outlined in the following.

The approach is based on the idea to calculate the energy of periodic ordering patterns of hardcore bosons on the unit cell of the respective pattern. An example for an ordering pattern with a unit cell[2] consisting of two elementary unit cells and its translational vectors $\boldsymbol{T}_1$ and $\boldsymbol{T}_2$ is illustrated in Figure 4.1.

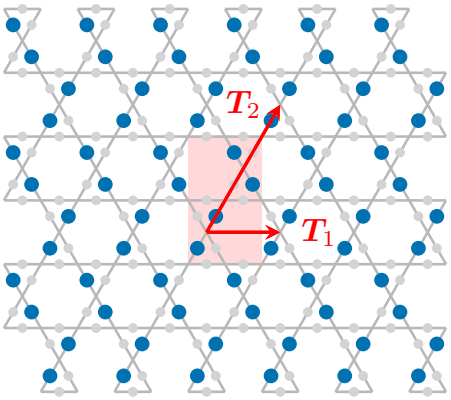

Figure 4.1.: Exemplary ordering structure of hardcore bosons in the classical limit. Sites occupied by one boson are shown in blue ● , unoccupied sites in light gray ● . The unit cell of the ordering pattern is highlighted in red and consists of two elementary unit cells for this particular pattern. The translational unit vectors of this unit cell, $\boldsymbol{T}_1$ and $\boldsymbol{T}_2$, are shown as red arrows.

Of course, the long-range interaction couples this unit cell to all other unit cells and we cannot evaluate the energy of the unit cell in the thermodynamic limit directly. At this point, it is necessary to introduce so-called resummed couplings. Loosely speaking, the couplings in between unit cells are absorbed into the couplings within one unit cell, where the couplings between

[1] 'Hole' referring to an unoccupied site, 'particle' to an occupied one.

[2] A note on terminology: here we refer to a unit cell in the context of periodic repetition in the ordering pattern of crystalline structures; if we mean the actual unit cell of the underlying lattice we will explicitly refer to this as the elementary unit cell.

equivalent sites are summarized. Formally, the resummed coupling between two sites at positions $\boldsymbol{r}_i$ and $\boldsymbol{r}_j$ within the unit cell is defined as

$$\tilde{V}_{ij}^{K,\alpha} = V \sum_{k=-K}^{K} \sum_{l=-K}^{K} \frac{1}{|\boldsymbol{r}_i - \boldsymbol{r}_j + k\boldsymbol{T}_1 - l\boldsymbol{T}_2|^\alpha} ,$$

where $\boldsymbol{T}_{1,2}$ are the translational vectors of the unit cell and K is a cut-off for the extent of the resummation. The error due to this cut-off is estimated in order to obtain extrapolated couplings for an infinite resummation, $\tilde{V}_{ij}^{\infty,\alpha}$. For more details, see Ref. [46]. Note that the obtained $\tilde{V}_{ij}^{\infty,\alpha}$ are unit-cell dependent. The resummed couplings then allow to reformulate the Hamiltonian in Equation (4.1) on the unit cell:

$$H_{\text{class}}^{\text{FSS}} = -\delta \sum_i n_i + \frac{1}{2} \sum_{i \neq j} \tilde{V}_{ij}^{\infty,\alpha} n_i n_j + \frac{1}{2} \sum_i \tilde{V}_{ii}^{\infty,\alpha} n_i n_i . \tag{4.2}$$

Now, the site index i runs only over sites contained in the unit cell of the ordering pattern. With this we can evaluate the energy per site of an ordering pattern within the respective unit cell in the thermodynamic limit.

In order to find the energetically favored ordering pattern, we will now investigate all unit cells spanning the lattice up to a certain extent. For an arbitrary lattice with m sites per elementary unit cell and translational lattice spanned by the elementary lattice vectors $\boldsymbol{t}_1, \boldsymbol{t}_2$ these can be generated systematically. For this, it is exploited that the translational lattice,

$$\mathcal{L}(\boldsymbol{t}_1, \boldsymbol{t}_2) := \{p\boldsymbol{t}_1 + q\boldsymbol{t}_2 \,|\, p, q \in \mathbb{Z}\} ,$$

is isomorphic to the integer lattice $\mathbb{Z}^2$ under the map

$$h : \mathcal{L}(\boldsymbol{t}_1, \boldsymbol{t}_2) \to \mathbb{Z}^2 , \quad p\boldsymbol{t}_1 + q\boldsymbol{t}_2 \mapsto (p, q) .$$

More details can be found in Ref. [46]. Then, the translational unit cells of the integer lattice up to a certain extent can be generated independently from the original lattice. The lattice geometry is reintroduced afterwards by inverting the isomorphism, which yields the respective translational unit cells of the original lattice. Finally, the positions of the m sites are added to each elementary unit cell within the translational unit cell.

This leaves us with a set of unit cells up to a certain extent in size. On each of these unit cells we have to find the energetically optimal ordering pattern in the thermodynamic limit. We are dealing with large unit cells as the elementary unit cell of the link-Kagome lattice already consists of six sites, hence it is not possible to calculate the energy of every possible ordering pattern. Instead, a global minimization scheme is applied in order to find the optimal ordering pattern. The main part of this scheme is a local optimization which uses the steepest descent rule in a discrete form. We start with an initial state. Going from there, we want to modify the state step by step until an energetically 'lowest' state is reached. To this end, the following operations are proposed for all pairs of sites i, j and all sites i, respectively:

a) move hardcore boson from site i to site j,

b) insert hardcore boson at site i,

c) remove hardcore boson from site i.

For each proposal, the energy between the original state and the state after the operation, $\Delta E = E_{\text{after}} - E_{\text{before}}$, is evaluated using resummed couplings as introduced before. If the performed operation is energetically beneficial and the new state has a lower energy than the initial state, i.e. $\Delta E < 0$, the corresponding proposed operation is accepted and applied, resulting in a new initial state for which this local optimization is applied. If no operation with $\Delta E < 0$ can be proposed, we conclude that a local minimum is reached and terminate the optimization.

This local optimization is repeated for a number of times which seems sufficient, randomly altering the initial state for each new optimization. We then call the best local minimum the global minimum obtained by the optimization round. In order to improve the robustness of the result, we repeat the optimization until the same global minimum is reached 10 times - without meanwhile finding a lower global minimum. While it is not guaranteed that the true global minimum is found hereby, this scheme suffices for practical purposes.

This global minimization scheme is applied to each unit cell out of the set we are considering. Comparing the optimal configuration on each unit cell, the overall best configuration with the lowest energy between all unit cells is selected as the ordering pattern of the ground state.

For the determination of the phase diagram we proceed as follows: we determine the filling fraction f and the realized ordering pattern for evenly spaced values for $\delta/V \in (0, \bar{\mu}^6)$. Note that with the described method, we cannot rule rule out that there exists an ordering pattern with a unit cell larger than the ones we are considering which is even more energetically beneficial.

5. Discussion of the J_1-J_2-J_3 transverse-field Ising model

We will approach understanding the full FSS model by first investigating the TFIM which is realized for the specific parameter ratio $\delta/V \approx 2.105$ as derived in section 2.2. The Hamiltonian is defined in Equation (2.11). The truncation of the long-range interaction after the third-nearest neighbor leaves us with the three antiferromagnetic interaction strengths $J_1, J_2, J_3 > 0$ which are related by the algebraic decay of the interaction strength J with r^{-6}. We will however extend the discussion of the TFIM to arbitrary $J_{1,2,3}$ in this chapter.

We start our analysis by discussing the limiting cases of setting J_2 (J_3) to zero. The complexity of the lattice geometry and of the hierarchy of the interactions in these cases is reduced compared to the TFIM with algebraically decaying interaction strength. On the one hand, this allows computing higher orders of the series expansion. On the other hand, it is easier for us to understand the mechanisms occurring in the low-field limit. We will then combine our understanding of the two reduced models J_1-J_2 and J_1-J_3 from section 5.1 and section 5.2 into understanding the combined J_1-J_2-J_3 model in section 5.3. Finally, we will turn to the original model with algebraically decaying interaction strength, where the previously gained insights will be beneficial in the interpretation. For all cases, the high-field limit is investigated using the pCUT method combined with a graph decomposition as outlined in chapter 3. After understanding the special case of the TFIM, we will turn to the full FSS model in the next chapter.

5.1. J_1-J_2 transverse-field Ising model

In the following section we begin the investigation by setting $J_3 = 0$ and discuss the resulting J_1-J_2 TFIM. Figure 5.1 shows the lattice geometry with the J_1 and J_2 bonds. We provide a discussion of the high-field limit in subsection 5.1.1 and the low-field limit in subsection 5.1.2. We first analyze the case $J_1 = J_2$ where we do not have to take a hierarchy of bonds into account. The phase transition we find between the two limits in this case is further analyzed in subsection 5.1.3. We then proceed to discuss the model for arbitrary ratios of J_2/J_1 in subsection 5.1.4.

5.1.1. High-field limit for $J_1 = J_2$

We start by discussing the high-field limit $h \gg J$ of the J_1-J_2 TFIM. Following the approach described in chapter 3, we apply the pCUT method to derive a quasi-particle conserving effective Hamiltonian H_{eff} as a series in the perturbation parameter $\lambda = J/2h$. We extract the one quasi-particle channel from H_{eff} and exploit the translational invariance of the lattice to perform a Fourier transformation into momentum space which reduces the problem to a 6×6 matrix H_k. Diagonalizing this matrix yields six eigenstates with corresponding eigenenergies, which depend on the momentum and thus give us the dispersion of one quasi-particle. For $J_1 = J_2 =: J$, we calculate the one quasi-particle dispersion up to order $k_{\max} = 11$. For arbitrary J_1, J_2, we calculate the one quasi-particle dispersion up to order $k_{\max} = 10$. Here we discuss the results for

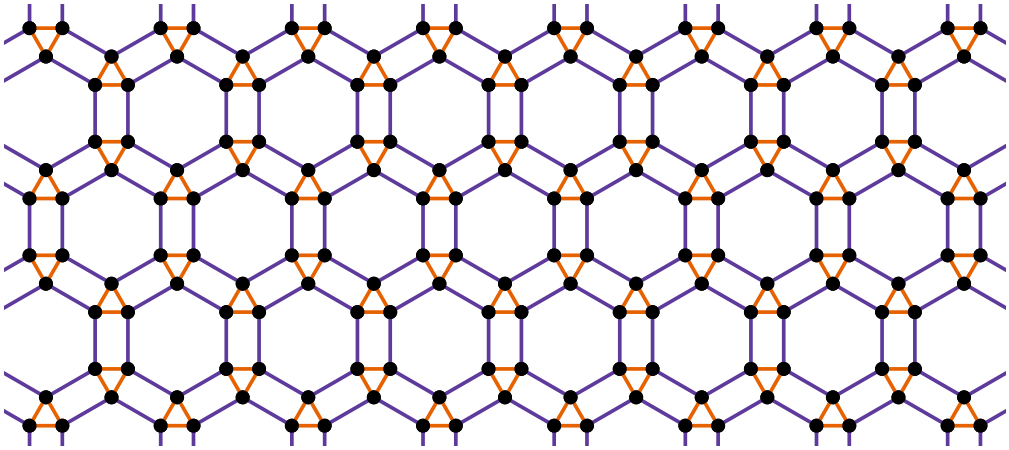

Figure 5.1.: Visualization of the J_1-J_2 lattice. The positions of the spin 1/2 are shown as black circles. The spins interact via bonds with strengths J_1 (orange) and J_2 (purple), resulting in the geometry of the ruby lattice.

$J_1 = J_2$ in detail. For arbitrary J_1, J_2 refer to subsection 5.1.4.

Figure 5.2 shows the six energy eigenvalues obtained by the diagonalization for $\lambda = 0.2$, sorted by energy. The two axes are the coefficients k_1, k_2 of the momentum, defined with respect to the lattice vectors given in Equation (2.3). Note that due to the normalization of the Hamiltonian we obtain the quasi-particle energy in units of $2h$. Thus, the one quasi-particle energy in the unperturbed case for vanishing Ising interaction strength $J = 0$ is one. We investigate the specific momentum where the energy of one quasi-particle is lowered the most due to the perturbation, i.e. at the minimum of the six energy bands. We find that the minima of the dispersion lie at $\boldsymbol{k}_{\min} = \pm\left(\frac{2\pi}{3}, -\frac{2\pi}{3}\right)$ for small enough values of λ. In order to investigate the band gap Δ of one quasi-particle, we look at the dispersion at these minima, i.e. at the lowest band at $\boldsymbol{k}_{\min}$. It is possible to explicitly diagonalize the matrix H_k at the minima, which gives us an analytic expression for the energy gap as a function of λ. In specific, Δ is obtained as a series expansion in λ.

From the gap momentum we conclude the periodicity of the favored ordering pattern of the system. For the unperturbed case $\lambda = 0$, the system is in a trivial x-polarized phase where the spins are aligned by the magnetic field σ^x. All spins point in the same direction, giving rise to the terminology 'polarized'. Switching on the perturbation $\sigma_i^z \sigma_j^z$ ($\lambda > 0$) introduces fluctuations about this polarized state. The structure of the fluctuations over the lattice is determined by the momentum of the one quasi-particle gap $\boldsymbol{k}_{\min}$. This can be understood by considering the complex phase $\mathrm{e}^{i\boldsymbol{k}\boldsymbol{r}}$ of a one quasi-particle state at $\boldsymbol{r}$ for the eigenstate which corresponds to the one quasi-particle gap momentum $\boldsymbol{k}_{\min}$. The resulting ordering pattern is a clock-ordered $\sqrt{3} \times \sqrt{3}$ structure. We will elaborate on this in subsection 5.1.3. In the vicinity of a continuous phase transition at a critical value λ_c, the elementary excitation gap of a quasi-particle in the system in the thermodynamic limit is given by a power-law behavior $\Delta \propto |\lambda - \lambda_c|^{z\nu}$. For the case considered in this chapter, $z = 1$. At the point of the transition, the elementary excitation gap vanishes. We thus look at the potential vanishing of the excitation gap Δ in order to find a critical value λ_c indicating a continuous phase transition.

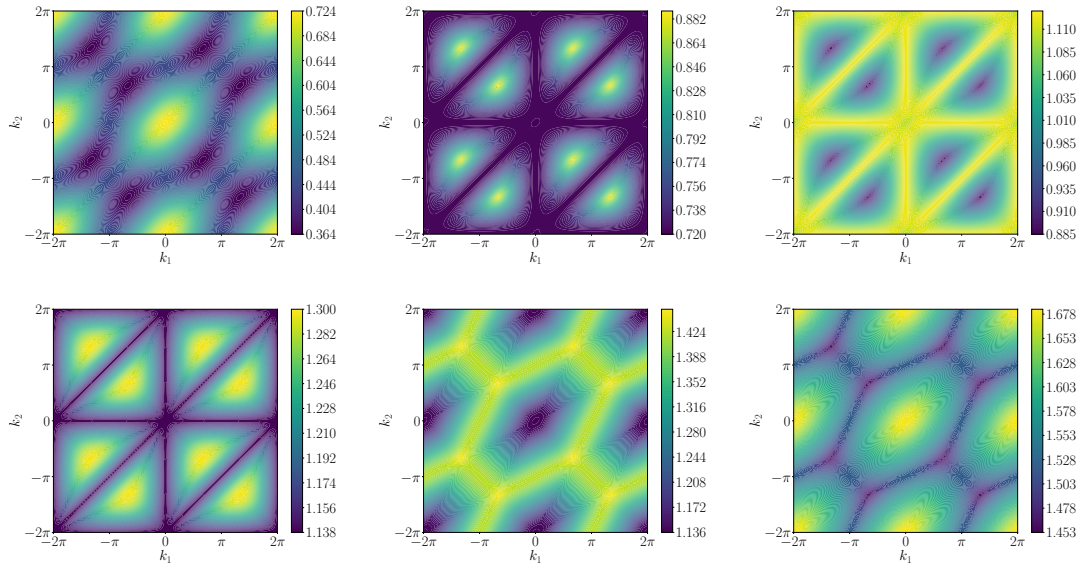

Figure 5.2.: One quasi-particle dispersion in the J_1-J_2 TFIM for $J_{1,2}/2h = 0.2$. The six energy bands obtained from diagonalizing the respective Hamiltonian in momentum space are shown sorted by energy. The momenta k_1, k_2 are defined with respect to the translational lattice vectors $\boldsymbol{a}_1, \boldsymbol{a}_2$. The minima of the dispersion lie at $\boldsymbol{k}_{\min} = \pm\left(\frac{2\pi}{3}, -\frac{2\pi}{3}\right)$.

We use the extrapolation techniques introduced in section 3.4 for the series expansion for the gap in order to get a better estimate of the gap for larger λ and a better representation of a potential power-law behavior. The results of the extrapolations of the gap are shown in Figure 5.3. We show only extrapolants $(d)P[L, M]$ obtained from orders $k = 9$ or higher of the bare series and with $d = L - M \leq 3$. Defective extrapolants are excluded. Additionally, the figure shows the bare series in the maximal order ($k_{\max} = 11$) in the perturbation.
In order to judge the convergence of the bare series, we plot lower orders ($k = 6$ to 10) alongside the series in the highest obtained order in lighter colors, with the opacity increasing with order. As can be seen, for lower values of λ all orders lie on top of each other. The orders start to spread more with increasing perturbation parameter λ as the range in which the perturbation series is converged in the obtained order is exceeded. The extrapolations visibly increase the range where the description of the gap is well converged. All shown non-defective Padé and DlogPadé extrapolants lie close to each other and the bare series. This indicates that the extrapolations work well and describe the behavior of the calculated series for the gap well. The high-order extrapolants show a clear closing tendency around $\lambda \approx 0.3$, indicating a continuous quantum phase transition. Before analyzing this gap closing in more detail, we first investigate the opposite limit, the low-field limit.

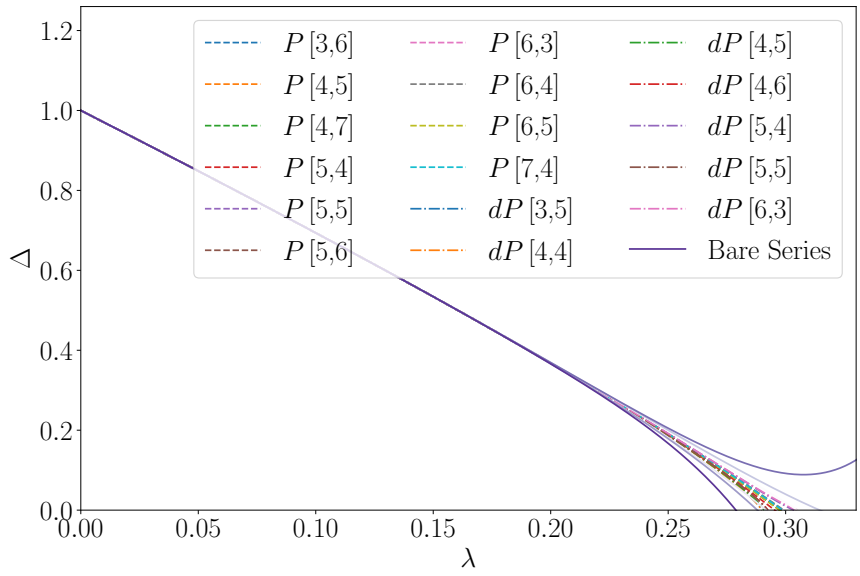

Figure 5.3.: One quasi-particle excitation gap Δ in the J_1-J_2 TFIM. The bare series in the maximal order $k_{\max} = 11$ is shown along lower orders ($k = 6$ to 10) in lower opacities and the obtained Padé and DlogPadé extrapolants $(d)P[L, M]$ as a function of $\lambda = J/2h$. Note that H^{TFIM} is defined such that Δ is calculated in units of $2h$. Only non-defective extrapolants in orders $k \geq 9$ with $L - M \leq 3$ are shown.

5.1.2. Low-field limit for $J_1 = J_2$

In the following section, we analyze the low-field limit ($h \gg J$) of the J_1-J_2 TFIM. Let us start by discussing the classical limit $h = 0$ for $J_1 = J_2 =: J$. In this case, the Hamiltonian is given by

$$H = \sum_{\substack{\langle i,j \rangle \\ \langle\langle i,j \rangle\rangle}} J\, \sigma_i^z \sigma_j^z \,,$$

where the sum runs over all pairs of nearest and next-nearest neighbors i and j. In our case of antiferromagnetic Ising coupling $J > 0$, coupled spins prefer to align antiparallel. Note that the sites interact only via the bonds shown in Figure 5.1, where the interaction has the same strength J on all bonds. Still, we will keep referring to the two 'types' of bonds as J_1 and J_2 in the following in order to distinguish their different geometry. There is no state in which the condition of antiparallel alignment is fulfilled on all bonds due to the geometrically frustrated lattice. In particular, within the small triangles comprised of J_1 bonds, at least one of the three bonds is ferromagnetic. The classical ground states of the system are given by spin configurations which minimize the total number of ferromagnetic bonds on the lattice. It is clear to see that any ground-state configuration has to fulfill the following two requirements:

1. in each triangle one J_1 bond is ferromagnetic and two J_1 bonds are antiferromagnetic and
2. no J_2 bond is ferromagnetic.

We will now argue why the number of configurations that satisfy these requirements is infinitely large in the thermodynamic limit. For this it is illustrative to regard the lattice as circular plaquettes arranged on a triangular lattice, as sketched in Figure 5.4.

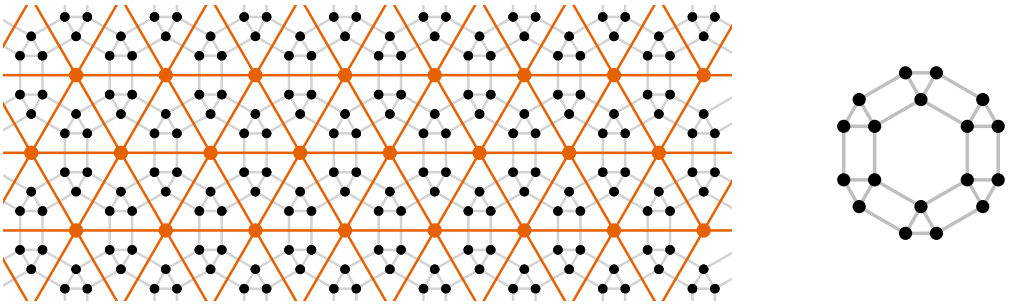

Figure 5.4.: Visualization of the structuring of the J_1-J_2 lattice into circular plaquettes. The J_1-J_2 lattice can be seen as an arrangement of circular plaquettes on a triangular lattice, shown in orange. One circular plaquette is shown on the right hand side. In order to understand the configurations of spins comprising the ground-state manifold in the limit $h = 0$ of the TFIM, it is illustrative to first investigate which configurations form a ground state on such finite circular plaquettes.

One circular plaquette contains six J_1-triangles and hence six ferromagnetic bonds in a ground state. We want to find all spin configurations where the only ferromagnetic bonds are those six. We proceed systematically as follows. Take one spin in the circular plaquette and choose its eigenvalue to be either $\sigma^z = +1$ or $\sigma^z = -1$, and fix that eigenvalue. Going from there along the circle, identify all spin eigenvalues which are fixed by this one spin by obeying the two rules for a ground-state configuration and fix those accordingly. If this leaves a spin with undetermined eigenvalue, again choose its eigenvalue. Repeat this procedure until all spin eigenvalues are set. In the end, check whether the resulting configuration fulfills the two ground-state rules, i.e. whether the bond 'closing' the circle is valid for a ground state. This results in five possible types of configurations, shown in Figure 5.5.

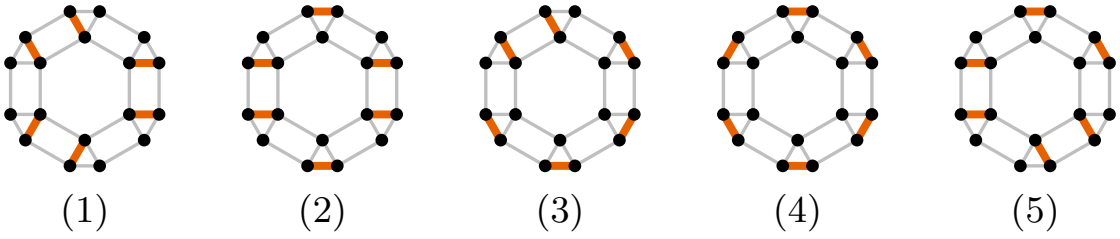

Figure 5.5.: Possible types of ground-state configurations on a circular plaquette for $h = 0$. Each J_1-triangle must have exactly one ferromagnetic bond (orange), and all other bonds are antiferromagnetic (light gray). Such a distribution of six ferromagnetic J_1 bonds over the plaquette results in five types of configurations. Note that the distribution of those ferromagnetic bonds has to be compatible with an explicit spin configuration. Further ground-state configurations of those five types are obtained by performing the symmetry operations listed in the main text.

Note that the representation of configurations in terms of ferro- and antiferromagnetic bonds does not specify whether the ferromagnetic bond is between two spins with eigenvalues $\sigma^z = +1$ or $\sigma^z = -1$. Thus, each type of those configurations can be realized by two spin configurations which are related to each other by a global spin flip. It is clear that the plaquettes remain ground states upon rotations and mirroring. The following operations on the five types of ground-state plaquettes yield further ground states of the same type:

- Type 1: vertical mirroring (2),
- Type 2: rotation by 120° (3),
- Type 3: rotation by 60° (6),
- Type 4: none (1),
- Type 5: rotation by 60° (6).

The number in brackets states the total number of configurations of the type obtained by the operation (without the global spin flip, which yields an additional factor 2). We thus find $2 \cdot 18$ distinct ground-state spin configurations on one circular plaquette for $h = 0$.

In a ground-state configuration on the infinite lattice, each circular plaquette is in one of those five types of configurations. Even though the plaquettes are not independent from each other, as they share multiple sites and bonds, we find an infinite number of possibilities to combine the ground-state plaquettes into a ground state on the full lattice. This can be understood looking at the illustration in Figure 5.6. Assume that we fix the configuration of one plaquette on the lattice (in the illustrated example to type 5). This puts some constraints on the six plaquettes surrounding the fixed plaquette in a circle, but does not determine their type uniquely. Within the circle surrounding those six plaquettes, we find six plaquettes whose configuration can be chosen from at least two different plaquette types. Thus, even though one plaquette is fixed, the second-to-next surrounding circle again allows for multiple choices, along with some choices in the directly surrounding circle. This pattern extends over the full lattice. In consequence, the ground state is extensively degenerate for $h = 0$.

Now consider applying a perturbation in terms of a small transverse magnetic field $h \ll J$, which introduces quantum fluctuations by flipping the σ^z component of the spins. In general, flipping a spin by applying the operator σ^x turns all ferromagnetic bonds of that spin into antiferromagnetic bonds, and vice versa. Hence, flipping one spin within a ground-state configuration results in a configuration with more ferromagnetic bonds than before which is thus no longer a classical ground state. However, there might exist a sequence of spin-flip operations resulting in a different configuration which is still a valid ground state. In such a scenario, the corresponding classical ground state would be energetically favored by the perturbation of the small transverse magnetic field. The ground-state manifold in the low-field model, which can in general be comprised of any possible superpositions of classical ground states, would then be dominated by those classical ground states which gain the most energy from quantum fluctuations induced by the magnetic field. This approach of identifying basis states for possible quantum ground states by searching for the softest fluctuations allowing for the maximal energy gain from the perturbation was introduced by Moessner and Sondhi in Ref. [70].
Again, we start our search for such fluctuations between different ground states by restricting ourselves to the finite circular plaquettes. Looking at the five types of ground-state configurations in Figure 5.5, we find that applying a spin flip to the six spins along the inner hexagon of a circular

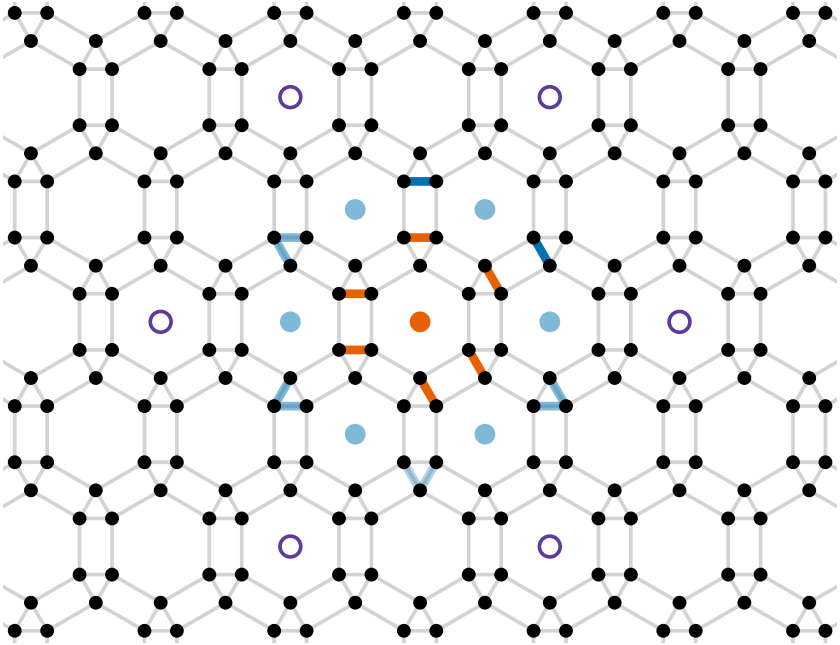

Figure 5.6.: Illustration of the extensive ground-state degeneracy in the limit $h = 0$. Assume the configuration of a central plaquette (orange dot ●) is chosen to be type 5. The ferromagnetic bonds of this plaquette are drawn in orange. Antiferromagnetic bonds are drawn in light gray. This places constraints on the six plaquettes surrounding the central one in a circle (blue dots ●). Dark blue bonds resemble ferromagnetic bonds enforced by the central plaquette, while light blue bonds resemble the freedom of choosing one of the two respective bonds to be ferromagnetic. In the second-to-next circle, we find six plaquettes for which no ferromagnetic bond is fixed by the central plaquette (purple circles ○). The configuration of those plaquettes can be chosen from at least two types of configurations. This pattern can be extended over the full lattice, giving rise to an extensive degeneracy of the classical ground state.

plaquette of type 1 is equivalent to a rotation of the plaquette by 60°. The operation thus yields another ground state, which we term type 1′. The resonance between those two ground states, which arises in order 6 in h by this spin-flip sequence $\sigma_1^x\sigma_2^x\sigma_3^x\sigma_4^x\sigma_5^x\sigma_6^x$, is visualized in Figure 5.7 for a specific spin configuration. We do not find another resonating process in order 6 (or lower) among the other ground states on a plaquette. Hence, we conclude that out of the ground states on the plaquette, states of type 1 are favored energetically by the small perturbation. We note that also diagonal corrections to the ground-state energy due to the magnetic field occur. In general, those can favor either the same or another type of plaquette as the off-diagonal corrections which are discussed here. We did not consider these diagonal corrections explicitly for the J_1-J_2 TFIM. For an exemplary discussion of diagonal corrections, refer to subsection 5.2.2. While we assume that above a certain magnetic field strength the off-diagonal corrections dominate and type 1 plaquettes are selected, which is supported by our further results, other configurations might be favored for lower magnetic fields. The detailed discussion of this regime requires further analysis and remains an open point within this thesis.

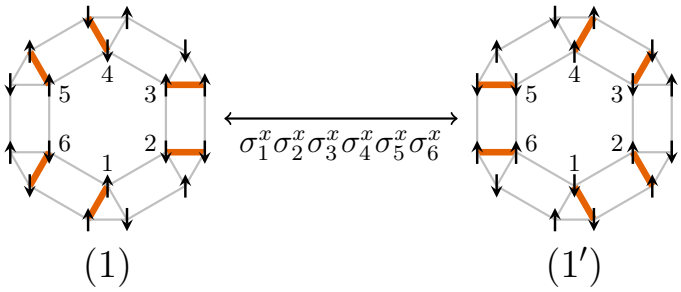

Figure 5.7.: Illustration of the resonating process between ground-state configurations of type 1 and 1′ on a circular plaquette in h^6. Applying the spin flip sequence $\sigma_1^x\sigma_2^x\sigma_3^x\sigma_4^x\sigma_5^x\sigma_6^x$ to the six spins along the inner hexagon changes the position of the ferromagnetic J_1 bond at each of those spins as shown. The resulting configuration is again a classical ground state. Applying the same spin flip sequence for a second time again results in the initial ground state. Note that the spin flip sequence corresponds to a clockwise rotation of the plaquette by 60°.

Returning to the infinite lattice, we need to consider the effect this spin-flip sequence has on the configurations of neighboring circular plaquettes. As neighboring plaquettes share multiple sites and bonds, spin-flip operations on one plaquette also change the distribution of ferromagnetic bonds on the neighboring plaquettes and we have to verify that the investigated operator sequence also results in a valid ground state on the full lattice. We find that for a second plaquette in any of the types of ground-state configurations shown in Figure 5.5 neighboring our resonating plaquette, the second plaquette remains in a ground-state configuration. For the illustration of an example for this, see Figure 5.8. Hence, applying the spin-flip sequence to any type-1 plaquette within a classical ground state on the infinite lattice results in a resonance with another classical ground state. This implies that ground-state configurations with the maximal density of plaquettes in configuration of type 1 are energetically favored by the perturbation.

This scenario we find is in close analogy the the antiferromagnetic TFIM with nearest-neighbor interactions (NNTFIM) on the triangular lattice [70]. Before we discuss the favored ground-state configurations in the J_1-J_2 TFIM in more detail, we give a short overview concerning the low-field limit in this triangular lattice NNTFIM, as we will later draw conclusions from their analogy found in the course of this. Without transverse field, the ground states are given by configurations where each triangle has exactly one ferromagnetic and two antiferromagnetic bonds, resulting in an extensively degenerate ground-state manifold. Those ground states can be represented in a dimer model on the dual lattice of the triangular lattice, which is the honeycomb lattice, by placing dimers on all ferromagnetic bonds. In the dimer model, the classical ground-state manifold is represented by all possible hardcore dimer-coverings up to a global spin flip [70]. Now, we introduce an infinitesimal transverse magnetic field which induces quantum fluctuations and analyze its effects on the classical ground states. Flipping a spin within a ground state does not leave the ground-state space if the number of ferromagnetic bonds remains unchanged. In the dimer-picture, flipping a spin corresponds to changing all six surrounding dimers to non-dimers, and vice versa. As a dimer corresponds to a ferromagnetic bond, the state remains a ground state if the number of dimers remains unchanged and the condition of a hardcore dimer-covering remains fulfilled. As each spin is surrounded by a hexagonal plaquette, this is the case for plaquettes with three dimers. Consequently, such plaquettes are called ‘flippable’. The quan-

tum ground-state manifold is in general composed of superpositions of classical ground states. In first order in the magnetic field, those superpositions generated from quantum fluctuations above a classical ground state with the maximal number of flippable plaquettes have the lowest energy. The respective ground states exhibit symmetry-breaking clock-order. As the classically disordered system transitions into a quantum *ordered* state driven by quantum fluctuations (*disorder*), this scenario is called *order by disorder* [70], based on the investigation of thermal order by disorder in generalized two-dimensional frustrated Ising models by Villain et al. in 1980 [71].

Coming back to the J_1-J_2 TFIM investigated in this thesis, we can write down an effective model in the low-field limit in analogy to the discussed quantum dimer model in terms of the resonances between plaquettes of type 1 and $1'$ within the ground-state manifold as

$$H = h^6 \sum_p \left(|1\rangle_p \langle 1'|_p + \text{h.c.} \right) ,$$

where the sum runs over all circular plaquettes p on the lattice. As already argued before, this effective model contains that spin-flip sequences in h^6 can switch between ground-state configuration 1 and $1'$ on a circular plaquette within a classical ground state. The corresponding ground states with maximal density of plaquettes with configuration of type 1 thus form a basis for a variational analysis [70].
We will now analyze the structure of those configurations. As shown in Figure 5.4, the plaquettes reside on a triangular lattice. Obeying the rules for a classical ground-state configuration, we can place a maximum of two plaquettes of type 1 (and $1'$) on one triangle. The third plaquette is then fixed to type 4. This results in 2/3 of all plaquettes being type 1 and 1/3 being type 4. The left panel in Figure 5.8 shows the resulting configuration of ferromagnetic bonds and visualizes the periodicity of the configuration. The right panel of the figure illustrates the effect the resonance from type 1 to type $1'$ has on this configuration. Note that while the plaquettes are not elementary unit cells of the lattice, the periodicity in terms of the actual six site elementary unit cells is the same, as can easily be verified by looking at Figure 5.8. Hereby we have found the configurations out of the infinitely degenerate classical ground-state manifold which are energetically favored by a small perturbation h. The choice of one plaquette configuration determines the configuration on the entire lattice, lifting the infinite degeneracy of the classical ground-state manifold. We observe that in those configurations selected by the perturbation, the elementary unit cells are in three different states, arranged in a $\sqrt{3} \times \sqrt{3}$ structure on the triangular lattice.

With this, the analogy to the order-by-disorder scenario in the NNTFIM on the triangular lattice becomes even more apparent. In both models, we find the infinite degeneracy of the classical ground-state manifold to be lifted by quantum fluctuations induced by a small transverse magnetic field, which select configurations with symmetry breaking clock-order in an order-by-disorder scenario. We note that the emerging clock-order has the same ordering structure as the favored ordering defined by the gap momentum in the high-field limit, $\boldsymbol{k}_{\min} = \pm(\frac{2\pi}{3}, -\frac{2\pi}{3})$. Thus, the ordering structure in the low-field limit is the one preferred by the fluctuations about the high-field limit.

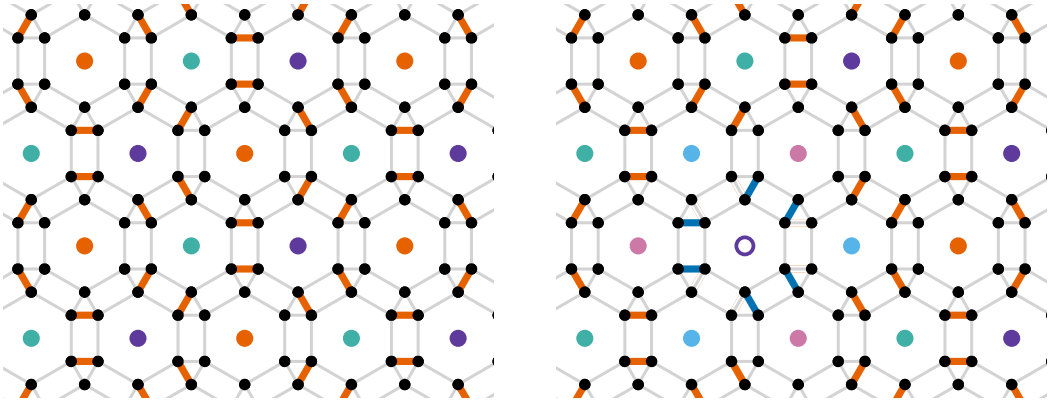

Figure 5.8.: Left panel: Classical ground-state configuration with maximal density of circular plaquettes of type 1, selected by the magnetic field perturbation due to resonances between ground states in order 6. The figure shows the distribution of ferromagnetic (orange) and antiferromagnetic (light gray) bonds over the lattice in this configuration. The colored dots in the centers of the plaquettes show the type of the plaquette configuration, with the following color code: ● marks a plaquette of type 1, ● marks a plaquette of type 1′ (type 1 rotated by 60°) and ● marks a plaquette of type 4. Right panel: Configuration resulting from the resonance between a plaquette of type 1 (i.e. ●) and 1′ (i.e. ●) in the configuration in the left panel. The resonating plaquette is marked with a purple circle ○ . Upon this, the ferromagnetic bonds on the resonating plaquette are changed into the configuration highlighted in blue. The type of the six surrounding plaquettes is changed accordingly, where ● marks a plaquette of type 3 and ● marks a plaquette of type 5 (including rotated versions). However, it is clear that the resulting configuration is again a classical ground state.

5.1.3. Analysis of the criticality of the quantum phase transition for $J_1 = J_2$

In the following we analyze the criticality of the quantum phase transition out of the high-field limit discussed in subsection 5.1.1. Let us first recapitulate our findings from the previous two subsections.

As discussed in subsection 5.1.2, for low fields ($h \ll J$) a quantum ordered state with $\sqrt{3} \times \sqrt{3}$ clock-ordered structure is selected from an extensively degenerate classical ground-state space by quantum fluctuations in an order-by-disorder scenario. For high fields ($h \gg J$), the system is in a polarized phase where all spins are aligned by the high magnetic field. The momentum of the one quasi-particle excitation gap corresponds to a clock-order. Series expansions of the gap about this high-field limit performed in subsection 5.1.1 indicate a phase transition at a critical point λ_c separating the high- and low-field phase.

We find an analogy between the order-by-disorder scenario in the J_1-J_2 TFIM and the NNTFIM on the triangular lattice, as described in detail in subsection 5.1.2. On the triangular lattice, the frustrated lattice geometry results in an extensive ground-state degeneracy for $h = 0$. Likewise, quantum fluctuations for $0 < h < \epsilon$ lift the ground-state degeneracy and select a clock-ordered state [70].

In Ref. [72], the high-field limit ($h \gg J$) of the TFIM on the triangular lattice is investigated.

They apply the same perturbative series expansion techniques as we do in this thesis to obtain the one quasi-particle dispersion as a series in order $k_{\max} = 11$. They find the minima of the one quasi-particle dispersion at $\boldsymbol{k}_{\min} = \pm\left(\frac{2\pi}{3}, -\frac{2\pi}{3}\right)$. A plot of the complex phase of eigenstates given by these momenta reveals a $\sqrt{3} \times \sqrt{3}$ structure. From extrapolations of the one quasi-particle gap, they extract a critical point around $\lambda_c \approx 0.305$ with critical exponent $\nu = 0.708 \pm 0.012$, which is also supported by quantum Monte Carlo simulations [73]. They conclude that the gap closes in a second-order phase transition between an x-polarized phase ($\lambda < \lambda_c$) and an ordered phase ($\lambda > \lambda_c$) with $\sqrt{3} \times \sqrt{3}$ structure. The application of a Landau-Ginzburg-Wilson analysis (see Ref. [74]) to the effective quantum dimer model on the dual lattice implies that the quantum phase transition lies within the 3d XY universality class [51, 70], with $\nu_{\text{3d XY}} = 0.679(7)$ [75].

Motivated by the analogous effective low-field description of the J_1-J_2 TFIM on the link-Kagome lattice, we postulate 3d XY criticality for the continuous phase transition between the ordered phase for low fields and the polarized phase for high fields. We probe this theory by looking at the criticality of the phase transition found in subsection 5.1.1, for which we analyze the DlogPadé extrapolants in more detail. We extract the critical point λ_c and the exponent $z\nu$ of the gap closing using Equation (3.23). Here, we have the dynamical critical exponent $z = 1$. In order to analyze the convergence behavior of those critical values, we structure the DlogPadé extrapolants $dP[L, M]$ into families with the same $d = L - M$. We then plot the calculated λ_c and ν as a function of the order $r = L + M + 1$ of the series expansion, connecting points within the same family. Figure 5.9 shows the convergence behavior of critical point and exponent, taking only extrapolants with $|d| \leq 3$ into consideration.

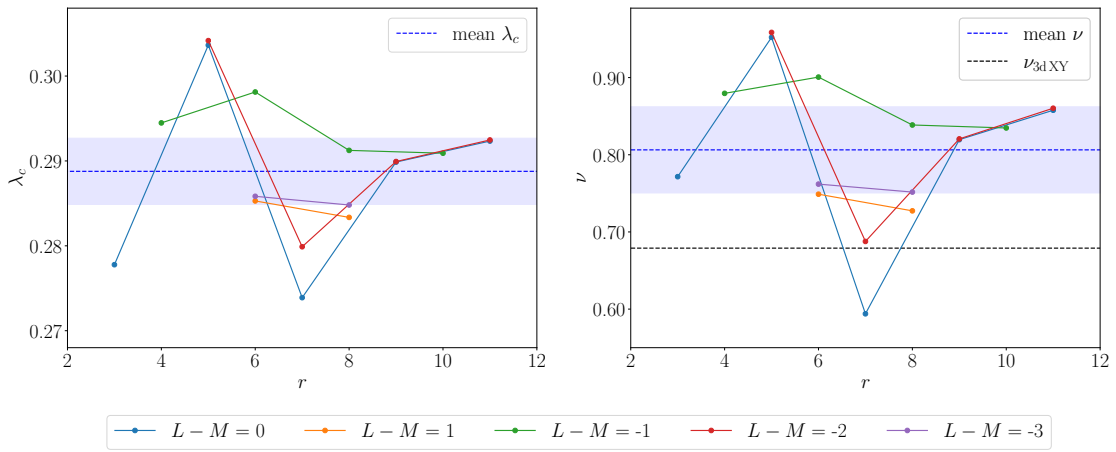

Figure 5.9.: Convergence behavior of the critical point λ_c (left panel) and critical exponent ν (right panel) extracted from the DlogPadé extrapolants $dP[L, M]$ in the considered order $r = L + M + 1$. The extrapolants are structured into families by connecting extrapolants with the same $d = L - M$. We show only extrapolants with $|d| \leq 3$. To obtain a mean value for λ_c and ν we average over the extrapolants of highest order for each shown family. The calculated means $\lambda_c = 0.289 \pm 0.004$ and $\nu = 0.806 \pm 0.056$ are drawn as dashed blue lines, with the highlighted areas indicating the standard deviations of the individual extrapolants. The black dashed line represents the literature value $\nu_{\text{3d XY}} = 0.679(7)$ [75].

For higher orders the spread of the extrapolants decreases. For calculating mean values for λ_c

and ν, we average over the extrapolants of the highest order of all considered families. We obtain the critical value for the phase transition

$$\lambda_c = 0.289 \pm 0.004\,.$$

The gap closes with a critical exponent of

$$\nu = 0.806 \pm 0.056\,.$$

The value we obtain is approximately 20% larger than the critical exponent of the proposed 3d XY criticality class, $\nu_{3\mathrm{d\,XY}} = 0.679(7)$ [75].
We know that DlogPadé extrapolations tend to overestimate the critical value λ_c, resulting in a systematic overestimation of the critical exponent ν. Such an overestimation is also experienced by Powalski et al. in the investigation of the NNTFIM on the triangular lattice [72]. By biasing the DlogPadé extrapolations [68] to have a pole at the critical point given by quantum Monte Carlo simulations, they obtain a critical exponent closer to the expected $\nu_{3\mathrm{d\,XY}}$. We do not know another estimate for the critical point of the J_1-J_2 TFIM. Still, in order to get a feeling for the effect of the overestimation of λ_c, we try to perform biased DlogPadé extrapolations with steadily decreasing λ_c and extract the obtained averaged critical exponent. In order to get a critical exponent $\nu \approx 0.68$, the critical point has to be biased to $\lambda_c \approx 0.275$. This value lies considerably below the critical point obtained from the unbiased DlogPadé extrapolations.
Without further analysis, we can not confirm our postulated scenario rigorously. Nevertheless, we can try to give an explanation why the obtained order of the series expansion does not suffice in capturing the full criticality of the proposed 3d XY phase transition. The applied DlogPadé extrapolation scheme relies on the criticality being described by a power-law behavior, $\Delta \propto |\lambda - \lambda_c|^{z\nu}$. Such a behavior is realized on an infinite lattice close to λ_c. However, in finite perturbation order, additive corrections to the power-law scaling occur. Being less dominated by a power-law behavior decreases the ability of the extrapolations to accurately describe the gap closing. Looking at the $\sqrt{3} \times \sqrt{3}$ ordering structure of the fluctuations in the high-field limit, we observe that its unit cell spans several elementary unit cells, each containing six sites. It is thus apparent that high-order linked processes are needed in order to even capture the structure of the fluctuations. In order $k_{\max} = 11$ of the series expansion, a hopping process can cover maximally 4 elementary unit cells in $\boldsymbol{a}_1$ ($\boldsymbol{a}_2$) direction, which can be seen by investigating the available bonds in Figure 5.1. This limits the spatial extent of correlations between spins. One can argue that while unit cells of the ordering structure are connected in the considered order, $k_{\max} = 11$ might still be too low to take a sufficient extent of fluctuations on the lattice into account.
Combining this reasoning with the analogy we draw to the NNTFIM on the triangular lattice, we come to the conclusion that the critical exponent we obtain is in accordance with the proposed 3d XY criticality. In particular, we note that we can rule out 3d Ising criticality with $\nu_{3\mathrm{d\,Ising}} = 0.629971(4)$ [76] with the obtained results (see also the next section 5.2).

5.1.4. Phase transition for arbitrary J_2/J_1

After having discussed the J_1-J_2 TFIM for equal interaction strengths $J_1 = J_2$ in detail, we examine the case of arbitrary ratios of J_2/J_1.
We begin by noticing that the discussion of the order-by-disorder scenario for the low-field limit in subsection 5.1.2 holds for arbitrary $J_1, J_2 > 0$. This is easily seen by observing that in all classical ground states, each J_1-triangle has exactly one ferromagnetic bond if $J_1 > 0$. Further, there is no ferromagnetic J_2 bond in the classical ground states. The configuration of the ground

states follows purely from the *existence* of J_2 bonds connecting the triangles: as long as $J_2 > 0$, having a ferromagnetic J_2 bond is energetically unfavorable. From this it can be inferred that the low-field physics do not depend on the actual ratio of J_2/J_1. In the high-field limit, the gap momentum is given by $\boldsymbol{k}_{\min} = \pm(\frac{2\pi}{3}, -\frac{2\pi}{3})$ independent of the ratio of J_2/J_1. We thus conjecture that we find a phase transition within the 3d XY criticality class for arbitrary ratios of J_2/J_1.

After performing DlogPadé extrapolations of the gap, we extract the critical point λ_c and the critical exponent ν for various ratios of J_2/J_1 parameterized by θ as follows:

$$J_1 = \cos(\theta)\, J\,,$$
$$J_2 = \sin(\theta)\, J\,.$$

The symmetric case $J_1 = J_2$, which has been discussed in detail in the previous subsections, is recovered for $\theta = \pi/4$. Note however, that in this parametrization we have $J_1 = J_2 = J/\sqrt{2}$, resulting in a rescaling of the critical point $\lambda_{c,J_1=J_2}$ compared to previous discussions where we set $J_1 = J_2 = J$. The ratio $J_2/J_1 = 1/27$, which corresponds to the ratio given by the algebraic van-der-Waals decay with $\alpha = 6$, is realized for $\theta \approx 0.037$. Note that the series expansion for arbitrary ratios is only calculated up to order $k_{\max} = 10$ due to the increased complexity of the problem. For $J_1 = J_2$, all bonds are equivalent and one single perturbation parameter λ is needed in the implementation. For arbitrary $J_{1,2}$, two perturbation parameters $\lambda^{(1,2)}$ are needed, which increases the number of relevant graphs (see also section 3.2). Figure 5.10 shows the critical point and exponent extracted from selected DlogPadé extrapolants. For reference, the values $\lambda_{c,J_1=J_2}$ and $\nu_{J_1=J_2}$ calculated for the symmetric case $J_1 = J_2$ in subsection 5.1.3 are plotted as blue lines.

Regarding the critical points, although all extrapolants show the same qualitative behaviors, deviations of some extrapolants of lower orders (e.g. $dP[3,2]$, $dP[2,3]$, plotted in lower opacities in Figure 5.10) can be observed. In general, we find that with increasing deviation from the symmetric case, those lower order extrapolants tend do describe the gap less well and they are discarded for the discussion. Coming from $J_1 = J_2$, a decrease in J_2 results in the gap closing at increasing λ. For $J_2/J_1 \lesssim 0.2$ ($\theta \lesssim 0.2$) no clear gap closing tendencies are present. This can be understood by looking at the limiting case $J_2 = 0$ ($\theta = 0$). Here, the lattice is given by decoupled J_1-triangles on which no phase transition is possible. When this limit is approached, we observe that the critical point gets pushed to larger λ.

The range within which our series expansion of the gap in the obtained perturbation order and the extrapolations are reasonably converged however is finite, and we can not track phase transitions at too large λ. We expect a phase transition as long as $J_2 > 0$, with the gap closing at values beyond the range where the obtained extrapolants are converged for $\theta \lesssim 0.2$. Coming from $J_1 = J_2$, λ_c stays approximately constant for a decrease in J_1.

For the critical exponents, a large variety in the qualitative behavior is observed. Nevertheless, we can identify a consistent tendency regarding extrapolants of high orders, for which we already observed a better convergence behavior regarding the critical points. For $\theta < \pi/4$, the critical exponent decreases slightly with θ. For $\theta > \pi/4$, the exponent increases slightly with θ. Within the range of deviations, one could argue a roughly constant value around the calculated $\nu_{J_1=J_2}$ from subsection 5.1.3 (blue line and shaded region) and conclude that the phase transition lies within the same proposed 3d XY criticality class as expected.

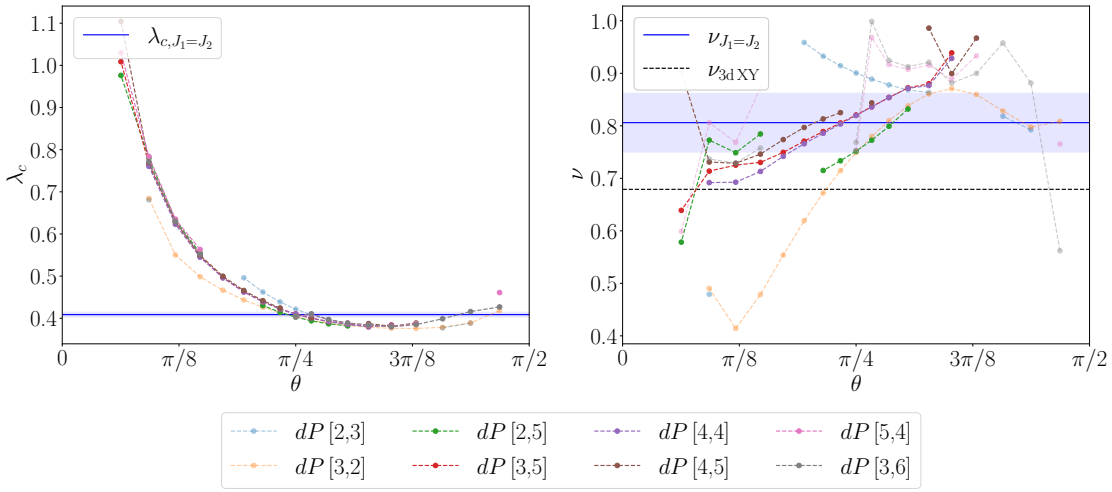

Figure 5.10.: Critical points λ_c (left panel) and critical exponents ν (right panel) for various ratios of J_2/J_1 parameterized by θ as given in the main text. The plots show the results obtained from individual selected DlogPadé extrapolants in different orders. Extrapolants which show deviations from the (qualitative) behavior of the bulk of extrapolants are shown in lighter opacities. The blue lines and shaded regions show the values $\lambda_{c,J_1=J_2}$ and $\nu_{J_1=J_2}$ with their standard deviations as calculated in subsection 5.1.3, respectively. Note that the value $\lambda_{c,J_1=J_2}$ is rescaled due to the modified definition of $J_{1,2}$. The black dashed line in the right panel shows the literature value for the assumed 3d XY criticality of the phase transition, $\nu_{3d\,XY} = 0.679(7)$ [75].

5.2. J_1-J_3 transverse-field Ising model

In this next section we continue our discussion of reduced versions of the TFIM by setting $J_2 = 0$, which results in the J_1-J_3 TFIM. The lattice geometry of the considered J_1 and J_3 bonds is shown in Figure 5.11. We proceed analogously to the analysis of the J_1-J_2 TFIM in section 5.1. We discuss the high-field limit in subsection 5.2.1 and the low-field limit in subsection 5.2.2 in the case $J_1 = J_3$. We analyze the phase transition we find between the two limits in this case in subsection 5.2.3. We then discuss the model for arbitrary ratios of J_3/J_1 in subsection 5.2.4.

5.2.1. High-field limit for $J_1 = J_3$

We first discuss the high-field limit $h \gg J$ of the J_1-J_3 TFIM. As we follow the same methodology as for the J_1-J_2 TFIM, please refer to the corresponding subsection 5.1.1 for more detailed descriptions. We again calculate the one quasi-particle dispersion in order $k_{\max} = 11$ for $J_1 = J_3 =: J$ and in order $k_{\max} = 10$ for arbitrary J_1, J_3 (see subsection 5.2.4). The six dispersive energy bands are shown in Figure 5.12 for $\lambda = 0.2$. In the J_1-J_3 TFIM, we find the one quasi-particle excitation gap located at $\boldsymbol{k}_{\min} = (0, 0)$. The same holds for arbitrary $J_1, J_3 > 0$. From this we conclude the ordering pattern of fluctuations introduced to the system by the perturbation.
The quasi-particle excitation gap given by the dispersion at the minimum is calculated as a series expansion in λ. The result is shown in Figure 5.13, alongside corresponding (Dlog)Padé extrapolants in orders $k \geq 8$ and $d \leq 3$. Defective extrapolants are excluded. Lower orders of

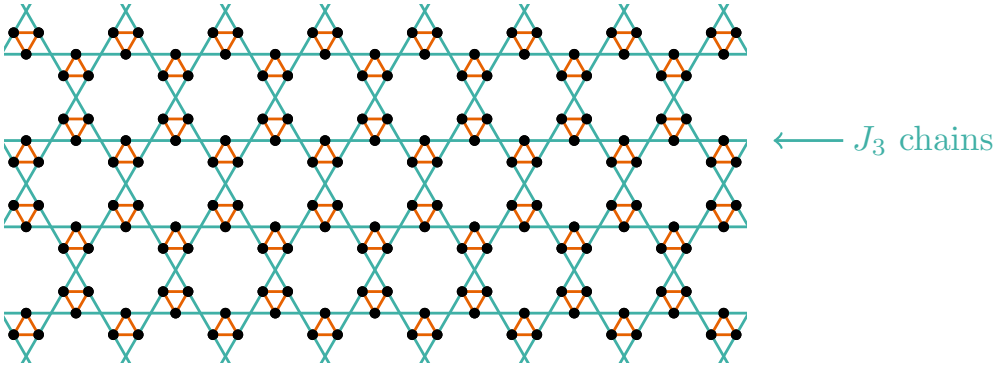

Figure 5.11.: Visualization of the J_1-J_3 lattice. The positions of the spin 1/2 are shown as black circles. The spins interact via bonds with strengths J_1 (orange) and J_3 (blue-green). Note that the J_3 bonds span parallel linear chains over the lattice, as indicated in the figure.

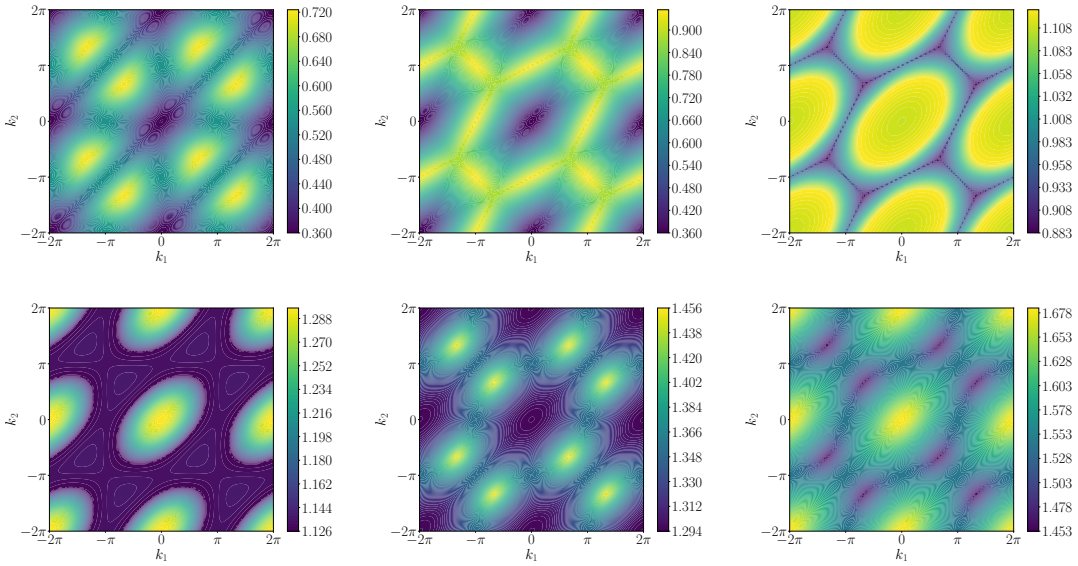

Figure 5.12.: One quasi-particle dispersion in the J_1-J_3 TFIM for $J_{1,3}/2h = 0.2$. The six energy bands obtained from diagonalizing the respective Hamiltonian in momentum space are shown sorted by energy. The momenta k_1, k_2 are defined with respect to the translational lattice vectors $\boldsymbol{a}_1, \boldsymbol{a}_2$. The minimum of the dispersion lies at $\boldsymbol{k}_{\min} = (0, 0)$.

the bare series ($k = 6$ to 10) are shown in decreasing opacity. We observe good convergence behavior of the bare series within the shown region. Also the high-order extrapolants are in good accordance and clearly indicate a closing of Δ in a narrow region around $\lambda \approx 0.3$. A slight separation between Padé and DlogPadé extrapolants appears around the gap closing, where the Padé extrapolants show a later closing of the gap by roughly 0.025. We assume that the DlogPadé extrapolants capture the behavior of Δ around $\lambda \approx 0.3$ better. However,

both extrapolation techniques still yield very similar results and agree in their indication of a quantum phase transition out of the high-field limit. In the next subsection, we will describe the low-field limit of the J_1-J_3 model. Afterwards, we will analyze the presumed quantum phase transition between those two limits.

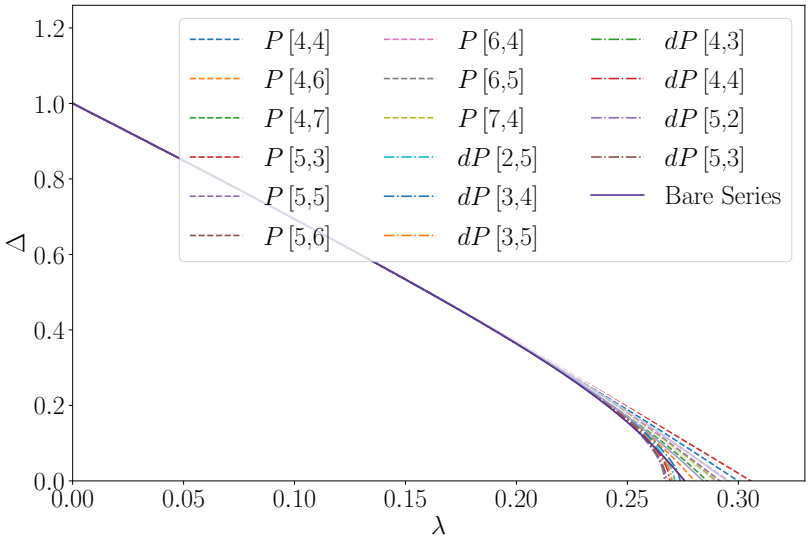

Figure 5.13.: One quasi-particle excitation gap Δ in the J_1-J_3 TFIM. The bare series in the maximal order $k_{\max} = 11$ is shown along lower orders ($k = 6$ to 10) in lower opacities and the obtained Padé and DlogPadé extrapolants $(d)P[L, M]$ as a function of $\lambda = J/2h$. Note that H^{TFIM} is defined such that Δ is calculated in units of $2h$. Only non-defective extrapolants in orders $k \geq 8$ with $L - M \leq 3$ are shown.

5.2.2. Low-field limit for $J_1 = J_3$

In this subsection we discuss the low-field limit ($h \ll J$) of the J_1-J_3 TFIM. For simplicity, we again discuss the case $J_1 = J_3$ where we do not have to consider a hierarchy of the bond colors. We follow the same logic as for the J_1-J_2 TFIM in subsection 5.1.2.

For $h = 0$, coupled spins prefer to align antiparallel on the frustrated J_1-J_3 lattice. Due to the frustration a finite number of bonds is ferromagnetic and classical ground states minimize the number of those ferromagnetic bonds. Within the J_1-triangles, exactly one of the three bonds is ferromagnetic. Further, no J_3 bond is ferromagnetic. In order to identify all possible ground-state configurations, we reiterate the procedure described in subsection 5.1.2 and first investigate possible ground-state configurations on circular plaquettes. Note that the decomposition of the lattice into plaquettes is analogous to Figure 5.4, with the J_2 bonds simply replaced by J_3 bonds. At first glance one might be tempted to assume that thus also all plaquette ground-state configurations of ferromagnetic bonds for the J_1-J_2 model shown in Figure 5.5 are also valid ground states for the J_1-J_3 model. This is however not the case, which becomes clear when taking the actual spin configuration yielding the distribution of ferromagnetic bonds into

account. In particular, we find that two of those bond-configurations do not exist in the J_1-J_3 model. Figure 5.14 shows the three possible types of classical ground-state configurations for this model in terms of the ferromagnetic bonds. As discussed in subsection 5.1.2, a ferromagnetic bond connects two spins with eigenvalues $\sigma^z = +1$ or $\sigma^z = -1$ and thus every bond configuration corresponds to two spin configurations related to each other by a global spin flip.

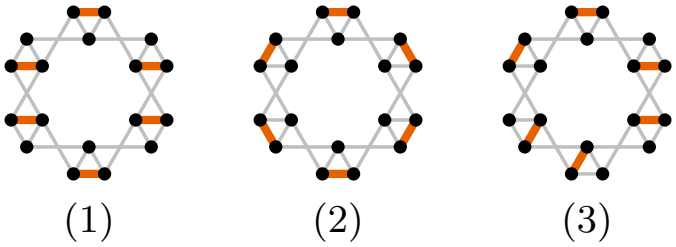

Figure 5.14.: Possible types of ground-state configurations on a circular plaquette for $h = 0$. Each J_1-triangle must have exactly one ferromagnetic bond, drawn in orange, and all other bonds are antiferromagnetic, drawn in light gray. Such a distribution of six ferromagnetic J_1 bonds over the plaquette results in three types of configurations. Note that the distribution of ferromagnetic bond has to be compatible with an explicit spin configuration.

On the infinite lattice we find an infinite number of possibilities to combine these plaquettes into a valid classical ground state. This is illustrated in Figure 5.15. We observe that infinite stripes can be build from one single plaquette configuration of type 1 and 3, respectively, as visualized in the figure. Next to a stripe of type 1, one can place either another stripe of type 1 or a stripe of type 3 with compatible 'orientation', and vice versa. Thus, there are infinitely many different combinations of such stripe alignments, giving rise to an extensive degeneracy of the classical ground state. Note that those stripe configurations are not the only classical ground states and we find a finite number of additional classical ground states.

Applying a small transverse magnetic field $h \ll J$ introduces individual spin flips to the classical ground states of $h = 0$. In contrast to the J_1-J_2 TFIM, we find no resonating process between different classical ground states in any finite order in h. This can be understood by looking at the geometry of the J_3 bonds in Figure 5.11. In the case $J_1 = 0$, the lattice is reduced to chains of J_3 bonds spanning the full lattice parallel to each other in three directions. Each spin is contained in exactly one of those chains. Along those chains, the spins are alternating as all J_3 bonds are antiferromagnetic in a classical ground state. Applying a single spin flip thus always results in the two J_3 bonds neighboring the spin turning ferromagnetic and the state is no longer a ground state. In order to recover a ground state, each spin in the chain would have to be flipped. For an infinite lattice, this is not possible in a finite-order process. From this we conclude that there are no off-diagonal matrix elements connecting different classical ground states in finite order.

However, we find that there are ground-state configurations which are energetically favored by diagonal corrections in h. We start by recognizing that each ground-state configuration can be build from three elementary unit cell configurations (in terms of ferromagnetic bonds), visualized in Figure 5.16. The three plaquettes in Figure 5.14 consist of different mixtures of those elementary unit cell configurations. We can thus identify which plaquette is favored energetically by considering the ground-state energy corrections due to the magnetic field on

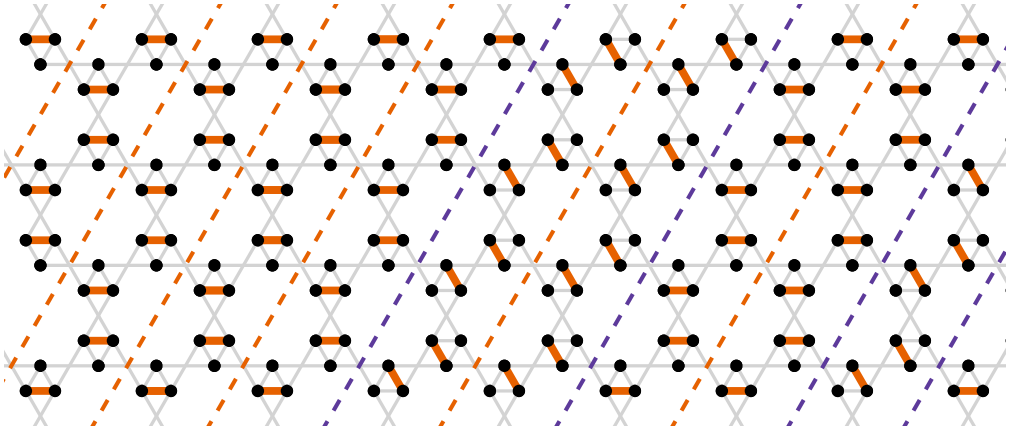

Figure 5.15.: Illustration of the ground-state degeneracy in the J_1-J_3 TFIM for $h = 0$. An exemplary classical ground-state configuration is shown, where orange lines represent ferromagnetic bonds and light gray lines represent antiferromagnetic bonds. The illustrated configuration consists of stripes of plaquettes of type 1 (orange dashed lines) and type 3 (purple dashed lines). Next to a type-1 stripe, one can always place either another type-1 stripe or a type-3 stripe, and vice versa. Note that the plaquettes are rotated differently in some stripes. One possible sequence of stripes is illustrated in the figure.

those unit cells. We calculate the first four orders analytically using Takahashi perturbation theory [77]. In zeroth order, each of the three unit cells has unperturbed energy $E_0^{(0)} = 2J_1$. In second order, the correction to the ground-state energy is given by

$$E_0^{(2)} = \lambda^2 \langle \Psi | PVSVP | \Psi \rangle \,. \tag{5.1}$$

Here, P is a projector onto the ground-state subspace, $S = (1-P)/(E_0^{(0)} - H_0)$, $V = h\sum_i \sigma_i^x$ is the perturbation and $|\Psi\rangle$ is the ground state. The energy correction contains a sum over all possible fluctuations due to the perturbation. The perturbation flips one spin, and thereby all connected ferromagnetic bonds become antiferromagnetic ones, and vice versa. In order to again yield the same ground state, the perturbation has to act on every spin twice. Thus only even perturbation orders contribute. To obtain the right correction, we also have to take the eight J_3 bonds 'leaving' the elementary unit cell into account, indicated by the dashed lines in Figure 5.16. In order two, only processes where the perturbation acts on exactly one spin contribute. The contribution of each spin depends on the number of ferro- and antiferromagnetic bonds connected to that spin. Each of the three elementary unit cell configurations has 4 spins with one ferromagnetic J_1 bond and 2 spins with only antiferromagnetic bonds. Thus, the second order correction is equal for all elementary unit cell configurations. Using Equation (5.1), we obtain

$$E_0^{(2)} = -\lambda^2 \left(4 \cdot \frac{1}{2J_3} + 2 \cdot \frac{1}{2J_1 + 2J_3} \right) .$$

In fourth order, the ground-state energy correction is given by

$$E_0^{(4)} = \lambda^4 \langle \Psi | \left(PVSVSVSVP - \frac{1}{2} PVS^2VPVSVP - \frac{1}{2} PVSVPVS^2VP \right) | \Psi \rangle \,. \tag{5.2}$$

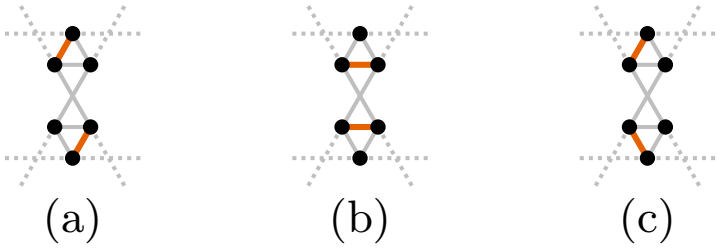

Figure 5.16.: Elementary unit cell configurations appearing in a classical ground-state configuration. Ferromagnetic bonds are drawn in orange, antiferromagnetic bonds are drawn in light gray. Antiferromagnetic J_3 bonds leaving the elementary unit cell are shown as dotted lines. When considering corrections to the ground-state energy of the unit cells, those bonds have to be taken into account in order to obtain correct results.

The last two summands arise due to two consecutive second-order processes, so they are equal for all three elementary unit cell configurations. The first summand describes a purely fourth order process acting on two spins connected by a bond. Spins can either be connected by a J_1 or a J_3 bond. The contribution of one process again depends on the other bonds those two spins are connected to. A J_1 bond can connect:

- two spins which both have one ferromagnetic J_1 bond (the J_1 bond is ferromagnetic itself), or
- two spins where one has one ferromagnetic J_1 bond and one has no ferromagnetic J_1 bond (the J_1 bond is antiferromagnetic),

and a J_3 bond can connect:

- two spins which both have no ferromagnetic J_1 bond, or
- two spins which both have one ferromagnetic J_1 bond, or
- two spins where one has one ferromagnetic J_1 bond and one has no ferromagnetic J_1 bond.

The three elementary unit cell configurations have the same composition of such J_1 bonds, resulting in equal contributions to the correction. However, they have different numbers of such J_3 bonds, giving rise to different fourth-order ground-state energy corrections. As the unit cells only differ in the J_3 bonds, it suffices to take exclusively processes acting on two spins connected by a J_3 bond into account when we want to compare the unit cell configurations energetically. Analytic calculation of Equation (5.2) yields the following corrections due to fourth-order processes on the J_3 bonds:

$$E^{(4)}_{J_3}(a) = -\lambda^4 \left(4 \cdot \left(\frac{1}{2J_3} \right)^3 + 4 \cdot \left(\frac{1}{2J_1 + 2J_3} \right)^2 \frac{1}{4J_1 + 2J_3} \right) ,$$

$$E^{(4)}_{J_3}(b) = -\lambda^4 \cdot 8 \cdot \left(\frac{1}{2J_3} \right)^3 ,$$

$$E^{(4)}_{J_3}(c) = -\lambda^4 \left(4 \cdot \left(\frac{1}{2J_3} \right)^2 \frac{1}{2J_1 + 2J_3} + 4 \cdot \left(\frac{1}{2J_1 + 2J_3} \right)^3 \right) .$$

We do not simplify the expressions here so that their origin can be traced. For arbitrary $J_1, J_3 > 0$, we find the following hierarchy for the energy lowering corrections $E^{(4)}_{J_3}$:

$$|E^{(4)}_{J_3}(c)| < |E^{(4)}_{J_3}(a)| < |E^{(4)}_{J_3}(b)|\,.$$

This implies that the energetically favored configuration is (b), followed by (a), and then (c). We confirm our analytic calculation by a numeric evaluation of the fourth order ground-state energy correction. Turning back to the ground-state plaquettes in Figure 5.14, we look at the composition of those from the elementary unit cells. Plaquette 2 consists of only (c) and is thus the energetically least beneficial configuration. Plaquette 1 and 3 both contain two times (b). Plaquette 1 contains four times (a), while plaquette 3 contains two times (a) and two times (c). We conclude that plaquette 1 is favored by the magnetic field in fourth order.

On the infinite lattice, we notice that the full lattice can be spanned by purely type 1 plaquettes. The resulting ground-state configuration in terms of ferromagnetic bonds is shown in Figure 5.17.

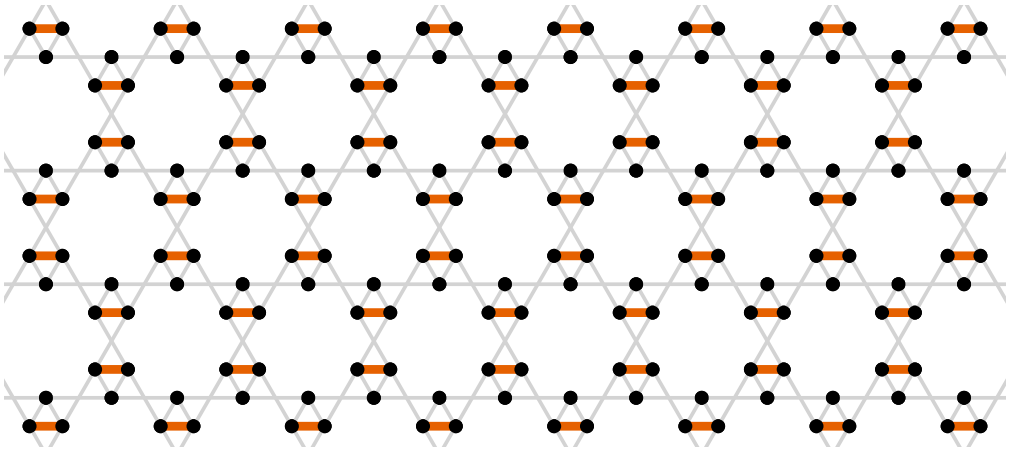

Figure 5.17.: Classical ground-state configuration selected by the magnetic field perturbation due to diagonal ground-state energy corrections in h^4. The configuration is visualized in terms of ferromagnetic (orange) and antiferromagnetic (light gray) bonds distributed over the lattice.

It is obvious that this configuration is symmetric with respect to a global spin flip and can be rotated by 120°. It is thus six-fold degenerate. We conclude that this finite number of ground states is selected from the infinitely degenerate classical ground-state manifold by a small transverse field in an order-by-disorder scenario. Note that the lattice geometry requires that not only the distribution of ferromagnetic bonds, but also the explicit spin configuration is the same for each elementary unit cell. Thus, the momentum corresponding to such a configuration is $\boldsymbol{k} = (0, 0)$. This is precisely the momentum $\boldsymbol{k}_{\min}$ of the one quasi-particle gap we found in the high-field limit in subsection 5.2.1 which connects the two limiting cases.

5.2.3. Analysis of the criticality of the quantum phase transition for $J_1 = J_3$

In this section, we analyze the criticality of the quantum phase transition between the limits discussed in the previous two sections. In the low-field limit, diagonal energy corrections in fourth order select a quantum ordered state from an infinitely degenerate classical ground-state manifold. In this ordered state each elementary unit cell is in the same configuration. In the high-field limit, a polarized phase with related gap momentum $\boldsymbol{k}_{\text{min}} = (0, 0)$ is realized. The analysis in subsection 5.2.1 indicates a second-order phase transition between those phases. We conjecture this phase transition lies in the 3d Ising criticality class with $\nu_{\text{3d Ising}} = 0.629971(4)$ [76].

The critical exponent $z\nu$ of the gap closing is extracted from the DlogPadé extrapolations, where we have the dynamical critical exponent $z = 1$. We analyze the convergence behavior of the extrapolants $dP[L, M]$ by structuring them into families with constant $d = L - M$ and plot λ_c and ν as a function of the order $r = L + M + 1$. Results for $|d| \leq 3$ are shown in Figure 5.18.

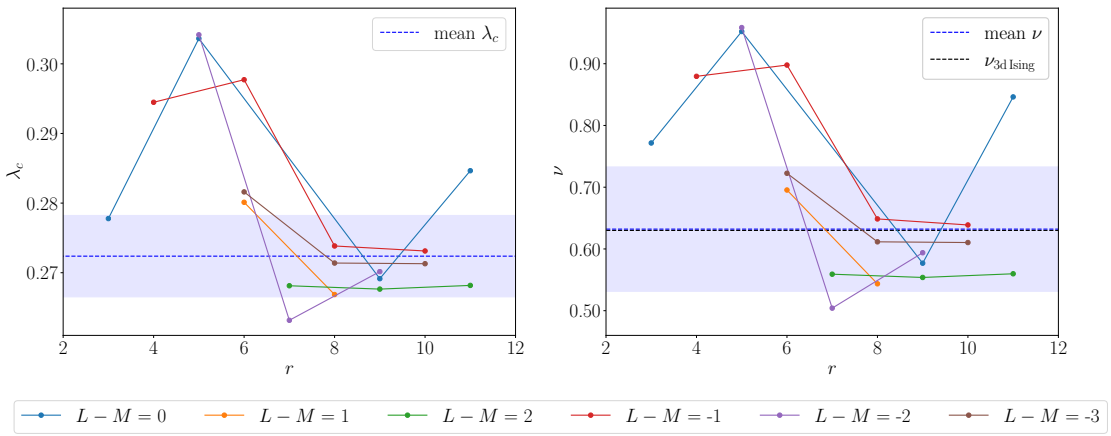

Figure 5.18.: Convergence behavior of the critical point λ_c (left panel) and critical exponent ν (right panel) extracted from the DlogPadé extrapolants $dP[L, M]$ in the considered order $r = L + M + 1$. The extrapolants are structured into families by connecting extrapolants with the same $d = L - M$. We show only extrapolants with $|d| \leq 3$. To obtain a mean value for λ_c and ν we average over the extrapolants of highest order for each shown family. The calculated means $\lambda_c = 0.272 \pm 0.006$ ($\nu = 0.632 \pm 0.101$ are drawn as a dashed blue lines, with the highlighted areas indicating the standard deviations of the individual extrapolants. The black dashed line represents the literature value for $\nu_{\text{3d Ising}} = 0.629971(4)$ [76].

Except for one outlier, $dP[5, 5]$, the extrapolants converge well with increasing order r. We calculate the mean value for the critical point by averaging over the highest order extrapolants per family, resulting in

$$\lambda_c = 0.272 \pm 0.006\,.$$

Analogously, we calculate the mean critical exponent,

$$\nu = 0.632 \pm 0.101\,.$$

The resulting critical exponent is in good agreement with the literature value of the expected 3d Ising universality class, $\nu_{\text{3d Ising}} = 0.629971(4)$ [76].

Comparing the degree of agreement of the critical value ν we obtain with the literature value of the conjectured criticality, we notice a large difference between the J_1-J_2 and the J_1-J_3 model (with equal J_i). For the J_1-J_2 model, the obtained critical exponent is roughly 20% too high, while for the J_1-J_3 model, the obtained exponent agrees with the literature value almost perfectly. In subsection 5.1.3, we argued that the considered perturbation order $k_{\max} = 11$ is too low to describe fluctuations in the J_1-J_2 model on a large enough scale to capture the relevant ordering structure, which spans 3 unit cells, and the extracted gap is not sufficiently dominated by a power-law behavior. In contrast to this, the relevant order of fluctuations in the J_1-J_3 model only spans one unit cell. Additionally, the geometry of the J_3 bonds is such that further apart elementary unit cells are connected in lower orders. In particular, in order 11, hopping processes can span 11 elementary unit cells in $\boldsymbol{a}_1$ ($\boldsymbol{a}_2$) direction. The combination of those two factors suggests that the results obtained for the J_1-J_3 model describe the relevant physics already well in order 11, while the J_1-J_2 model might require the computation of higher orders.

5.2.4. Phase transition for arbitrary J_3/J_1

Finally, to conclude the discussion of the J_1-J_3 TFIM, we look at arbitrary ratios of J_3/J_1. The low-field limit as discussed in subsection 5.2.2 actually holds for arbitrary $J_3 > 0$. The deciding role the J_3 bonds play for the ground-state configurations is connecting the J_1-triangles and thus placing restrictions on the position of the ferromagnetic J_1 bonds. For this, however, the strength J_3 is irrelevant. The momentum of the gap in the high-field limit is given by $\boldsymbol{k}_{\min} = (0, 0)$ independently from the ratio J_3/J_1. In the case of a gap closing, we thus expect a phase transition in the 3d Ising criticality class independent from the ratio J_3/J_1.

We perform DlogPadé extrapolations to extract the critical point λ_c and the critical exponent ν for various ratios of J_3/J_1. Analogously to subsection 5.1.4, the interaction strengths are parameterized by θ as follows:

$$J_1 = \cos(\theta)\, J\,,$$
$$J_3 = \sin(\theta)\, J\,.$$

The previously discussed symmetric case $J_1 = J_3$ is recovered for $\theta = \pi/4$. This particular parametrization yields $J_1 = J_3 = J/\sqrt{2}$, which results in a rescaling of the critical point $\lambda_{c,J_1=J_3}$ compared to subsection 5.2.3. In Figure 5.19 we show the results obtained for selected individual extrapolants. The values for the symmetric case ($\lambda_{c,J_1=J_3}$ and $\nu_{J_1=J_3}$) as calculated in subsection 5.2.3 are plotted as blue lines for reference. Note that for arbitrary ratios, we have calculated the gap only up to order $k_{\max} = 10$ due to the increased complexity (two bond colors are needed instead of one).
For the critical points, we observe the same qualitative behavior of all extrapolants, with some quantitative deviations in extrapolants of lower orders (e.g. $dP[2, 3]$, $dP[3, 2]$, plotted in lower opacities in Figure 5.19) which we thus exclude from the discussion. The accordance is greater for $J_1 < J_3$ than for $J_1 > J_3$. Coming from the symmetric case and decreasing θ, the gap closes at increasing λ. Similarly to the J_1-J_2 model, no gap closing tendencies can be observed for $J_3/J_1 \lesssim 0.15$ ($\theta \lesssim 0.15$). In the limit $J_3 = 0$ ($\theta = 0$) the system is given by decoupled triangles of J_1 bonds. On such finite systems, no phase transition is possible. With decreasing J_3 this limit is approached, and we assume that the gap closing is no longer described by the perturbative series in the obtained order. For $J_1/J_3 \to 0$ ($\theta \to \pi/2$), the critical value tends to $\lambda_c \approx 0.5$.

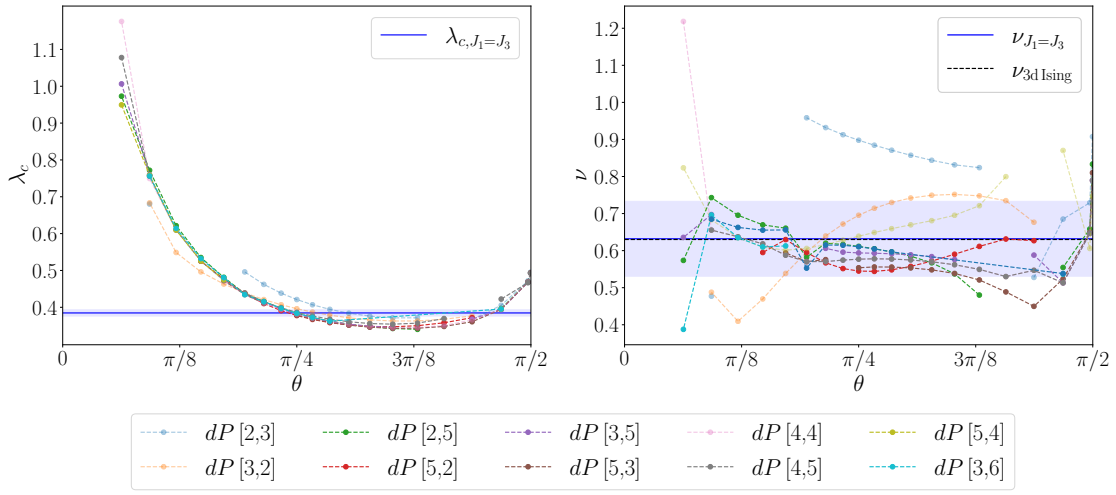

Figure 5.19.: Critical points λ_c (left panel) and critical exponents ν (right panel) for various ratios of J_3/J_1 parameterized by θ as given in the main text. The plots show the results obtained from individual selected DlogPadé extrapolants in different orders. Extrapolants which show deviations from the (qualitative) behavior of the bulk are shown in lighter opacities. The blue lines and shaded regions show the values $\lambda_{c,J_1=J_3}$ and $\nu_{J_1=J_3}$ with their standard deviations as calculated in subsection 5.2.3, respectively. Note that the value $\lambda_{c,J_1=J_3}$ is rescaled due to the modified definition of $J_{1,3}$. The black dashed line in the right panel shows the literature value for the assumed 3d Ising criticality of the phase transition, $\nu_{3\mathrm{d\,Ising}} = 0.629971(4)$ [76].

As discussed in subsection 5.2.2, the case $J_1 = 0$ corresponds to decoupled chains of J_3 bonds spanning the lattice. The critical point of the antiferromagnetic TFIM on a linear chain lies at $\lambda_c = 0.5$, as the model is self-dual with respect to $J = h$ [78]. We recover this limit for very small J_1/J_3, for example we find $\lambda_c \approx 0.496$ for $J_1/J_3 = 0.001$.
For the critical exponents, more deviations in between the individual extrapolants are observed. Still, we can deduce a qualitative behavior from the bulk of high-order extrapolants. For $\theta \lesssim 0.5$ the critical exponents increase and scatter more, as the limit of isolated triangles is approached. For most of the range however, the critical exponent stays approximately constant and within the range of the critical exponent $\nu_{J_1=J_3}$ calculated in the previous subsection. This is consistent with our conjecture of 3d Ising criticality for arbitrary J_3/J_1.

5.3. J_1-J_2-J_3 transverse-field Ising model

The discussion of the limiting cases $J_2 = 0$ or $J_3 = 0$ in sections 5.1 and 5.2 allowed us to understand some underlying mechanisms of the full model. In particular, we could understand the effects of a transverse magnetic field perturbation on classical ground states in the low-field limit. In both cases, we found the selection of a finite subset of quantum ordered states from an infinitely degenerate classical ground-state manifold by the perturbation in an order-by-disorder scenario. In the high-field limit of the J_1-J_2 model, we found a phase transition to the low-field limit which we propose lies within the 3d XY criticality class, with gap momentum $\boldsymbol{k}_{\mathrm{min}} = \pm\left(\frac{2\pi}{3}, -\frac{2\pi}{3}\right)$. In the high-field limit of the J_1-J_3 model, we found a phase transition

within the 3d Ising criticality class, with gap momentum $\boldsymbol{k}_{\min} = (0, 0)$. In this section, we will combine these findings to understand general combinations of J_2 and J_3 to the full J_1-J_2-J_3 TFIM.
We start by calculating the one quasi-particle dispersion in the high-field limit as a series up to order $k_{\max} = 9$ for variable $J_{1,2,3}$, We parameterize the interaction strengths $J_{2,3}$ by θ as follows:

$$\begin{aligned} J_1 &= J\,, \\ J_2 &= \cos(\theta)\, J\,, \\ J_3 &= \sin(\theta)\, J\,. \end{aligned}$$

We recover the previously discussed J_1-J_2 TFIM for $\theta = 0$ and the J_1-J_3 TFIM for $\theta = \pi/2$. We expect the J_1-J_2-J_3 TFIM to be dominated by these two limiting cases for a certain extent of θ. This expectation is met when looking at the one quasi-particle dispersion. For $\theta \in [0, \pi/4)$, we find the minima of the dispersion at $\boldsymbol{k}_{\min} = \pm\left(\frac{2\pi}{3}, -\frac{2\pi}{3}\right)$ like for the J_1-J_2 TFIM. For $\theta \in (\pi/4, \pi/2]$, we find the minimum of the dispersion at $\boldsymbol{k}_{\min} = (0, 0)$ like for the J_1-J_3 TFIM. The gap is again calculated as a series expansion by diagonalizing the Hamiltonian at the respective minimum, yielding two different expressions for the distinct ranges of θ. We perform (Dlog)Padé extrapolations of the gap and extract the critical point and exponent for various θ. Considering the respective averages over extrapolants obtained from orders $k \geq 6$ yields the results shown in Figure 5.20. The error-bars indicate the standard deviations of the averages. Note that differences from previously stated values for the two limiting cases arise due to the lower order $k_{\max}$ of the series and different extrapolants being taken into account.

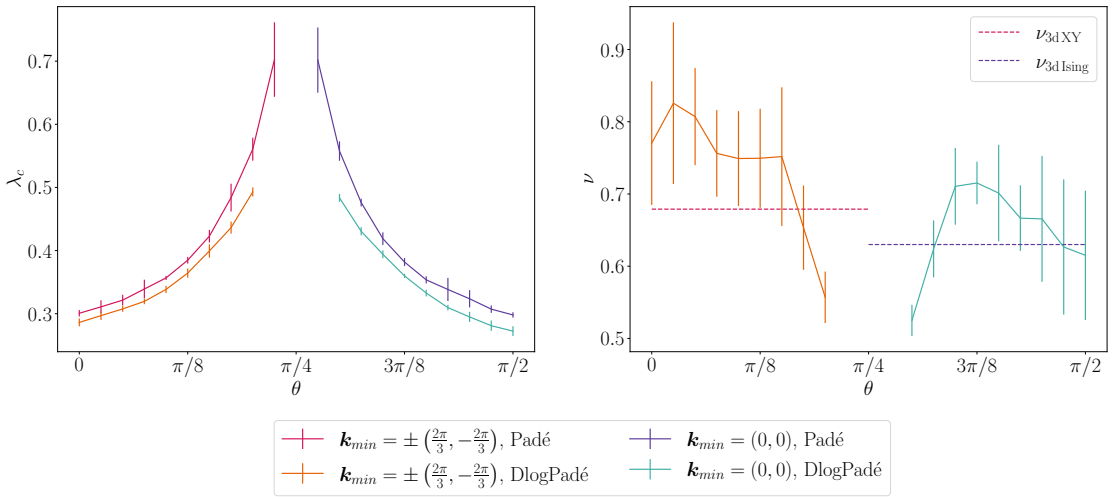

Figure 5.20.: Critical points λ_c (left panel) and critical exponents ν (right panel) in the J_1-J_2-J_3 TFIM parameterized by θ as given in the main text. The shown values are obtained by averaging over non-defective extrapolants of orders $k \geq 6$, with the error bars representing the respective standard deviations. As discussed in the main text, the momentum $\boldsymbol{k}_{\min}$ at which the gap closes depends on θ, as drawn in different colors. The literature values of the critical exponents expected for the two momenta, $\nu_{3d\,XY} = 0.679(7)$ [75] and $\nu_{3d\,Ising} = 0.629971(4)$ [76], are drawn as dashed lines in the respective ranges for θ in the right panel.

A third distinct parameter is $\theta = \pi/4$, where we find a 'crossover' between the two limiting cases,

as $J_2 = J_3 = J/\sqrt{2}$. We find $\boldsymbol{k}_{\min} = \pm\left(\frac{2\pi}{3}, -\frac{2\pi}{3}\right)$ for $\theta = \pi/4$. Interestingly, the lowest energy band stays flat up to and including order 6 and only becomes dispersive in order 7. We do not investigate this behavior further in the scope of this thesis.

Coming from the limiting cases $\theta = 0, \pi/2$ and increasing the admixture of the 'third interaction' towards $\theta = \pi/4$, the critical point λ_c increases approximately symmetrically. Meanwhile, the degree of accordance between the individual extrapolants decreases as the critical point moves to larger values which are less well described by the perturbative series expansion.
The critical exponent remains roughly constant for $\theta \in [0, 0.5]$ and then drops quickly. Coming from $\theta = \pi/2$, the critical exponent first increases monotonously down to $\theta \approx 1.1$ and then also drops rapidly. These rapid declines happen approximately in the range for θ where the critical point increases drastically and the individual extrapolants are less well converged. Thus, the reliability of our estimate is decreased. Note that the decrease in the standard deviation around $\theta = \pi/4$ is due to the smaller number of non-defective extrapolants. It is interesting no note the ratio between J_2 and J_3 at the values where this decline occurs. We find $J_2 \approx 1.83\, J_3$ for $\theta = 0.5$ and $J_3 \approx 1.96\, J_2$ for $\theta = 1.1$. Thus, the drop happens approximately where the dominating interaction drops below twice the strength of the weaker one and the ratio between the two becomes more balanced. It seems that the gap closing is hindered by an interplay of J_2 and J_3 with the same order of magnitude.

We continue by discussing the low-field limit. We start by considering the case $h = 0$. In the limiting cases of the J_1-J_2 TFIM and the J_1-J_3 TFIM, we approached the determination of possible classical ground-state configurations by considering the decomposition of the lattice into circular plaquettes. For both cases we found an infinite number of ground-state configurations, driven by the requirement to have exactly one J_1 ferromagnetic bond per small triangle. We find that for $J_2 > J_3$, all ground states identified in the J_1-J_2 model remain ground states, and vice versa. This can be seen by systematically determining the number of ferromagnetic J_3 bonds in a classical J_1-J_2 ground state (and vice versa). We decompose the lattice into elementary unit cells which take the bonds into account. We choose to define a unit cell as depicted in Figure 5.21, such that it contains:

- 6 sites, along with
- 2 small J_1-triangles (i.e. 6 J_1 bonds) and
- 6 large J_1-J_2-J_3-triangles (i.e. 6 J_2 and 6 J_3 bonds), each connected to one small J_1-triangle.

As already mentioned, each small triangle has exactly one ferromagnetic J_1 bond. With this, both small triangles are 'satisfied', as well as two of the large triangles. For the other four large triangles, either a J_2 or J_3 bond has to be ferromagnetic, as those cost less energy than a J_1 bond. Thus, for $J_2 > J_3$ in all of the four remaining large triangles the J_3 bond is ferromagnetic. On the full unit cell, we therefore have 1/3 ferromagnetic J_1 bonds, zero ferromagnetic J_2 bonds and 2/3 ferromagnetic J_3 bonds. It is not possible to find a configuration with less J_3 bonds, and all classical ground-state configurations from the J_1-J_2 model have the same energy for $h = 0$. The same holds for $J_3 > J_2$ with J_2 and J_3 interchanged. Note that none of the spin configurations which are a ground state for $J_2 > J_3$ are a ground state for $J_3 > J_2$, and vice versa. For $J_2 = J_3$, it is not defined whether the J_2 or J_3 bond is ferromagnetic on the four large triangles. Note however, that for two large triangles which intersect, the same J_i is chosen for both triangles. Hence, all classical J_1-J_2 and J_1-J_3 ground states are ground states for $J_2 = J_3$.

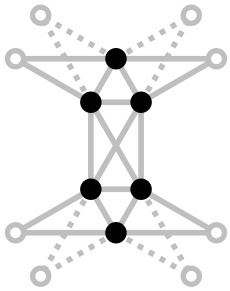

Figure 5.21.: Depiction of an elementary unit cell in the J_1-J_2-J_3 model. The unit cell contains 6 sites, drawn as black dots, and 6 J_i bonds ($i = 1, 2, 3$), drawn as gray lines. The dashed lines and outlined circles visualize the integration of the unit cell into the lattice.

Thus, the ground-state degeneracy is extensive for any θ for $h = 0$.

Now consider switching on a small magnetic field $h > 0$. We already found that for $\theta = 0$, the perturbation selects the subset of ground states with a maximum number of resonating plaquettes, shown in Figure 5.8. For $\theta = \pi/2$, the perturbation selects a subset of ground states where all ferromagnetic bonds are parallel to each other (Figure 5.17), which we will term 'striped' J_3 ground state. As argued in the previous paragraph, the maximally resonating ground state has zero ferromagnetic J_2 bonds and $2/3$ ferromagnetic J_3 bonds. The striped J_3 ground state has zero ferromagnetic J_3 bonds and $2/3$ ferromagnetic J_2 bonds. Thus, for $J_2 > J_3$ the maximally resonating ground state is favored over the striped one, and vice versa for $J_3 > J_2$. Following this argumentation we extend our model of the respective order-by-disorder scenario from the J_1-J_2 (J_1-J_3) TFIM to arbitrary $J_2 > J_3$ ($J_3 > J_2$).

We can further extend the conjectured criticality from the limiting models to the full J_1-J_2-J_3 model with $\theta \neq \pi/4$. For $J_2 > J_3$, the momentum of the gap, $\boldsymbol{k}_{\min} = \pm\left(\frac{2\pi}{3}, -\frac{2\pi}{3}\right)$, and the critical exponent obtained for $\theta \in [0, 0.5]$ let us conclude that the transition from the polarized high-field phase to the clock-ordered low-field phase lies within the 3d XY criticality class. We contribute deviations of the critical exponent as the limit $J_2 = J_3$ is approached to the gap closing being less well described by the perturbative series. For $J_3 > J_2$, we find the gap momentum $\boldsymbol{k}_{\min} = (0, 0)$. The critical exponent however increases as J_2 is increased, for which we currently have no explanation. To the current status, we still conjecture that the phase transition lies within the 3d Ising criticality class. The $J_2 = J_3$ case still requires further analysis, which remains an open point in this thesis.

5.4. J_1-J_2-J_3 transverse-field Ising model with van-der-Waals decay

In the final section of this chapter, we turn to the originally defined TFIM with algebraically decaying interaction strength ($\alpha = 6$). Here, the three interaction strengths are related to each other by the distance r they span on the lattice with r^{-6}, leaving us with

$$\begin{aligned} J_1 &= J\,, \\ J_2 &= \frac{1}{27} J\,, \\ J_3 &= \frac{1}{64} J\,. \end{aligned}$$

We already calculated the one quasi-particle dispersion for arbitrary J_i up to order $k_{\max} = 9$ (section 5.3), so we only have to plug in the specific values for the interaction strengths. Keeping the previous section in mind, note the hierarchy of interaction strengths $J_1 \gg J_2 > J_3$ which is given naturally by the algebraic decay. Thus, we find the gap at momentum $\boldsymbol{k}_{\min} = \pm\left(\frac{2\pi}{3}, -\frac{2\pi}{3}\right)$. Figure 5.22 shows the results obtained for the gap $\Delta(\lambda)$. The bare series in order $k_{\max} = 9$ is shown in purple, with lower orders plotted in decreasing opacities. From their spread we can deduce that the bare series is converged well until $\lambda \approx 0.5$. Alongside, (Dlog)Padé extrapolants of the bare series in orders $k \geq 7$ with $d = L - M \leq 3$ are plotted. The extrapolants are mainly converged over the shown range, but start to spread towards higher λ. It is clearly visible that the extrapolants are converged over a larger range than the bare series. Over the range where we assume our results are valid, no gap closing tendencies are present.

For this we suggest the following explanation. First, note that the system is strongly dominated by the interaction J_1, with $J_2/J_1 \approx 0.04$. From subsection 5.1.4, we know that in the J_1-J_2 TFIM no gap closing can be detected within our perturbative approach for values $J_2/J_1 \lesssim 0.2$. Due to the even lower influence of J_3, the energy gap is approximately given by the one for the J_1-J_2 TFIM. Further, $J_3/J_1 \approx 0.02$, for which we similarly find no gap closing within the range described by our results in the J_1-J_3 TFIM in subsection 5.2.4. In both reduced models, we argued that this results from approaching the limit of decoupled triangles for $J_1 \gg J_2(J_3)$. The takeaway is thus, that the absence of gap closing is consistent with the findings for the J_1-J_2 TFIM by which the full model is approximately described.

It is illustrative to elaborate further on the limiting case of $J_2 = J_3 = 0$, which we term the 'J_1 TFIM'. As already mentioned, it is easily seen that the lattice decomposes into isolated triangles, where three sites are connected by J_1 bonds (compare Figure 2.2). On such a triangle, the Hilbert space has dimension 8, and the TFIM can be solved exactly, as the respective Hamiltonian can be represented as an 8×8 matrix. After diagonalization of this matrix we can compute the elementary excitation gap on a triangle. The result is depicted in Figure 5.22. The gap on the isolated triangles shows the same qualitative behavior as the gap extrapolated from the J_1-J_2-J_3 TFIM with van-der-Waals decay, underlining the dominance of the J_1 interaction. However, it is always larger than the extrapolated gap and the difference between them increases with λ, as $J_{2,3}$ start to become relevant. We know that the gap of the triangles will not close for $\lambda \to \infty$, as there can be no phase transition on a finite system. Within the perturbative approach, we simply stay too close to the limit of decoupled triangles to make a reasonable statement about a possible phase transition.

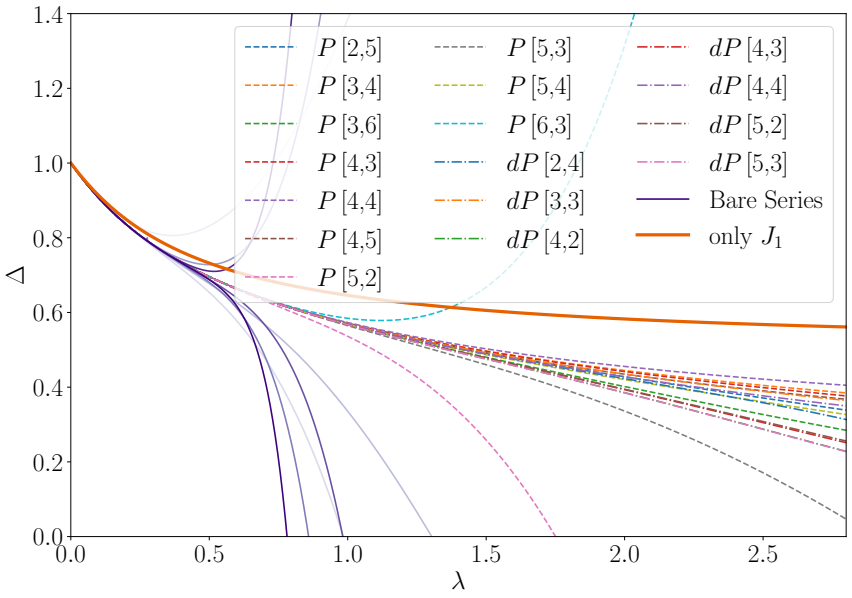

Figure 5.22.: One quasi-particle excitation gap Δ in the J_1-J_2-J_3 TFIM with algebraically decaying interaction strength with $\alpha = 6$. The bare series in the maximal order $k_{\max} = 9$ is shown along lower orders in lower opacities and the obtained Padé and DlogPadé extrapolants $(d)P[L, M]$ as a function of $\lambda = J/2h$. Note that H^{TFIM} is defined such that Δ is calculated in units of $2h$. Only non-defective extrapolants in orders $k \geq 7$ with $L - M \leq 3$ are shown. The thick orange line shows the gap in the limit of $J_2 = J_3 = 0$, where the lattice is decomposed into isolated triangles.

Alongside this explanation, we note that in the discussion of the J_1-J_2-J_3 model in section 5.3 we found that the critical point increases rapidly around the point where $J_2 \lesssim 2\,J_3$. For the algebraic decay we find $J_2/J_3 \approx 2.37$, which lies close to this ratio. Combining this with the system being dominated by purely local triangles, we understand why no gap closing can be observed within the scope of our perturbative approach.

6. Discussion of the Fendley-Sengupta-Sachdev model

In this chapter, we discuss our results for the full FSS model. The initial goal is to obtain a quantum phase diagram in the parameter space $(\Omega/\delta, V/2\tilde{\Delta})$. We will see that this is a challenging task which can not be accomplished with series expansions about the weak-interaction-strength limit alone, which are discussed in section 6.1. We gain further insights by the examination of the classical limit of the FSS model in section 6.2. Additionally, on the specific parameter line where $\delta/V \approx 2.105$, the FSS model is equivalent to the TFIM, which was already discussed in section 5.4. We summarize our findings in the draft of a quantum phase diagram in section 6.3 and try an interpretation taking in particular our findings concerning the TFIM from chapter 5 into account. At this point, we want to stress that we investigate the FSS model as defined in section 2.1, namely with a long-range algebraically decaying van-der-Waals interaction between Rydberg-excited atoms. This particular interaction is enforced by the physical system of Rydberg atom arrays we aim to describe.

6.1. Weak-interaction-strength limit of the V_1-V_2-V_3 Fendley-Sengupta-Sachdev model

In this section, we discuss the limit of weak interaction strengths, $V \ll \tilde{\Delta}$, in the FSS model defined in Equation (2.1). The one quasi-particle dispersion is calculated as a series in $\lambda = V/2\tilde{\Delta}$ up to order $k_{\max} = 6$ using the pCUT method (chapter 3) on clusters[1]. Owing to the complexity of the T_n operators of this model defined in section 3.1, computational efforts increase quickly with the perturbation order and we could not obtain higher orders. For the calculations, we define the T_n operators for arbitrary $\phi = \arctan(\Omega/\delta)$ such that we obtain the quasi-particle dispersion as a function of λ with parameter $\phi(\Omega/\delta)$.
We start by choosing a specific set of parameters, namely $(\delta = 10, \Omega = 1)$. Figure 6.1 shows the six energy eigenvalues obtained by the diagonalization of H_k for $\lambda = 0.2$, sorted by energy. The momentum coefficients k_1, k_2 are defined with respect to the lattice vectors given in Equation (2.3). Note that due to the rescaling of the Hamiltonian we obtain the quasi-particle energy in units of $2\tilde{\Delta} = \sqrt{\delta^2 + \Omega^2}$. In other words, the one quasi-particle energy for vanishing interaction strength $V = 0$ is normalized to one. We observe that this energy is lowered due to the interaction for all six bands for this parameter set. The minimum of the dispersion is located at momenta $\boldsymbol{k}_{\min} = \pm\left(\frac{2\pi}{3}, -\frac{2\pi}{3}\right)$. We find that this holds for any values δ and Ω. Note that although all six energy bands are dispersive, they are relatively flat. The elementary excitation gap Δ is given by explicitly diagonalizing H_k at the minimum, yielding an analytic expression for $\Delta(\lambda, \phi)$ as a series in λ.

Figure 6.2 shows the bare series in the maximal order ($k_{\max} = 6$) in the perturbation, along with the series in lower orders in lighter shades of purple. Comparing the different orders indicates

[1] In contrast to the calculations for the TFIM, we do not perform a full graph decomposition here.

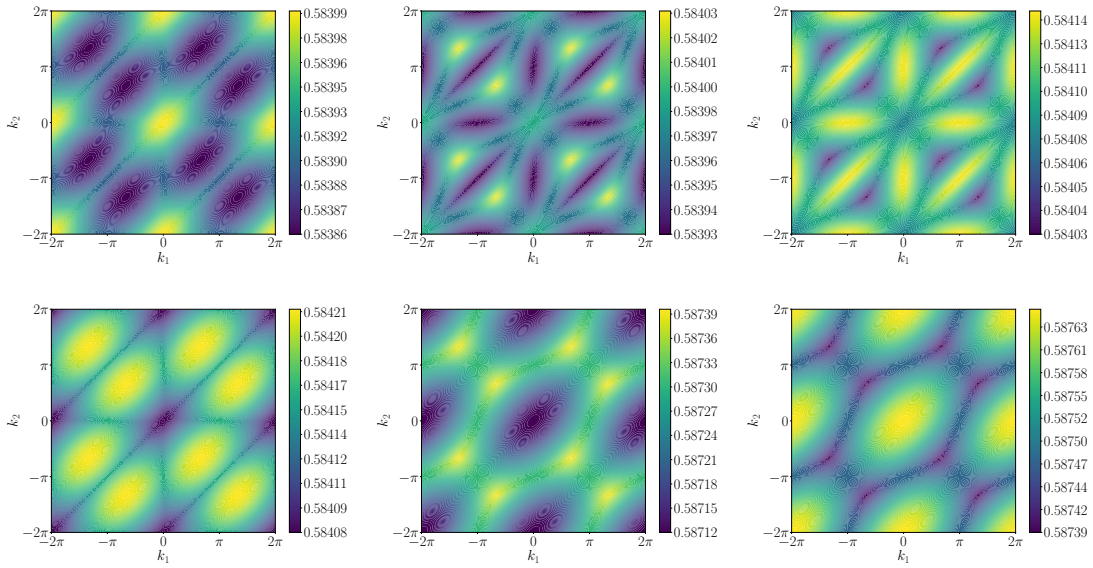

Figure 6.1.: One quasi-particle dispersion in the FSS model for $\delta = 10$, $\Omega = 1$ and $\lambda = 0.2$. The six energy bands obtained from diagonalizing the respective Hamiltonian in momentum space are shown sorted by energy. The momenta k_1, k_2 are defined with respect to the translational lattice vectors $\boldsymbol{a}_1, \boldsymbol{a}_2$. The minima of the dispersion lie at $\boldsymbol{k}_{\min} = \pm\left(\frac{2\pi}{3}, -\frac{2\pi}{3}\right)$.

good convergence of already the bare series in the shown region. (Dlog)Padé extrapolations are performed to confirm the convergence. All non-defective extrapolants are shown in Figure 6.2. Clearly, all extrapolants lie almost on top of each other, as well as on top of the bare series and indicate a closing of the gap in a narrow region around $\lambda \approx 0.5$.
Averaging over all Padé extrapolants yields the critical point of the gap closing

$$\lambda_c = 0.489 \pm 0.006\,,$$

and averaging over all DlogPadé extrapolants yields

$$\lambda_c = 0.506 \pm 0.013\,.$$

Note that for both extrapolation methods, only extrapolants for which either the numerator degree L or denominator degree M is equal to one are shown, as all other extrapolants are defective and thus sorted out. This includes most of the extrapolants with a small $d = L - M$, which usually tend to show the best convergence behavior. Nevertheless, here the extraction of the critical point seems to work well enough. The low number of extrapolants and the low order of the bare series are however problematic for the determination of the critical exponent from the DlogPadé extrapolants. All DlogPadé extrapolants show a closing of the gap with critical exponent $z\nu > 1$. In particular, we find a spreading over a wide range from $z\nu = 4.18$ to 5.30. This leads to assume that the obtained perturbation order $k_{\max} = 6$ does not suffice in capturing the dominant power-law scaling of the gap around the critical point. Due to this 'slow' closing of the gap, the critical point obtained from the DlogPadé extrapolants is larger than the one obtained from the Padé extrapolants. As we can not determine a reasonable estimate, we will in the following omit

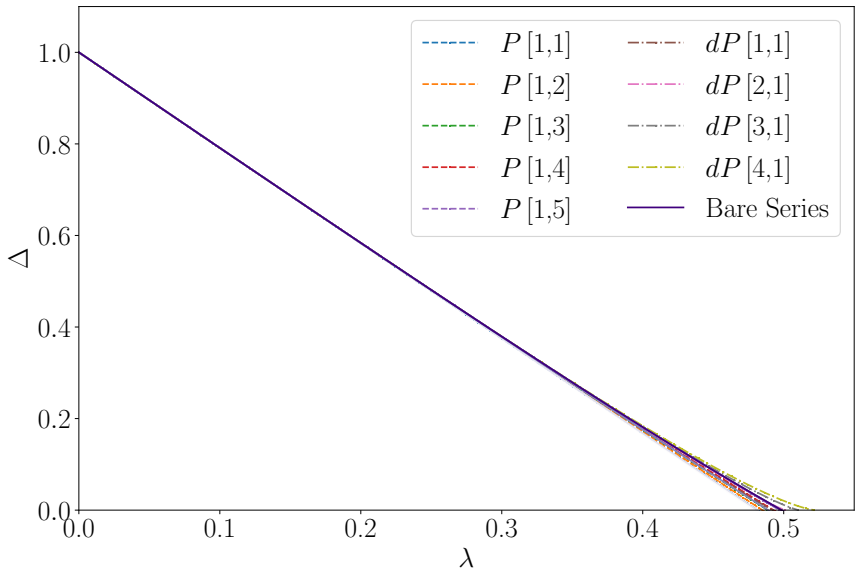

Figure 6.2.: One quasi-particle excitation gap Δ in the FSS model for $(\delta = 10, \Omega = 1)$. The bare series in the maximal order $k_{\max} = 6$ is shown along lower orders in lower opacities and the obtained Padé and DlogPadé extrapolants $(d)P[L, M]$ as a function of $\lambda = V/2\tilde{\Delta}$. Defective extrapolants are sorted out. Note that H^{FSS} is defined such that Δ is calculated in units of $2\tilde{\Delta}$.

the determination of the critical exponent and concentrate on only discussing the critical point λ_c.

As it has already been elaborated on, the convergence of the bare series and the extrapolants is of high quality for the investigated parameters $(\delta = 10, \Omega = 1)$. We will now observe that the quality of the bare series and the extrapolations depends heavily on the parameter ratio Ω/δ. To understand this, we shortly recapitulate on the definition of the weak-interaction-strength limit. The initial unperturbed Hamiltonian as defined in Equation (2.1) reads

$$H_0^{\text{FSS}} = \frac{\Omega}{2} \sum_i \left(b_i + b_i^\dagger \right) - \delta \sum_i n_i \,.$$

We solve the unperturbed problem with a rotation by $\phi = \arctan(\Omega/\delta)$ into the $\tilde{b}_i, \tilde{b}_i^\dagger$ basis. For $\Omega \ll \delta$, H_0^{FSS} is already almost diagonal and ϕ is small. Accordingly, the rotated density-density interaction $H_1^{\text{FSS}} = \sum_{i<j} V_{ij} \tilde{n}_i \tilde{n}_j$ is only transformed slightly and remains almost diagonal in the particle number n_i. We stay close to the classical limit (see chapter 4 and section 6.2). The parameter set we chose for our first investigation results in a rotation by a small angle $\phi \approx 5.7°$. Let us now deviate further from the classical limit by taking the parameter set $(\delta = 5, \Omega = 1)$ which results in $\phi \approx 11.3°$. The resulting bare series and extrapolants are shown in Figure 6.3 in analogous fashion.

The obtained bare series in different perturbation orders spread more widely with increasing λ

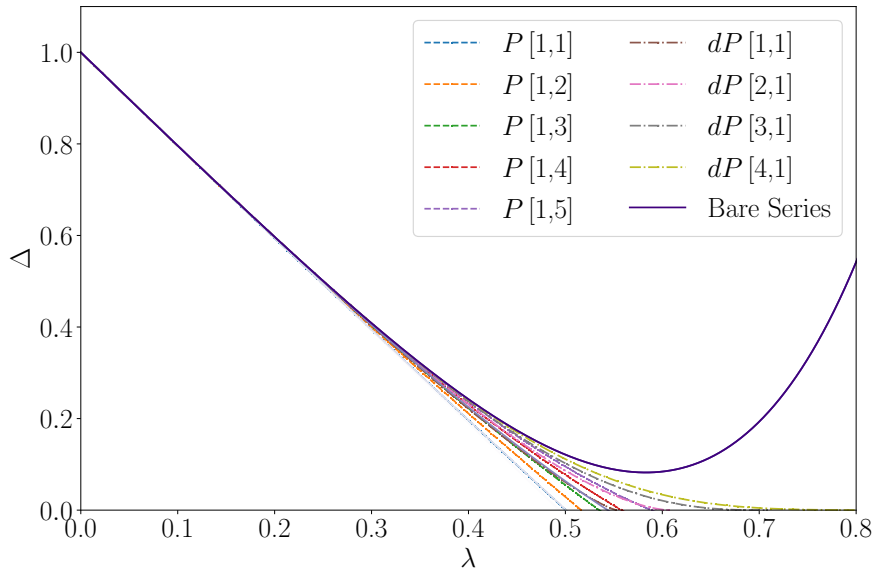

Figure 6.3.: One quasi-particle excitation gap Δ in the FSS model for $(\delta = 5, \Omega = 1)$. The bare series in the maximal order $k_{\max} = 6$ is shown along lower orders in lower opacities and the obtained Padé and DlogPadé extrapolants $(d)P[L, M]$ as a function of $\lambda = V/2\tilde{\Delta}$. Defective extrapolants are sorted out. Note that H^{FSS} is defined such that Δ is calculated in units of $2\tilde{\Delta}$.

and the critical point lies out of the range where the individual orders are converged. Especially the Padé extrapolations seem to be able to estimate the gap better for larger λ compared to the bare series. Nonetheless, a decrease in the agreement of the extrapolants compared to the case in Figure 6.2 is clearly visible. Overall, we find a decrease in the quality of the results with increasing Ω/δ. On the one hand, the region where the gap closes according to the extrapolations gets pushed to higher values of λ. In particular, averaging over all Padé extrapolants for $\Omega/\delta = 1/5$ yields

$$\lambda_c = 0.540 \pm 0.031\,,$$

and averaging over all DlogPadé extrapolants yields

$$\lambda_c = 0.718 \pm 0.202\,.$$

On the other hand, the spread of the extrapolants increases also for smaller λ. While for $\Omega/\delta = 1/10$ the extrapolants lie almost on top of each other up to $\lambda \approx 0.4$, the extrapolants already start spreading around $\lambda \approx 0.3$ for $\Omega/\delta = 1/5$ (compare Figures 6.2 and 6.3). The combination of a decreased range in which the extrapolants are converged and increased gap-closing point only allows us to determine λ_c for $\Omega/\delta \in (0, 1/3)$. We show the results obtained for selected values in that range in Appendix A in analogous fashion to the results for the two values shown in this section.
Assuming the system undergoes a second-order quantum phase transition, the value λ_c where the gap closes indicates the position of the transition. In section 6.3, we combine the obtained

results into the draft of a quantum phase diagram under this assumption. Prior to this however, we analyze the classical limit of the system in the next section.

6.2. Crystalline structures in the classical limit

In this section, we discuss the classical limit of the FSS model, where $\Omega = 0$. Chapter 4 already introduced this limit and gave an intuition for how one can imagine which ground-state configurations are formed. As the Hamiltonian is diagonal in the particle number n_i in the classical limit, the ground states are crystalline structures, where hardcore bosons arrange on the lattice such that the total energy is minimized.
Constructing the phase diagram in the classical limit corresponds to determining the filling fraction f of the system and the realized ground-state configuration for all possible parameters δ/V, which is achieved employing the algorithm described in chapter 4. In order to find the energetically favored ordering pattern, we investigate all unit cells with translational vectors

$$\{i\boldsymbol{t}_1 + j\boldsymbol{t}_2 \,|\, i \in \{-4, 4\}, j \in \{-4, 4\}\}\,, \tag{6.1}$$

where $\boldsymbol{t}_{1,2}$ are defined in Equation (2.3). Although already mentioned, let us stress again that for the classical limit, we take the *full* long-range interaction into account (see the discussion about resummed couplings in chapter 4). This is in contrast to our previous discussions of the V_1-V_2-V_3 FSS model in section 6.1 and the J_1-J_2-J_3 TFIM in chapter 5, where we only considered interactions between the three nearest neighbors. Results presented in this chapter were created in collaboration with Jan Koziol, and are published in similar form in Ref. [46].

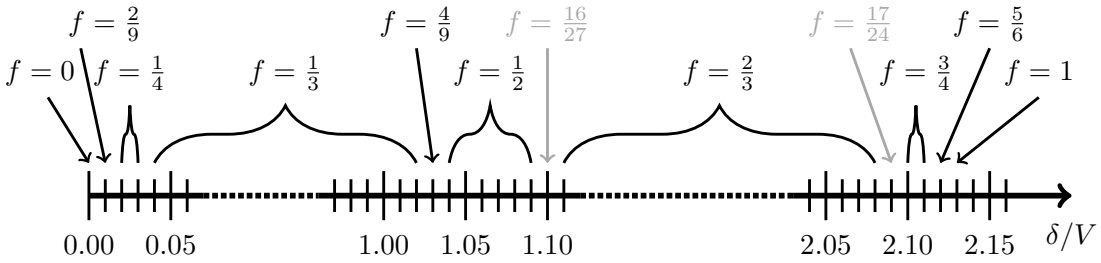

Figure 6.4.: Phase diagram of the classical limit of the FSS model. The phase diagram shows the filling fractions f evaluated on a grid of 0.01 in δ/V. The configurations of relevant encountered phases are shown in Figure 6.5. In between those phases, a staircase of phases with intermediate filling fractions is expected. Some of those intermediate phases lie on the chosen grid and are printed in gray. Note that while the phase diagram is in principle particle-hole symmetric with respect to $\delta/V = \bar{\mu}^{\alpha}/2 \approx 1.063$, not all shown filling fractions have a particle-hole-symmetric counterpart in this visualization. This is simply due to the counterparts not lying on the chosen grid. However, we do find the respective phases on a finer grid and they could be added to the phase diagram.

We present the obtained phase diagram in Figure 6.4. The figure shows which filling fraction f is realized for which ratio δ/V. The ground-state configurations for the filling fractions we consider the most relevant are shown in Figure 6.5. The unit cells of the ordering patterns are indicated as red-shaded boxes. As already reasoned in chapter 4, we find an empty system with $f = 0$

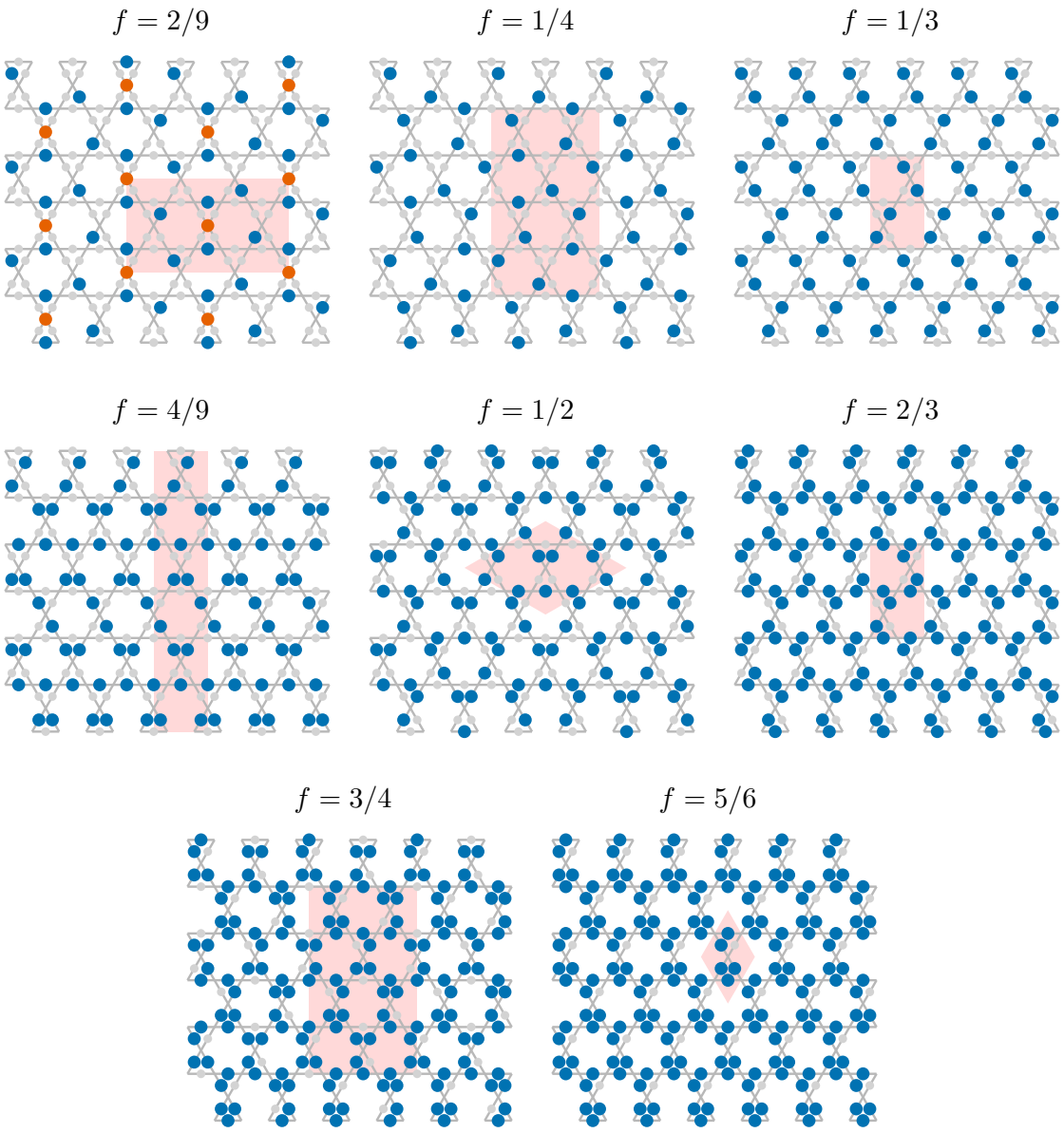

Figure 6.5.: Selected configurations of relevant phases in the classical limit. Blue circles ● indicate sites occupied by one boson, light gray circles ● indicate empty sites. The unit cells of the ordering structures are indicated as red-shaded boxes. In the $f = 2/9$ phase, the connection to a dimer-monomer picture is visualized by marking monomer vertices with orange circles ● .

for $\delta/V \leq 0$ and a fully filled system with $f = 1$ for $\delta/V \geq \bar{\mu}^\alpha$. Considering the full long-range interaction, $\bar{\mu}^\alpha \approx 2.126$ for $\alpha = 6$. To investigate the partially filled phases in between, we choose a sampling grid of 0.01 in δ/V. Figure 6.4 shows which filling fractions are realized for all δ/V lying on this grid. We find that the phase diagram is dominated by a few phases with large extent in δ/V. In particular, $f = 1/3$ for $\delta/V \in [0.04, 1.02]$, $f = 1/2$ for $\delta/V \in [1.04, 1.09]$ and $f = 2/3$ for $\delta/V \in [1.11, 2.08]$. Note that the filling fractions of these extended phases fit the lattice geometry with an elementary unit cell containing 6 sites well. For example, in the $f = 1/3$ phase, in each of the two V_1-triangles within an elementary unit cell, exactly one site is occupied. The unit cell of the corresponding ordering structure consists of only two elementary unit cells, as can be seen in Figure 6.5. As ordering structures with unit cells of significantly larger extent are considered for the determination of the optimal ordering structure, we are confident in the reliability of our results in particular if the ordering structures have unit cells consisting of only a few elementary unit cells. Those configurations with large extent would also be found considering only interactions between the first few neighbors. Due to the rapid decay of the long-range interactions, they dominate the phase diagram.

In between those phases with large extent, we find multiple intermediate phases with smaller extent, e.g. $f = 2/9$, $f = 1/4$ or $f = 4/9$, whose ordering structures are illustrated in Figure 6.5. We further find phases with filling fractions that seem 'unnatural', for example $f = 16/27$. In between the phases presented in Figure 6.4, one could always find an infinite staircase of phases with ordering structures with large unit cells by increasing the resolution of the grid. This is the case due to the chemical potential δ benefiting the occupation of sites in a grand canonical framework. By coincidence, some of the phases within this staircase lie on the grid we chose. Note, however, that as we only consider unit cells up to a certain extent (compare Equation (6.1)), the size of ordering structures we can identify correctly as the ground state is limited. Thus, configurations we find with larger unit cells might not be the actual ground state.

We find that the phase diagram is particle-hole symmetric with respect to $\delta/V = \bar{\mu}^\alpha/2$, as can be concluded from a mapping to the Ising model with longitudinal field (compare chapter 4). For some phases in Figure 6.4, the corresponding particle-hole symmetric counterpart does not lie on the grid of 0.01 in δ/V chosen for the visualization. However, we can always find the counterpart by choosing a finer grid and thereby confirm the symmetry. For $\delta/V = \bar{\mu}^\alpha/2$, the longitudinal field is zero, and we recover the limit $h = 0$ of the TFIM. The filling fraction of the system is then $f = 1/2$. The ground-state configuration we find for this filling fraction is shown again in the left panel in Figure 6.6.
With a Matsubara-Matsuda transformation [42], we can map the hardcore bosonic states $|0\rangle, |1\rangle$ to spin 1/2 states $|\uparrow\rangle, |\downarrow\rangle$ such that occupied sites correspond to spin 'down' and empty sites to spin 'up'. Consider now only the interactions between nearest and next-nearest neighbors, i.e. J_1 and J_2. One can easily draw in all ferromagnetic bonds in the ground-state configuration and compare the resulting distribution of ferromagnetic bonds to the ones discussed in chapter 5. Interestingly, we find exactly the maximally resonating ground-state structure that is favored in the low-field limit of the J_1-J_2 TFIM, shown in the right panel of Figure 6.6. In the discussion of the classical limit of the J_1-J_2 TFIM in subsection 5.1.2, we found an infinitely degenerate classical ground-state manifold, in which the maximally resonating ground state is contained.
Apparently, the full long-range interaction lifts the degeneracy of the classical ground-state manifold and selects the state with a maximal number of plaquettes which allow for resonances induced by a transverse magnetic field as a ground state for $h = 0$. We thus find that the long-range interaction selects the same ground state that is also selected by a small magnetic field.

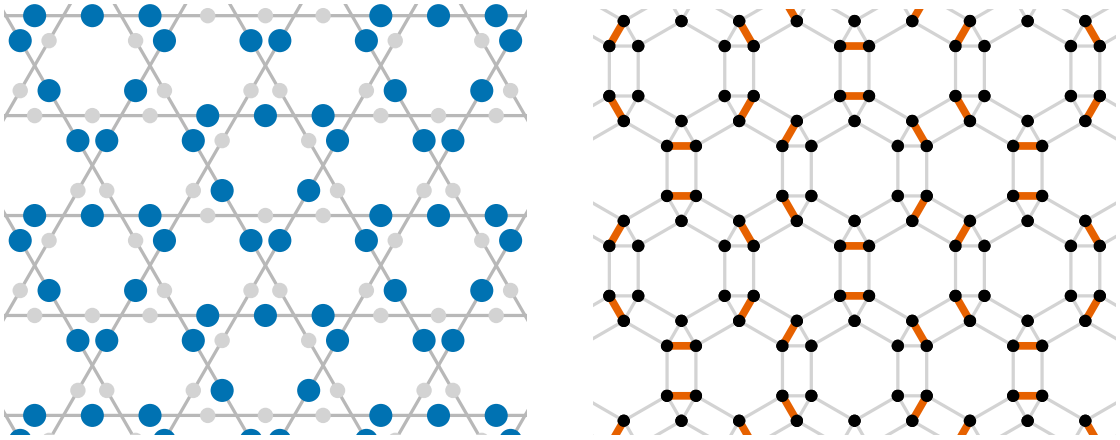

Figure 6.6.: Left panel: Crystalline ground state in the classical limit of the FSS model with filling fraction $f = 1/2$. This configuration is realized for the ratio $\delta/V = \bar{\mu}^{\alpha}/2$, which maps exactly to the TFIM with $h = 0$. Blue circles ● indicate sites occupied by one boson, light gray circles ● indicate empty sites. Note that the gray lines in this figure just serve as a guide to the eye and do not have any physical meaning. The two hardcore bosonic states can be mapped to spin 1/2 states (see main text), resulting in ferromagnetic bonds between two occupied (unoccupied) sites. Drawing in ferromagnetic bonds taking into account nearest and next-nearest neighbor interactions results in the distribution shown in the right panel.
Right panel: Maximally resonating ground state in the low-field limit of the J_1-J_2 TFIM found in subsection 5.1.2. This state is selected from an infinitely degenerate classical ground-state manifold. The configuration is shown in terms of its ferromagnetic bonds, which are drawn in orange. Antiferromagnetic bonds are drawn in light gray. This is the configuration we obtain as a classical ground state when the full long-range interaction is taken into account (see left panel).

On the triangular lattice, a different situation is found. As already stated in subsection 5.1.3, a magnetic field selects $\sqrt{3} \times \sqrt{3}$ clock-ordered states from a degenerate ground-state manifold in the nearest-neighbor TFIM [72]. This is equivalent to our conjecture for the J_1-J_2 TFIM. The ground state in the long-range Ising model on the triangular lattice however is a six-fold degenerate plain stripe-ordered phase [45, 46, 79, 80], which appears to be stable against quantum fluctuations due to a small magnetic field. Hence, coming from the classical nearest-neighbor Ising model, different ground states are selected by the long-range interaction and quantum fluctuations.

Another present crystalline phase we want to highlight is the filling $f = 1/4$ which is realized for $\delta/V \in [0.02, 0.03]$. This filling is closely connected to the prediction of a $\mathbb{Z}_2$ spin liquid state for intermediate δ/Ω by Verresen et al. in Ref. [39], which was described shortly in section 2.3. They work under the premise of a Rydberg-blockade model, where the long-range van-der-Waals interaction is approximated by forbidding the occupation of the six nearest neighbors of an occupied site. In particular, this corresponds to considering interactions up to the third-nearest neighbor, with the additional approximation of setting $V_1 = V_2 = V_3 = +\infty$. They map the limit of small Ω to a dimer picture, where an occupied site on a link of the Kagome lattice corresponds to a dimer connecting the two neighboring vertices of the lattice. Due to the constraint

implemented by the blockading interaction, each vertex can be touched by maximally one dimer. For $f = 1/4$ every vertex is touched by exactly one dimer, resulting in a perfect dimer covering where the blockade model is at maximal filling. Within the blockade model, the space of perfect dimer coverings is macroscopically degenerate. Verresen et al. argue that the regime of a small admixture of monomers (vertices touched by no dimers, exemplarily shown in the $f = 2/9$ phase in Figure 6.5 as orange circles) to a perfect dimer covering is a promising candidate for the realization of a quantum spin liquid state due to induced resonances between dimer states [39].

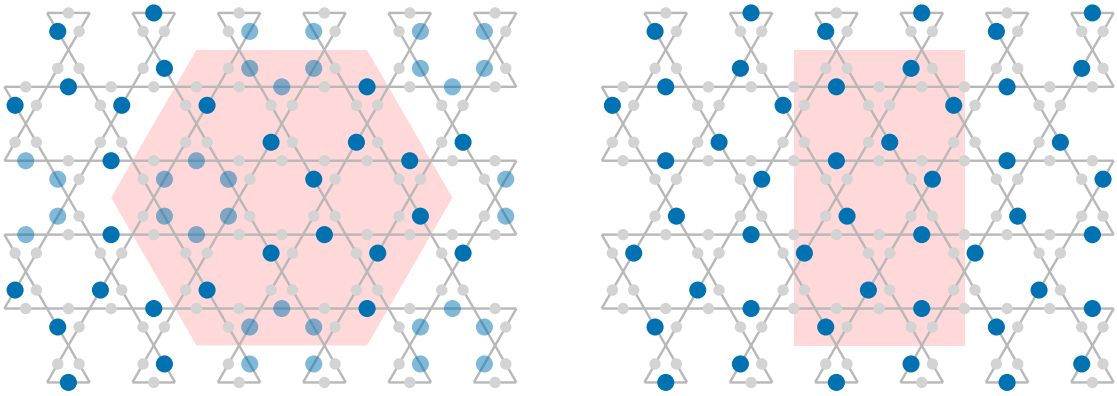

Figure 6.7.: Comparison of the resonating valence bond state found for small $\Omega > 0$ in the limit of perfect dimer coverings in the blockade model in Ref. [39] (left panel) and the crystalline ground state we find in the classical limit $\Omega = 0$ with full long-range interactions with filling fraction $f = 1/4$ (right panel). Blue circles ● indicate sites occupied by one boson, light gray circles ● indicate empty sites and half-opaque blue circles ● indicate half-filled sites taking part in the resonance. The unit cells of the ordering structures are highlighted in red. It can easily be verified that both configurations corresponds to a perfect dimer covering.

In the limit of small Ω, quantum fluctuations select dimer coverings with resonating plaquettes in sixth order perturbation theory, termed valence bond solids (VBS), from the degenerate space of perfect dimer coverings [39, 81–83]. The left panel in Figure 6.7 shows the VBS state found in the blockade model for small $\Omega > 0$ in Ref. [39].

We find that the degeneracy of perfect dimer coverings within the blockade model is lifted by the long-range interaction for $\Omega = 0$. The classical configuration we find for $\Omega = 0$ taking into consideration the full long-range interaction is shown in the right panel in Figure 6.7, where we compare it to the VBS configuration found for small $\Omega > 0$ in the blockade model.

As can be seen, the configuration we find has no plaquettes allowing for resonances. Using the resummed couplings, we can evaluate the energy difference between the two configurations for $\Omega = 0$ to be $\Delta\epsilon = 4.4283 \times 10^{-5}\, V$ [46]. The difference arises as the resonating structure is obtained from a truncated interaction, for which both configurations have the same energy. Differences occur when taking into account interactions between fifth-nearest neighbors, which we do by considering the full long-range interaction. We conjecture that the configuration we find is the ground state for $\Omega = 0$ and that there is a level-crossing transition into the resonating state for some $\Omega > 0$. Quantum fluctuations can be incorporated with a strong-coupling expansion [84]. As argued in Ref. [46], second-order perturbation theory suggests that the long-range configuration is stable against quantum fluctuations up to a level crossing with the resonating state around $\Omega = 0.0078$.

The ordering pattern we find for the filling fraction $f = 1/4$ in the classical limit gives an additional starting point for understanding the system. In particular, in Ref. [39] it is observed that considering the full long-range interaction seems to destabilize the spin liquid phase. The inclusion of long-range interactions into the description for $\Omega > 0$ and its influence on the stability of quantum spin liquid phases remains a difficult topic requiring further investigation. However, the limit of $\Omega = 0$ can be fully understood with the applied approach. Our findings from this classical limit will be integrated into the quantum phase diagram of the full FSS model in the next section.

6.3. Drafting a quantum phase diagram

In this section, we combine our results into a draft for the quantum phase diagram of the FSS model on the link-Kagome lattice. For the unperturbed case $\lambda = 0$, the system is in a trivial polarized phase. As outlined in subsection 2.1.2, the system can be described in terms of spin $1/2$ degrees of freedom which align against a magnetic field whose direction depends on the ratio Ω/δ. All spins point in the same direction, giving rise to the terminology 'polarized'. Switching on the perturbation ($\lambda > 0$) introduces diagonal corrections and quantum fluctuations in terms of spin flips (compare Equation (2.8)). These fluctuations work 'against' the uniform alignment favored by the unperturbed system. However, for small λ the system remains in a polarized phase. The structure of the leading fluctuations over the lattice is given by the momentum of the one quasi-particle gap $\boldsymbol{k}_{\min}$. Increasing λ above a critical value leads to a breakdown of the polarized phase.
A continuous quantum phase transition at a value λ_c is accompanied by a vanishing of the one quasi-particle excitation gap Δ. In section 6.1, we determine the value λ_c at which Δ closes. However, without further analysis of an underlying mechanism we can not definitely attribute this gap closing to a continuous phase transition. In particular, we can not rule out a first-order phase transition at some $\lambda < \lambda_c$. In the following, we construct the quantum phase diagram from the values λ_c of the gap closing. Assuming that the gap closing indicates a continuous quantum phase transition, these values are an estimate for the position of the transition out of the polarized phase.

Figure 6.8 shows a draft for the quantum phase diagram, including the obtained λ_c for discrete values of Ω/δ. We set up the parameter axis of the phase diagram as follows. On the y-axis, we show $\theta = \arctan(\lambda)$, where $\lambda = V/2\tilde{\Delta} = V/\sqrt{\Omega^2 + \delta^2}$. Thus, the polarized phase with $V = 0$ corresponds to $\theta = 0$ and $V = \infty$ corresponds to $\theta = \pi/2$. On the x-axis, we show $\pi/2 - \phi$, where ϕ is defined as in subsection 2.1.2 as $\phi = \arctan(\Omega/\delta)$. Thus, $\pi/2 - \phi = 0$ corresponds to $\delta = 0$ and $\pi/2 - \phi = \pi/2$ corresponds to the classical limit $\Omega = 0$. This parametrization is chosen in order to fit the full parameter ranges from 0 to ∞. Going along the x-axis, Ω/δ is increased, while going along the y-axis, λ is increased. The series expansions in the weak-interaction-strength limit are performed starting at different positions on the x-axis, going straight up into y-direction.

In Figure 6.8 we show the values λ_c of the gap closing obtained from averaging over non-defective Padé and DlogPadé extrapolants separately. Plots of the corresponding extrapolants are shown in Appendix A. The λ_c from DlogPadé extrapolants are consistently larger than the λ_c from Padé extrapolants, as already noted in section 6.1. The λ_c increase with increasing ϕ, as well as the standard deviation of the individual extrapolants and the spread between results from Padé and DlogPadé extrapolations. For $\phi \gtrsim 0.35$, we can not capture a closing of the excitation gap within our perturbative expansion anymore.

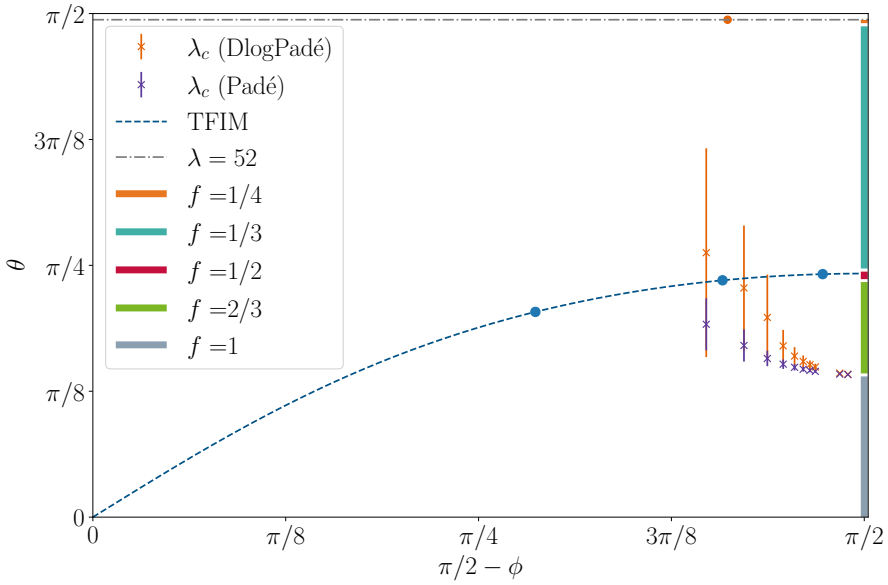

Figure 6.8.: Quantum phase diagram of the FSS model. We parameterize $\theta = \arctan(\lambda)$ and $\phi = \arctan(\Omega/\delta)$. Note that the x-axis is shifted by $\pi/2$. The values λ_c indicate where the one quasi-particle excitation gap in the limit of small θ closes. They are obtained by series expansions around the weak-interaction-strength limit for discrete ϕ, i.e. expanding straight up from the x-axis. Averages from corresponding DlogPadé and Padé extrapolations are shown in orange and purple respectively. The error-bars indicate the standard deviation from averaging over all non-defective extrapolants. For $\phi \gtrsim 0.35$ (20.1°), no critical point can be detected within the perturbative approach. The line in parameter space where the FSS model maps exactly to the TFIM ($\delta/V \approx 2.105$, with interaction truncated after the third-nearest neighbor) is shown as dashed line. The high-field expansions for the TFIM performed in section 5.4 start from the origin, expanding along the dashed line. The three dots along the line mark the characteristic values $0.3, 0.8, 2.8$ for $J/2h$ for phase transitions within the TFIM, respectively, for reference (see main text for details). For $\phi = 0$, the solid lines show the filling fractions of the crystalline ground states calculated in section 6.2. The orange dot on the dot-dashed gray line ($\lambda = 52$) shows where a quantum spin liquid state is found in Ref. [39] (see also section 2.3).

The classical limit $\Omega = 0$ is found for $\pi/2 - \phi = \pi/2$. In this limit, crystalline ground-state structures with filling fraction f depending on δ/V are found, as described in detail in section 6.2. In the phase diagram, we show the extent of the dominant phases as solid lines. Note again that in the determination of these crystalline ground states, we take the full long-range van-der-Waals interaction into account, while the other results emerge from a truncated interaction.

The TFIM is contained in the FSS model for $\delta/V = \bar{\mu}^6/2 \approx 2.105$. The resulting line in parameter space is drawn as a dashed line in Figure 6.8. A detailed discussion of the J_1-J_2-J_3 TFIM was already subject of chapter 5, where we considered arbitrary ratios of the J_i. Further, higher

orders $k_{\max} = 9, 10, 11$ were obtained. For the fixed algebraic decay with $\alpha = 6$ presented in the phase diagram, we found that no phase transition can be detected within the TFIM. Although other J_i ratios are not contained within the phase diagram, it is useful to employ them for speculations about the FSS model.

For the J_1-J_2 TFIM we found a transition from the weak-interaction-strength limit into a quantum ordered phase favored by quantum fluctuations with structure given by the gap momentum $\boldsymbol{k}_{\min} = \pm\left(\frac{2\pi}{3}, -\frac{2\pi}{3}\right)$ (compare subsection 5.1.3 and subsection 5.1.4). This scenario seems to extend to a model where the third-nearest-neighbor interaction J_3 is added, as long as the hierarchy $J_1 > J_2 > J_3$ is conserved. However, we also found that having $J_1 \gg J_{2,3}$ as well as $J_2 \lesssim 2J_3$ is a regime where either the gap closes beyond the range where the extrapolants are converged or does not close at all. Note again that for $\alpha = 6$, $J_2/J_3 \approx 2.37$.
For reference, we show three characteristic values of the perturbation parameter $J/2h$ of the TFIM in the phase diagram in Figure 6.8 as blue dots:

- $J/2h = 0.3$, which is roughly the point of the phase transition in the reduced J_1-J_2 TFIM (with $J_1 = J_2$),
- $J/2h = 0.8$, which is roughly the point up to which a phase transition can be detected in the J_1-J_2-J_3 TFIM with $J_2 \gtrsim J_3$ smaller than but comparable to J_1 in section 5.3, and
- $J/2h = 2.8$, which is roughly the point up to which the extrapolants of the J_1-J_2-J_3 TFIM with the J_i corresponding to $\alpha = 6$ are converged (compare Figure 5.22).

In particular, the last value $J/2h = 2.8$ lies close to the classical limit in the parametrization of the phase diagram, so that we can conclude that the gap does not close and there is no phase transition almost along the entire shown TFIM line. Note that the TFIM line ends in the crystalline phase with filling fraction $f = 1/2$. We recapitulate that for the truncated interaction, the classical ground-state manifold is degenerate (compare section 5.3) and that for $J_1 \gg J_2 > J_3$ a maximally resonating ground state is selected by quantum fluctuations for small $h = \Omega/2$. For the full long-range interaction, we find that the maximally resonating state is the energetically favored classical ground state of the system (compare section 6.2). One might speculate that a transition from the polarized to this quantum ordered phase occurs at some point between $J/2h = 2.8$ and $J/2h \to \infty$, which we however can not capture with the series expansion.

Naturally, the same hierarchy of interaction strengths, $V_1 \gg V_2 > V_3$, occurs in the FSS model. Again, we find that the momentum of the excitation gap is $\boldsymbol{k}_{\min} = \pm\left(\frac{2\pi}{3}, -\frac{2\pi}{3}\right)$, i.e. exactly the gap momentum we find for that interaction strength hierarchy in the TFIM. While this might hint at similarities in dominating mechanisms being realized at different filling fractions, we do not have the means to make any tangible propositions. The low order ($k_{\max} = 6$) of the series expansion of the FSS model limits the range of parameters to be investigated. Further, we were not able to determine the critical exponent for those Ω/δ where a gap closing was found due to the low quality of the obtained DlogPadé extrapolants. Lastly, we can not conclude that the closing of the gap indicates a continuous phase transition and rule out a prior first-order transition. A model for the phase beyond the respective phase transition is still to be developed. Thus, in order to be able to make more rigorous statements about phase transitions within the full FSS model, further analysis is required.

As the last component of the quantum phase diagram, we integrate some results found in the DMRG calculations by Verresen et al. in [39]. A detailed discussion of their findings is provided in section 2.3. They mainly investigate a blockade model, but also expand their calculations to the

actual algebraically decaying interaction. In particular, there they find $\delta/\Omega = 3.5$ for $\lambda \approx 52$, indicated by the gray dot-dashed line and orange dot. Here, it is clear that this parameter regime is beyond reach for our perturbative approach. As discussed in section 2.3, they truncate the interaction after the fourth-nearest neighbor. The interaction strength parameterized by λ is chosen such that the system is described perturbatively by a dimer model with a small admixture of monomers, resulting in a filling fraction $f \lesssim 1/4$. It can be seen from the gray dot-dashed line that we confirm such a filling in the classical limit for $\lambda = 52$. Note, however, that they find that taking further neighbors into account seems to destabilize the spin liquid and the the phase diagram along that line is not yet fully understood, especially considering the algebraically decaying van-der-Waals potential compared to a simple blockade model.

7. Conclusion

In this chapter we first provide a summary of the central results obtained in the scope of this thesis. Afterwards, we give an outlook over remaining open points and possible further research directions.

7.1. Summary

In this thesis we investigated an arrangement of Rydberg atoms on the link-Kagome lattice subject to a laser field. Rydberg atoms are atoms with one valence electron in a highly excited quantum level, giving rise to a long-range van-der-Waals interaction between Rydberg-excited atoms which decays with their distance r as $V(r) = V/r^6$ [1]. We described the system in terms of hardcore bosons using the Fendley-Sengupta-Sachdev (FSS) model [41], which is defined with the Rabi-frequency Ω and detuning δ of the laser, as well as the interaction strength V. We saw that the FSS model contains the transverse-field Ising model (TFIM) for a specific parameter ratio $\delta/V \approx 2.105$. The FSS model on the link-Kagome lattice is of interest as it is predicted to host a $\mathbb{Z}_2$ spin liquid phase for intermediate δ/Ω and strong interactions V [39], which could also be detected in experiments [34]. In this thesis we focused on the parameter regime of weak interaction strengths.
The limit of weak interaction strengths in the FSS model and the TFIM was approached using the well established method of perturbative continuous unitary transformations, with which the Hamiltonian is transformed into a block diagonal, quasi-particle conserving form. Physical quantities in this effective model, in particular the one quasi-particle excitation gap, were calculated in the thermodynamic limit on finite linked clusters. We chose to treat the long-range interaction with a truncation after the third-nearest-neighbor coupling. We further analyzed the ground-state configurations in the limit of strong interactions in the TFIM.

The construction of a quantum phase diagram was approached by first investigating the TFIM. We extended the discussion from the algebraically decaying interaction strength, $V(r) = V/r^6$, to arbitrary interactions $J_{1,2,3}$, with specific attention to the boundary cases of the J_1-J_2 and the J_1-J_3 TFIM. For both of these models, we found a macroscopically degenerate ground state for $h = 0$.
For small magnetic fields in the J_1-J_2 model, we found that a clock-ordered state emerges in an order-by-disorder scenario triggered by quantum fluctuations which couple $h = 0$ ground states via resonances occurring in sixth order perturbation theory. In the high-field limit, a series expansion of the gap with $\boldsymbol{k}_{\min} = \pm\left(\frac{2\pi}{3}, -\frac{2\pi}{3}\right)$ in order $k_{\max} = 11$ indicated a continuous phase transition from the polarized phase into this clock-ordered phase for $J_1 = J_2$. In analogy to the TFIM on the triangular lattice [72], we argued that this transition lies in the 3d XY universality class. We were able to extend this argumentation to arbitrary J_1, J_2 by considering respective series expansions of the gap in order $k_{\max} = 10$.
In the J_1-J_3 model, we found that in the low-field limit, a ground state with $\boldsymbol{k}_{\min} = (0, 0)$ is favored by diagonal energy corrections in fourth order. Series expansion around the high-field limit in order $k_{\max} = 11$ for $J_1 = J_3$ indicated a continuous phase transition which we argued

lies in the 3d Ising criticality class between polarized and quantum ordered phase. Again, this argumentation was extended to arbitrary J_1, J_3, where we performed series expansion in order $k_{\max} = 10$.
We then expanded these conjectures to the J_1-J_2-J_3 TFIM. Here, we found indications for analogous scenarios with a 3d XY transition for $J_1 > J_2 > J_3$ and a 3d Ising transition for $J_1 > J_3 > J_2$. For $J_1 > J_2 = J_3$, we found no indications for a continuous phase transition. Further, we found that the lowest energy band becomes dispersive only in perturbation order 7, a point which was not investigated further within the scope of this thesis.
Turning to the J_1-J_2-J_3 TFIM with algebraic decay, we found no indications for a phase transition within our perturbative series expansion. We explained this with the strongly dominating interaction $J_1 \gg J_{2,3}$, resulting in the model being approximated by disconnected, purely local triangles not allowing for a phase transition.

We further investigated the classical limit, $\Omega = 0$, of the FSS model with full long-range van-der-Waals interaction, following the approach developed in Ref. [46]. In this approach, it is exploited that the energy of periodic ordering patterns can be evaluated taking the full long-range interaction into account using resummed couplings. The ground state is determined by a search of the energetically lowest configuration on a set of all unit cells up to a certain extent, which is generated systematically, employing a global minimization scheme. We constructed a phase diagram of the ground state in δ/V, in which we found configurations with filling fractions $f \in [0, 1]$.
In particular, we found that the state with the maximal number of resonating plaquettes providing the leading contribution to the J_1-J_2 TFIM clock order is also the ground state in the classical limit of the TFIM with $f = 1/2$ selected by the full long-range interaction. Further, for a filling fraction of $f = 1/4$, we found a different configuration than the one found in Ref. [39] in a blockade-model approximation of the FSS model in the limit of small $\Omega > 0$. They discuss a valence bond solid (VBS) state with resonating plaquettes, which they take as a starting point for the discussion of the emergence of a spin liquid phase. We quantified the stability of the long-range ground state we found against quantum fluctuations, which we conjectured lead to a level crossing with the VBS state.

For the V_1-V_2-V_3 FSS model, series expansions in the weak-interaction-strength limit up to order $k_{\max} = 6$ indicated a closing of the gap at $\boldsymbol{k}_{\min} = \pm\left(\frac{2\pi}{3}, -\frac{2\pi}{3}\right)$ for $\Omega/\delta \in (0, 1/3)$. Assuming no first-order phase transition occurs prior to the gap closing, we summarized the values of the gap closing as an estimate for the breakdown of the polarizes phase for small V in a quantum phase diagram. The TFIM with algebraic decay is contained in this quantum phase diagram on a parameter line, along which we know no phase transition occurs within a certain range. Considering for example the same found gap momentum as in the $J_1 \gg J_2 > J_3$ TFIM, we speculated about the realizations of similar mechanisms, but could not draw conclusions without further analysis.

7.2. Outlook

We note that several points remain open questions within this thesis. While a general understanding in the J_1-J_2-J_3 TFIM could be obtained, a few details remain to be investigated. In the low-field limit of the J_1-J_2 we only analyzed off-diagonal corrections arising due to the transverse magnetic field. While we assume those to be dominating for larger fields, also diagonal corrections have to be considered in order to obtain a full picture for all $h > 0$. In the high-field

limit of this model, we found a critical exponent $\nu = 0.806 \pm 0.056$ which lies above the literature value $\nu_{\text{3d Ising}} = 0.679(7)$ [75] of the argued 3d XY criticality class of the found quantum phase transition. We attribute this discrepancy to the obtained perturbation $k_{\max} = 11$ being low considering the extent of the relevant fluctuations. As the DlogPadé extrapolation tends to overestimate the critical point, leading to an overestimation of the critical exponent, we assume our conjecture could be supported by a quantum Monte Carlo estimate for the critical point with which the extrapolations could be biased.
Regarding the full J_1-J_2-J_3 TFIM, the distinct point $J_1 > J_2 = J_3$ remains open for analysis. Here we found no indication of a quantum phase transition within the perturbative series expansion. Further, we found that the lowest energy band becomes dispersive in perturbation order $k = 7$. This finding was not investigated further in the scope of this thesis and remains as question for the future.

A particularly interesting direction for further studies is the investigation of the role of long-range interactions in the FSS model. In this thesis, we mainly took into account interactions between the three nearest neighbors. The treatment of the full long-range interaction in the classical limit already offered insights into subtleties neglected by this approximation. Regarding the prediction of quantum spin liquid states in the investigated system, it has already been found that long-range interactions seem to destabilize those states [34, 39]. The specific mechanism for this however is not yet understood and the behavior of the system away from the limit of dimer coverings for $\Omega > 0$ remains unclear.
The role of long-range interactions is also an interesting point regarding its interplay with geometric frustration. It is already known from the triangular lattice that this requires a careful analysis, see e.g. [44–48]. Coming from the classical limit $h = 0$ in the nearest-neighbor antiferromagnetic TFIM on the triangular lattice, different states are selected by the long-range interaction and a small transverse magnetic field. In contrast, we found that for the J_1-J_2 TFIM the same configuration is selected upon including the full long-range interaction and adding a small transverse magnetic field.
Lastly, it would be interesting to investigate the effect of continuously varying the decay exponent from $\alpha = 6$, like it can be realized in trapped-ion systems [85–87].

A. One quasi-particle gap of the Fendley-Sengupta-Sachdev model

In the following we show results obtained for the one quasi-particle excitation gap Δ in the FSS model for the parameter sets (δ, Ω) used for the construction of the quantum phase diagram in section 6.3. As described in section 6.1, Δ is calculated as a series in $\lambda = V/\sqrt{\delta^2 + \Omega^2}$ up to order $k_{\max} = 6$ depending on the parameter $\phi = \arctan(\Omega/\delta)$. The results are shown in analogous fashion to the ones in main thesis.

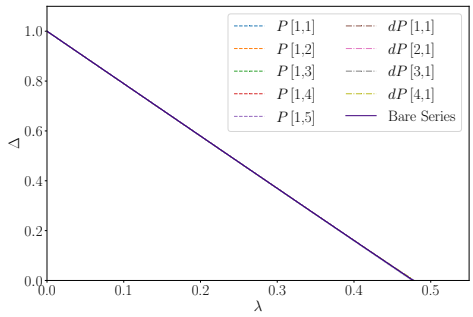

(a) Δ for $(\delta = 30, \Omega = 1)$, resulting in $\phi \approx 1.91°$.

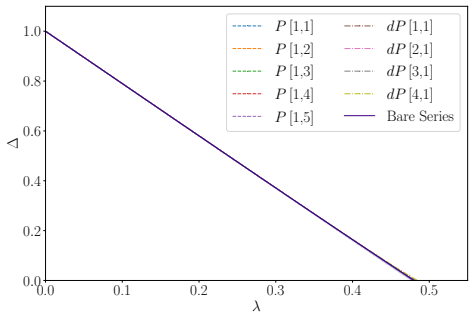

(b) Δ for $(\delta = 20, \Omega = 1)$, resulting in $\phi \approx 2.86°$.

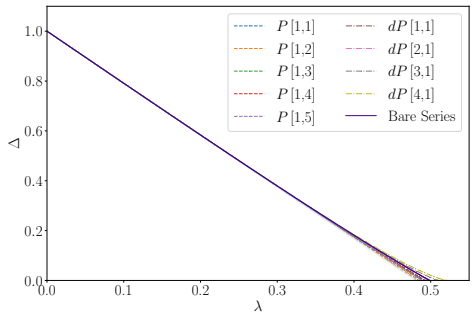

(c) Δ for $(\delta = 10, \Omega = 1)$, resulting in $\phi \approx 5.71°$.

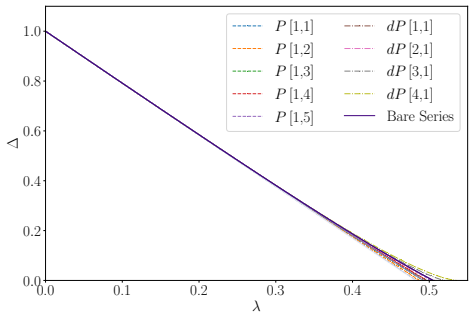

(d) Δ for $(\delta = 9, \Omega = 1)$, resulting in $\phi \approx 6.34°$.

Figure A.1.: One quasi-particle excitation gap Δ in the FSS model for various parameter sets (δ, Ω). The bare series in the maximal order $k_{\max} = 6$ is shown along lower orders in lower opacities and the obtained Padé and DlogPadé extrapolants $(d)P[L, M]$ as a function of $\lambda = V/2\tilde{\Delta}$. Defective extrapolants are sorted out. Note that H^{FSS} is defined such that Δ is calculated in units of $2\tilde{\Delta}$.

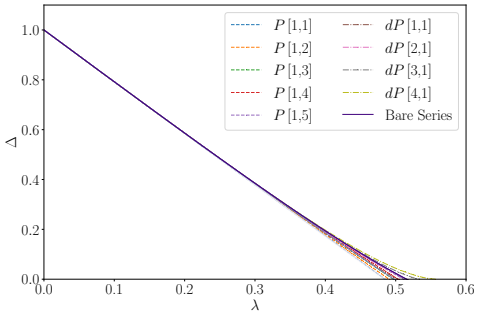

(e) Δ for $(\delta = 8, \Omega = 1)$, resulting in $\phi \approx 7.12°$.

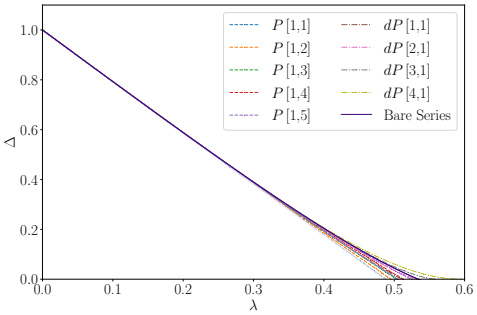

(f) Δ for $(\delta = 7, \Omega = 1)$, resulting in $\phi \approx 8.13°$.

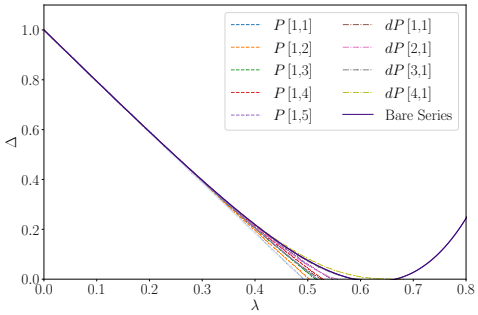

(g) Δ for $(\delta = 6, \Omega = 1)$, resulting in $\phi \approx 9.46°$.

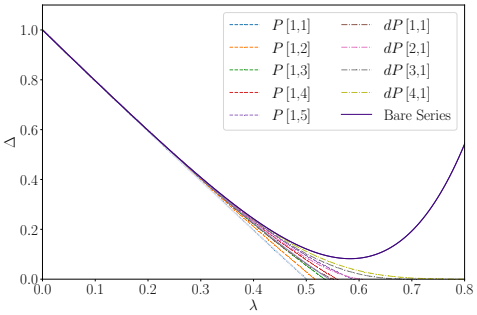

(h) Δ for $(\delta = 5, \Omega = 1)$, resulting in $\phi \approx 11.31°$.

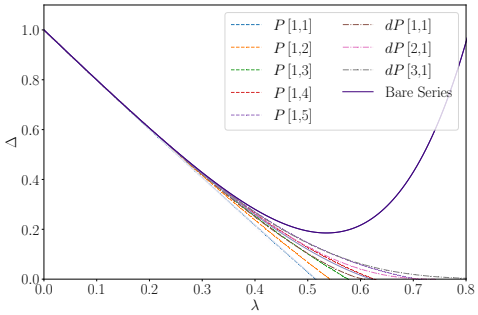

(i) Δ for $(\delta = 4, \Omega = 1)$, resulting in $\phi \approx 14.04°$.

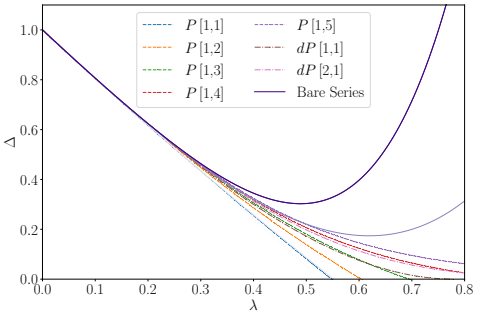

(j) Δ for $(\delta = 3, \Omega = 1)$, resulting in $\phi \approx 18.43°$.

Figure A.1.: One quasi-particle excitation gap Δ in the FSS model for various parameter sets (δ, Ω) (continued). The bare series in the maximal order $k_{\max} = 6$ is shown along lower orders in lower opacities and the obtained Padé and DlogPadé extrapolants $(d)P[L, M]$ as a function of $\lambda = V/2\tilde{\Delta}$. Defective extrapolants are sorted out. Note that H^{FSS} is defined such that Δ is calculated in units of $2\tilde{\Delta}$.

Bibliography

[1] A. Browaeys, D. Barredo, and T. Lahaye, "Experimental investigations of dipole-dipole interactions between a few rydberg atoms", *Journal of Physics B: Atomic, Molecular and Optical Physics*, vol. 49, no. 15, 2016. DOI: 10.1088/0953-4075/49/15/152001.

[2] T. F. Gallagher, "Rydberg atoms", *Reports on Progress in Physics*, vol. 51, no. 2, 1988. DOI: 10.1088/0034-4885/51/2/001.

[3] X. Wu *et al.*, "A concise review of rydberg atom based quantum computation and quantum simulation*", *Chinese Physics B*, vol. 30, no. 2, 2021. DOI: 10.1088/1674-1056/abd76f.

[4] E. Urban *et al.*, "Observation of rydberg blockade between two atoms", *Nature Physics*, vol. 5, no. 2, 2009. DOI: https://doi.org/10.1038/nphys1178.

[5] A. Gaëtan *et al.*, "Observation of collective excitation of two individual atoms in the rydberg blockade regime", *Nature Physics*, vol. 5, no. 2, 2009. DOI: https://doi.org/10.1038/nphys1183.

[6] Y. Gnedin *et al.*, "Rydberg atoms in astrophysics", *New Astronomy Reviews*, vol. 53, no. 7-10, 2009. DOI: https://doi.org/10.1016/j.newar.2009.07.003.

[7] O. Firstenberg, C. S. Adams, and S. Hofferberth, "Nonlinear quantum optics mediated by rydberg interactions", *Journal of Physics B: Atomic, Molecular and Optical Physics*, vol. 49, no. 15, 2016. DOI: 10.1088/0953-4075/49/15/152003.

[8] C. S. Adams, J. D. Pritchard, and J. P. Shaffer, "Rydberg atom quantum technologies", *Journal of Physics B: Atomic, Molecular and Optical Physics*, vol. 53, no. 1, 2019. DOI: 10.1088/1361-6455/ab52ef.

[9] D. Jaksch, J. I. Cirac, P. Zoller, S. L. Rolston, R. Côté, and M. D. Lukin, "Fast quantum gates for neutral atoms", *Physical Review Letters*, vol. 85, no. 10, 2000. DOI: 10.1103/PhysRevLett.85.2208.

[10] M. A. Nielsen and I. L. Chuang, *Quantum Computation and Quantum Information*, 10th ed. Cambridge University Press, 2000. DOI: 10.1017/CBO9780511976667.

[11] M. Saffman, T. G. Walker, and K. Mølmer, "Quantum information with rydberg atoms", *Reviews of Modern Physics*, vol. 82, no. 3, 2010. DOI: 10.1103/RevModPhys.82.2313.

[12] L. Isenhower *et al.*, "Demonstration of a neutral atom controlled-NOT quantum gate", *Physical Review Letters*, vol. 104, no. 1, 2010. DOI: 10.1103/physrevlett.104.010503.

[13] K. M. Maller *et al.*, "Rydberg-blockade controlled-not gate and entanglement in a two-dimensional array of neutral-atom qubits", *Physical Review A*, vol. 92, no. 2, 2015. DOI: https://doi.org/10.1103/PhysRevA.92.022336.

[14] T. Graham *et al.*, "Rydberg-mediated entanglement in a two-dimensional neutral atom qubit array", *Physical Review Letters*, vol. 123, no. 23, 2019. DOI: https://doi.org/10.1103/PhysRevLett.123.230501.

[15] T. H. Johnson, S. R. Clark, and D. Jaksch, "What is a quantum simulator?", *EPJ Quantum Technology*, vol. 1, no. 1, 2014. DOI: https://doi.org/10.1140/epjqt10.

[16] A. Browaeys and T. Lahaye, "Many-body physics with individually controlled rydberg atoms", *Nature Physics*, vol. 16, no. 2, 2020. DOI: https://doi.org/10.1038/s41567-019-0733-z.

[17] D. Jaksch and P. Zoller, "The cold atom hubbard toolbox", *Annals of Physics*, vol. 315, no. 1, 2005. DOI: https://doi.org/10.1016/j.aop.2004.09.010.

[18] I. Bloch, J. Dalibard, and S. Nascimbène, "Quantum simulations with ultracold quantum gases", *Nature Physics*, vol. 8, no. 4, 2012. DOI: https://doi.org/10.1038/nphys2259.

[19] K. Kim *et al.*, "Quantum simulation of frustrated ising spins with trapped ions", *Nature*, vol. 465, no. 7298, 2010. DOI: https://doi.org/10.1038/nature09071.

[20] D. Porras and J. I. Cirac, "Effective quantum spin systems with trapped ions", *Physical Review Letters*, vol. 92, no. 20, 2004. DOI: https://doi.org/10.1103/PhysRevLett.92.207901.

[21] J. Clarke and F. K. Wilhelm, "Superconducting quantum bits", *Nature*, vol. 453, no. 7198, 2008. DOI: https://doi.org/10.1038/nature07128.

[22] A. A. Houck, H. E. Türeci, and J. Koch, "On-chip quantum simulation with superconducting circuits", *Nature Physics*, vol. 8, no. 4, 2012. DOI: https://doi.org/10.1038/nphys2251.

[23] H. Bernien *et al.*, "Probing many-body dynamics on a 51-atom quantum simulator", *Nature*, vol. 551, no. 7682, 2017. DOI: https://doi.org/10.1038/nature24622.

[24] S. de Léséleuc *et al.*, "Observation of a symmetry-protected topological phase of interacting bosons with rydberg atoms", *Science*, vol. 365, no. 6455, 2019. DOI: 10.1126/science.aav9105.

[25] W. S. Bakr *et al.*, "Probing the superfluid–to–mott insulator transition at the single-atom level", *Science*, vol. 329, no. 5991, 2010. DOI: 10.1126/science.1192368.

[26] J. F. Sherson, C. Weitenberg, M. Endres, M. Cheneau, I. Bloch, and S. Kuhr, "Single-atom-resolved fluorescence imaging of an atomic mott insulator", *Nature*, vol. 467, no. 7311, 2010. DOI: https://doi.org/10.1038/nature09378.

[27] A. Keesling *et al.*, "Quantum kibble–zurek mechanism and critical dynamics on a programmable rydberg simulator", *Nature*, vol. 568, no. 7751, 2019. DOI: https://doi.org/10.1038/s41586-019-1070-1.

[28] P. Schauß *et al.*, "Crystallization in ising quantum magnets", *Science*, vol. 347, no. 6229, 2015. DOI: https://doi.org/10.1126/science.1258351.

[29] V. Lienhard *et al.*, "Observing the space- and time-dependent growth of correlations in dynamically tuned synthetic ising models with antiferromagnetic interactions", *Physical Review X*, vol. 8, no. 2, 2018. DOI: https://doi.org/10.1103/PhysRevX.8.021070.

[30] E. Guardado-Sanchez *et al.*, "Probing the quench dynamics of antiferromagnetic correlations in a 2d quantum ising spin system", *Physical Review X*, vol. 8, no. 2, 2018. DOI: https://doi.org/10.1103/PhysRevX.8.021069.

[31] H. Labuhn *et al.*, "Tunable two-dimensional arrays of single rydberg atoms for realizing quantum ising models", *Nature*, vol. 534, no. 7609, 2016. DOI: https://doi.org/10.1038/nature18274.

[32] P. Scholl *et al.*, "Quantum simulation of 2d antiferromagnets with hundreds of rydberg atoms", *Nature*, vol. 595, no. 7866, 2021. DOI: https://doi.org/10.1038/s41586-021-03585-1.

[33] S. Ebadi *et al.*, "Quantum phases of matter on a 256-atom programmable quantum simulator", *Nature*, vol. 595, no. 7866, 2021. DOI: https://doi.org/10.1038/s41586-021-03582-4.

[34] G. Semeghini *et al.*, "Probing topological spin liquids on a programmable quantum simulator", *Science*, vol. 374, no. 6572, 2021. DOI: 10.1126/science.abi8794.

[35] D. Barredo, H. Labuhn, S. Ravets, T. Lahaye, A. Browaeys, and C. S. Adams, "Coherent excitation transfer in a spin chain of three rydberg atoms", *Physical Review Letters*, vol. 114, no. 11, 2015. DOI: https://doi.org/10.1103/PhysRevLett.114.113002.

[36] J. Zeiher *et al.*, "Many-body interferometry of a rydberg-dressed spin lattice", *Nature Physics*, vol. 12, no. 12, 2016. DOI: https://doi.org/10.1038/nphys3835.

[37] J. Zeiher *et al.*, "Coherent many-body spin dynamics in a long-range interacting ising chain", *Physical Review X*, vol. 7, no. 4, 2017. DOI: 10.1103/PhysRevX.7.041063.

[38] L. Savary and L. Balents, "Quantum spin liquids: A review", *Reports on Progress in Physics*, vol. 80, no. 1, 2016. DOI: 10.1088/0034-4885/80/1/016502.

[39] R. Verresen, M. D. Lukin, and A. Vishwanath, "Prediction of toric code topological order from rydberg blockade", *Physical Review X*, vol. 11, no. 3, 2021. DOI: 10.1103/PhysRevX.11.031005.

[40] G. Giudici, M. D. Lukin, and H. Pichler, "Dynamical preparation of quantum spin liquids in rydberg atom arrays", *Physical Review Letters*, vol. 129, no. 9, 2022. DOI: 10.1103/PhysRevLett.129.090401.

[41] P. Fendley, K. Sengupta, and S. Sachdev, "Competing density-wave orders in a one-dimensional hard-boson model", vol. 69, no. 7, 2004. DOI: 10.1103/PhysRevB.69.075106.

[42] T. Matsubara and H. Matsuda, "A lattice model of liquid helium", *Progress of Theoretical Physics*, vol. 16, no. 6, 1956. DOI: 10.1143/PTP.16.569.

[43] E. Ising, "Beitrag zur theorie des ferromagnetismus", *Zeitschrift für Physik*, vol. 31, no. 1, 1925. DOI: https://doi.org/10.1007/BF02980577.

[44] S. N. Saadatmand, S. D. Bartlett, and I. P. McCulloch, "Phase diagram of the quantum ising model with long-range interactions on an infinite-cylinder triangular lattice", *Physical Review B*, vol. 97, no. 15, 2018. DOI: https://doi.org/10.1103/PhysRevB.97.155116.

[45] J. Koziol, S. Fey, S. C. Kapfer, and K. P. Schmidt, "Quantum criticality of the transverse-field ising model with long-range interactions on triangular-lattice cylinders", *Physical Review B*, vol. 100, no. 14, 2019. DOI: 10.1103/PhysRevB.100.144411.

[46] J. A. Koziol, A. Duft, G. Morigi, and K. P. Schmidt, "Systematic analysis of crystalline phases in bosonic lattice models with algebraically decaying density-density interactions", 2022. DOI: https://doi.org/10.48550/arXiv.2212.02091.

[47] S. Fey, S. C. Kapfer, and K. P. Schmidt, "Quantum criticality of two-dimensional quantum magnets with long-range interactions", *Physical Review Letters*, vol. 122, no. 1, 2019. DOI: https://doi.org/10.1103/PhysRevLett.122.017203.

[48] A. Smerald, S. Korshunov, and F. Mila, "Topological aspects of symmetry breaking in triangular-lattice ising antiferromagnets", *Physical Review Letters*, vol. 116, no. 19, 2016. DOI: https://doi.org/10.1103/PhysRevLett.116.197201.

[49] A. Kitaev, "Fault-tolerant quantum computation by anyons", *Annals of Physics*, vol. 303, no. 1, 2003. DOI: https://doi.org/10.1016/S0003-4916(02)00018-0.

[50] S. Sachdev, "Kagomé and triangular-lattice heisenberg antiferromagnets: Ordering from quantum fluctuations and quantum-disordered ground states with unconfined bosonic spinons", *Physical Review B*, vol. 45, no. 21, 1992. DOI: 10.1103/PhysRevB.45.12377.

[51] R. Moessner and S. L. Sondhi, "Resonating valence bond phase in the triangular lattice quantum dimer model", *Physical Review Letters*, vol. 86, no. 9, 2001. DOI: 10.1103/PhysRevLett.86.1881.

[52] R. Samajdar, D. G. Joshi, Y. Teng, and S. Sachdev, "Emergent $\mathbb{Z}_2$ gauge theories and topological excitations in rydberg atom arrays", *Physical Review Letters*, vol. 130, no. 4, 2023. DOI: 10.1103/PhysRevLett.130.043601.

[53] S. R. White, "Density matrix formulation for quantum renormalization groups", *Physical Review Letters*, vol. 69, no. 19, 1992. DOI: https://doi.org/10.1103/PhysRevLett.69.2863.

[54] S. R. White, "Density-matrix algorithms for quantum renormalization groups", *Physical Review B*, vol. 48, no. 14, 1993. DOI: https://doi.org/10.1103/PhysRevB.48.10345.

[55] R. Verresen and A. Vishwanath, "Unifying kitaev magnets, kagomé dimer models, and ruby rydberg spin liquids", *Physical Review X*, vol. 12, no. 4, 2022. DOI: 10.1103/PhysRevX.12.041029.

[56] P. S. Tarabunga, F. M. Surace, R. Andreoni, A. Angelone, and M. Dalmonte, "Gauge-theoretic origin of rydberg quantum spin liquids", *Physical Review Letters*, vol. 129, no. 19, 2022. DOI: 10.1103/PhysRevLett.129.195301.

[57] F. Wegner, "Flow-equations for hamiltonians", *Annalen der Physik*, vol. 506, no. 2, 1994. DOI: https://doi.org/10.1002/andp.19945060203.

[58] S. D. Głazek and K. G. Wilson, "Renormalization of hamiltonians", *Physical Review D*, vol. 48, no. 12, 1993. DOI: https://doi.org/10.1103/PhysRevD.48.5863.

[59] C. Knetter and G. Uhrig, "Perturbation theory by flow equations: Dimerized and frustrated s = 1/2 chain", *The European Physical Journal B*, vol. 13, no. 2, 2000. DOI: 10.1007/s100510050026.

[60] K. Cöster and K. P. Schmidt, "Optimizing linked-cluster expansions by white graphs", *Physical Review E*, vol. 92, no. 2, 2015. DOI: https://doi.org/10.1103/PhysRevE.92.022118.

[61] C. Knetter, K. P. Schmidt, and G. S. Uhrig, "The structure of operators in effective particle-conserving models", *Journal of Physics A: Mathematical and General*, vol. 36, no. 29, 2003. DOI: 10.1088/0305-4470/36/29/302.

[62] K. Cöster, "Quasiparticle pictures and graphs - from perturbative to non-perturbative linked-cluster expansions", Ph.D. dissertation, Technische Universität Dortmund, 2015. DOI: http://dx.doi.org/10.17877/DE290R-16955.

[63] M. P. Gelfand and R. R. P. Singh, "High-order convergent expansions for quantum many particle systems", *Advances in Physics*, vol. 49, no. 1, 2000. DOI: https://doi.org/10.1080/000187300243390.

[64] M. Mühlhauser and K. P. Schmidt, "Linked cluster expansions via hypergraph decompositions", *Physical Review E*, vol. 105, no. 6, 2022. DOI: 10.1103/PhysRevE.105.064110.

[65] J. Oitmaa, C. Hamer, and W. Zheng, *Series Expansion Methods for Strongly Interacting Lattice Models*. Cambridge University Press, 2006. DOI: https://doi.org/10.1017/CBO9780511584398.

[66] M. P. Gelfand, "Series expansions for excited states of quantum lattice models", *Solid State Communications*, vol. 98, no. 1, 1996. DOI: https://doi.org/10.1016/0038-1098(96)00051-8.

[67] S. Sachdev, *Quantum Phase Transitions*, 2nd ed. Cambridge University Press, 2011. DOI: https://doi.org/10.1017/CBO9780511973765.

[68] G. A. Baker and P. Graves-Morris, *Padé Approximants* (Encyclopedia of Mathematics and its Applications), 2nd ed. Cambridge University Press, 1996. DOI: https://doi.org/10.1017/CBO9780511530074.

[69] C. Domb, *Phase transitions and critical phenomena*. Elsevier, 2000.

[70] R. Moessner and S. L. Sondhi, "Ising models of quantum frustration", *Physical Review B*, vol. 63, no. 22, 2001. DOI: 10.1103/PhysRevB.63.224401.

[71] J. Villain, R. Bidaux, J.-P. Carton, and R. Conte, "Order as an effect of disorder", *Journal de Physique*, vol. 41, no. 11, 1980. DOI: https://doi.org/10.1051/jphys:0198000410110126300.

[72] M. Powalski, K. Coester, R. Moessner, and K. P. Schmidt, "Disorder by disorder and flat bands in the kagome transverse field ising model", *Physical Review B*, vol. 87, no. 5, 2013. DOI: 10.1103/PhysRevB.87.054404.

[73] S. V. Isakov and R. Moessner, "Interplay of quantum and thermal fluctuations in a frustrated magnet", *Physical Review B*, vol. 68, no. 10, 2003. DOI: 10.1103/PhysRevB.68.104409.

[74] D. Blankschtein, M. Ma, A. N. Berker, G. S. Grest, and C. M. Soukoulis, "Orderings of a stacked frustrated triangular system in three dimensions", *Physical Review B*, vol. 29, 9 1984. DOI: 10.1103/PhysRevB.29.5250.

[75] A. P. Gottlob and M. Hasenbusch, "The xy model and the three-state antiferromagnetic potts model in three dimensions: Critical properties from fluctuating boundary conditions", *Journal of Statistical Physics*, vol. 77, no. 3-4, 1994. DOI: https://doi.org/10.1007/BF02179470.

[76] F. Kos, D. Poland, D. Simmons-Duffin, and A. Vichi, "Precision islands in the ising and o(n) models", *Journal of High Energy Physics*, vol. 2016, no. 8, 2016. DOI: https://doi.org/10.1007/JHEP08(2016)036.

[77] M. Takahashi, "Half-filled hubbard model at low temperature", *Journal of Physics C: Solid State Physics*, vol. 10, no. 8, 1977. DOI: 10.1088/0022-3719/10/8/031.

[78] S. Suzuki, J. Inoue, and B. K. Chakrabarti, *Quantum Ising Phases and Transitions in Transverse Ising Models*. Springer Berlin Heidelberg, 2013. DOI: 10.1007/978-3-642-33039-1.

[79] G. Murthy, D. Arovas, and A. Auerbach, "Superfluids and supersolids on frustrated two-dimensional lattices", *Physical Review B*, vol. 55, no. 5, 1997. DOI: 10.1103/PhysRevB.55.3104.

[80] S. Wessel and M. Troyer, "Supersolid hard-core bosons on the triangular lattice", *Physical Review Letters*, vol. 95, no. 12, 2005. DOI: 10.1103/PhysRevLett.95.127205.

[81] P. Nikolic and T. Senthil, "Physics of low-energy singlet states of the kagome lattice quantum heisenberg antiferromagnet", *Physical Review B*, vol. 68, no. 21, 2003. DOI: https://doi.org/10.1103/PhysRevB.68.214415.

[82] R. R. P. Singh and D. A. Huse, "Ground state of the spin-1/2 kagome-lattice heisenberg antiferromagnet", *Physical Review B*, vol. 76, no. 18, 2007. DOI: 10.1103/PhysRevB.76.180407.

[83] D. Poilblanc and G. Misguich, "Competing valence bond crystals in the kagome quantum dimer model", *Physical Review B*, vol. 84, no. 21, 2011. DOI: http://dx.doi.org/10.1103/PhysRevB.84.214401.

[84] J. K. Freericks and H. Monien, "Strong-coupling expansions for the pure and disordered bose-hubbard model", *Physical Review B*, vol. 53, no. 5, 1996. DOI: https://doi.org/10.1103/PhysRevB.53.2691.

[85] R. Islam *et al.*, "Emergence and frustration of magnetism with variable-range interactions in a quantum simulator", *Science*, vol. 340, no. 6132, 2013. DOI: https://doi.org/10.1126/science.1232296.

[86] J. G. Bohnet *et al.*, "Quantum spin dynamics and entanglement generation with hundreds of trapped ions", *Science*, vol. 352, no. 6291, 2016. DOI: DOI:10.1126/science.aad9958.

[87] J. W. Britton *et al.*, "Engineered two-dimensional ising interactions in a trapped-ion quantum simulator with hundreds of spins", *Nature*, vol. 484, no. 7395, 2012. DOI: https://doi.org/10.1038/nature10981.

Acknowledgments

Zum Abschluss möchte ich mich noch bei einigen Menschen bedanken, die zur Entstehung dieser Arbeit beigetragen haben.
Zuallererst ein großes Danke an Kai für die Möglichkeit diese Arbeit in deiner Arbeitsgruppe zu schreiben, für die vielen Diskussionen, dein Engagement und die angenehme Arbeitsatmosphäre, die du geschaffen hast. Insbesondere deine enge Betreuung war bemerkenswert und von deiner Begeisterung und Expertise konnte ich immer wieder Neues lernen.
Großer Dank gilt auch meinen Betreuern Jan, Patrick und Matthias 1. Danke für eure Unterstützung und Erklärungen, für euer Interesse an ausgedehnten Diskussionen und stets neuen Ideen, sowie für das Korrekturlesen dieser Arbeit.
Danke an meine Büronachbarn Robert, Sumeet und Max sowie an den gesamten Lehrstuhl, der mich offen aufgenommen hat und das letzte Jahr unter anderem durch ausgedehnte Kaffeepausen und ein freundschaftliches Klima sehr angenehm gestaltet hat.
Zuletzt möchte ich mich bei meiner Familie, meinen Freunden und insbesondere Matthias bedanken. Ihr habt mich über mein gesamtes Studium hinweg stets in stressigen Phasen unterstützt sowie für einen Ausgleich gesorgt. Danke!

Eidesstattliche Versicherung

Hiermit versichere ich, dass ich die vorliegende Arbeit selbstständig verfasst und keine anderen als die angegebenen Quellen und Hilfsmittel benutzt habe, dass alle Stellen der Arbeit, die wörtlich oder sinngemäß aus anderen Quellen übernommen wurden, als solche kenntlich gemacht sind und dass die Arbeit in gleicher oder ähnlicher Form noch keiner Prüfungsbehörde vorgelegt wurde.

Erlangen, den 17.05.2023 Antonia Duft